Multi-material deployable radiative coolers for thermophotovoltaic systems operating in space

Keshav Ramparsad

A THESIS SUBMITTED TO THE FACULTY OF GRADUATE STUDIES IN PARTIAL FULFILLMENT OF THE REQUIREMENTS FOR THE DEGREE OF MASTER OF APPLIED SCIENCES

GRADUATE PROGRAM IN MECHANICAL ENGINEERING

YORK UNIVERSITY

TORONTO, ONTARIO

JULY 2025

© Keshav Ramparsad, 2025

Abstract

Thermophotovoltaic (TPV) systems have seen increasing research interest in recent years due to their distinct capabilities which enable lightweight, continuous heat-to-power conversion at high efficiencies without moving parts. This research investigates the thermal aspects of TPV systems for application in small satellites which demand passive radiative cooling methods across a limited external surface area. A deployable multi-material radiative cooler was designed and tested to provide high cooling capabilities while being lightweight. Initial analysis was conducted using COMSOL Multiphysics software to model different radiative cooler sizes and materials. An experimental setup was designed and built to test the best performing radiative cooler and validate the COMSOL model. The results showed that a 24 cm by 24 cm cooler, featuring a 14 cm by 18 cm copper core surrounded by aluminum, provided a cooling power of 20 W with a mass of 313 g and maintained an operating temperature of 300 K.

Acknowledgements

I would like to express my sincere gratitude to all those who supported me in completing this thesis.

Firstly, my heartfelt thanks to my supervisor, **Dr. Paul O'Brien**, for his invaluable guidance, mentorship, and constructive feedback. This thesis would not have been possible without his dedication.

I am also deeply thankful to my lab members, **Dr. Nima Talebzadeh**, **Shahriar Homaei**, and all others in the lab. Your collaboration, discussions, and feedback were a constant source of motivation and greatly enriched my research.

Furthermore, this project would not have been possible without the generous support of **Columbiad Launch Services**. I am grateful for their commitment to supporting the research conducted by our lab and for providing valuable feedback on our work.

Finally, and most importantly, I wish to express my appreciation to **my family**. Your unwavering support, and encouragement throughout this journey provided the strength needed to achieve this goal.

Thank you all.

Table of contents

Abstract ii
Acknowledgements iii
Table of contents iv
List of figures vii
List of tables xi
List of symbols xii
List of abbreviations xiii
1 Introduction 1
1.1 Problem introduction 1
1.2 Research gap 5
1.3 Objective Statement 6
1.4 Thesis outline 7
2 Relevant theory 8
2.1 Conduction 8
2.2 Convection 12
2.3 Radiation 12
2.4 Thermal circuit 14
2.5 Space environment 14
3 State of the art and literature review 18
3.1 Existing cooling systems in space 18
3.2 Suitable materials 27
3.3 Thermal interfaces 31
3.4 Thermal control coatings 33
3.5 Thermal vacuum chambers 36
4 Method 38
4.1 Preliminary modeling 38
4.1.1 Feasibility analysis 38
4.1.2 Model verification 40
4.1.3 Impact of size changes 41
4.1.4 Impact of materials 42
4.1.5 Panel configurations 42
4.2 Experimental setup 47

4.2.1 Assembled experimental setup 48
4.2.2 Vacuum chamber 48
4.2.3 Vacuum chamber wall temperature 49
4.2.4 Absorbing tape 51
4.2.5 Support for the radiative cooler 52
4.2.6 Heating element 53
4.2.7 Radiative cooler 54
4.2.8 Power supply and temperature measurement 56
4.2.9 TPV system integrated testing setup 56
4.2.10 Measurements 59
4.3 COMSOL modeling 60
4.3.1 Mesh independency study 61
4.3.2 Model parameters 61
4.3.3 Model validation experiment 64
4.3.4 Parametric study 67
4.3.5 Space condition analysis 69
4.4 TPV experiment 70
5 Results & discussion 72
5.1 Preliminary modeling 72
5.1.1 Feasibility analysis 73
5.1.2 Impact of size changes 74
5.1.3 Impact of materials 77
5.1.4 Panel configurations 78
5.2 Model validation 85
5.2.1 Vacuum chamber experiment 85
5.2.2 Error analysis 87
5.2.3 Simulation parameters 90
5.2.4 Result comparison 92
5.3 Parametric study 94
5.3.1 Constrained case 94
5.3.2 Unconstrained cases 95
5.4 Performance in space 95

5.4.1 Temperature change 96
5.4.2 Space conditions 96
5.5 TPV experiments 98
5.5.1 No filter case 98
5.5.2 Filter case 100
5.5.3 Cell temperature comparison 102
5.5.4 Temperature gradients across coolers 102
5.5.5 Weight and performance comparison 104
6 Conclusion 106
6.1 Future work 108
7 References 111

List of figures

Figure 1-1: Components of a typical TPV system 1
Figure 1-2: (a) Ideal performance [6] (b) Bandgap energy of common semiconductor materials against temperature. [7] 3
Figure 1-3: Impact of cell temperature on TPV cell efficiency at different bandgaps and emitter temperatures [1] 4
Figure 1-4: (a) TPV efficiency history [10] (b) Heat to power conversion efficiency vs temperature for different systems [11] 5
Figure 2-1: (a) Conduction example (b) molecular structure 8
Figure 2-2: Surface roughness at an interface [17] 9
Figure 2-3: (a) Impact of contact pressure on conductance (b) Impact of temperature on conductance [18] 11
Figure 2-4: Example of a thermal circuit [17] 14
Figure 2-5: (a) CubeSat in space [18] (b) Diagram showing radiation rays 15
Figure 2-6: 2000 ASTM Standard Extraterrestrial Spectrum Reference E-490 [19] 16
Figure 2-7: Incident ray on an object 16
Figure 2-8: Reflectance data for AZ-400 paint [20] 17
Figure 3-1: (a) Spacecraft louvers [14] (b) Model showing louver mechanism [15] 18
Figure 3-2: AMDROHP design [16] 19
Figure 3-3: Actuator controlled triangular fin array [17] 19
Figure 3-4: Deep-space explorer deployable radiator [18] 20
Figure 3-5: (a) Thermal louver top view (b) labeled design [24] 20
Figure 3-6: NASA/Texas A&M SMA Morphing Radiator 21
Figure 3-7: BYU Radial Fin 21
Figure 3-8: BYU Triangular Fin 21
Figure 3-9: Nagoya University reversible thermal panel 22
Figure 3-10: AMDROHP 22
Figure 3-11: Utah State University Active Thermal Architecture 22
Figure 3-12: JAXA Re-Deployable Radiator 22
Figure 3-13: ACT 3D Printed LHP with Deployable Radiator 22
Figure 3-14: Vought Corp Flexible Radiator 23
Figure 3-15: Alphabus Extension deployable panel radiator 23
Figure 3-16: Sierra Space - Miniature Satellite Energy-Regulating Radiator (MiSER) 23
Figure 3-17: DcubeD (aka FENNEC) Deployable Radiator 23
Figure 3-18: Sierra Space - Passive thermal louver (20 blades) 23
Figure 3-19: Thermal Management Technologies - Deployable Radiator 24
Figure 3-20: Redwire Space Q-Rad 24
Figure 3-21: ThermAvant oscillating heat pipe (OHP) radiator 24
Figure 3-22: Swales Aerospace - Alpha Deployable Radiator 24
Figure 3-23: ThermAvant unspooling OHP radiator 24
Figure 3-24: Dellingr CubeSat louver 25

Figure 3-25: Pumpkin/YSPM Rollout Deployable Radiator 25
Figure 3-26: Comparison of cooling power and weight for multiple radiative cooling structure designs [28] [23] [27] [38] [27] [34] 27
Figure 3-27: Number of incidences by material in radiative coolers 28
Figure 3-28: Comparison of density and thermal conductivity of materials 29
Figure 3-29: Carbon fibre composites density vs thermal conductivity 30
Figure 3-30: Thermal strap [48] 32
Figure 3-31: Parker Chomerics THERM-A-GAP 579 thermal pad [50] 32
Figure 3-32: Solar absorptivity and total hemispherical emissivity values for various paints and films used for conventional thermal control and smart radiation devices (SRD) [58] [59] 36
Figure 3-33: Large-scale thermal vacuum chambers (a) NASA [60] (b) Phenix facility [61] (c) EASA CubeSat support facility [62] 37
Figure 4-1: (a) 2D revolution geometry (b) Resulting model 38
Figure 4-2: Mesh close-up 40
Figure 4-3: Thermal circuit diagram 40
Figure 4-4: Fixed volume cases (a) 3 cm radius (b) 15 cm radius (c) 30 cm radius 41
Figure 4-5: Example of a panel configuration 42
Figure 4-6: (a) Cross-section (b) Model layout from top view (c) COMSOL model with location of applied heat flux shown 43
Figure 4-7: Sandwich structure with 9 sections with material legend 45
Figure 4-8: Cross-section of various circular multi-material structures with weight 45
Figure 4-9: Experiment's vacuum-based setup for testing the radiative coolers 47
Figure 4-10:(a) Experimental setup (b) Ceramic thermal insulator 48
Figure 4-11: Experimental setup showing shelf, vacuum chamber, pump, power supply and benchtop controller 49
Figure 4-12: Vacuum chamber model 49
Figure 4-13: Temperature gradient across cooler for different ambient temperatures. 50
Figure 4-14: (a) Vertex 70 FTIR spectrometer (b) Integrating sphere 51
Figure 4-15: FTIR absorptance result for black aluminum tape 52
Figure 4-16: Support for the radiative cooler 53
Figure 4-17: (a) Behaviour of a PTC ceramic heater [68] (b) heating element [67] 53
Figure 4-18: (a) Heating element used (b) Radiative cooler 54
Figure 4-19: Radiative cooler component dimensions (a) aluminum panel (b) copper center 54
Figure 4-20: Radiative cooler without ceramic pieces 55
Figure 4-21: (a) Skytoppower STP6005H (b) Labjack T7 56
Figure 4-22: (a) Halogen bulb (b) TPV cell (c) photon reflector and selective filter (d) close-up of cell and filter 57
Figure 4-23: Spectral filter transmission spectrum [72] 58
Figure 4-24: Complete TPV testing setup 59
Figure 4-25: Circuit for IV curve measurements 60
Figure 4-26: (a) Full geometry (b) Quarter geometry (c) Maximum temperature as a function of the number of mesh elements 61

Figure 4-27: Thermal conductivity of multiple (a) copper samples (b) aluminum samples against temperature [73] 62
Figure 4-28: Power error measurements 63
Figure 4-29: (a) Radiative cooler with the heating element and thermocouples (b) Location of thermocouples 64
Figure 4-30: Temperature measurements (a) copper and heat element intersection (b) panel intersections 65
Figure 4-31: Size iterations 68
Figure 4-32: Worse case radiation from the sun and Earth on the radiative cooler. [75] 69
Figure 4-33: (a) TPV setup in use (b) zoomed in illuminated TPV cell 70
Figure 5-1: Flowchart depicting steps followed for the design of the multi-material radiative cooler 72
Figure 5-2: (a) Simulation results for a radius of 12.3 cm (b) Temperature gradient across surface 73
Figure 5-3: Temperature gradient across cooler for different radii at uniform thickness 74
Figure 5-4: Simulation results for the impact of thicknesses of a copper radiative cooler with a radius of 15 cm on cell temperature 75
Figure 5-5: Fixed volume analysis with a constant volume of 70.7 cm^3 76
Figure 5-6: Comparison of coolers made of different materials 77
Figure 5-7: (a) Cross-section showing material locations (b) Results of horizontal material sweep 78
Figure 5-8: Temperature at center comparison for horizontal cases 79
Figure 5-9: (a) Illustration of vertical cross-section (b) results for vertical case 80
Figure 5-10: Temperature at center comparison for vertical cases 81
Figure 5-11: (a) Illustration of diagonal cross-section (b) Results for diagonal cases 82
Figure 5-12: Temperature at center comparison for diagonal cases 83
Figure 5-13: Comparison chart of horizontal cases 84
Figure 5-14: Experimental results for (a) PTC heating element tests (b) various radiative coolers 86
Figure 5-15: FTIR results for black ceramic paint on aluminum surface 88
Figure 5-16: Thermocouple readings across 4 different areas 89
Figure 5-17: FTIR results for ceramic glued to heating element 90
Figure 5-18: Copper and heating element conductance test 91
Figure 5-19: Power results using power supply and measurements inside vacuum chamber 92
Figure 5-20: Comparison of temperature gradient across cooler for experimental and simulation results 93
Figure 5-21: Constrained case results (a) temperature drop/weight vs temperature (b) weight vs temperature 94
Figure 5-22: Results for unconstrained case at room temperature (a) temperature drop/weight vs temperature (b) weight vs temperature 95
Figure 5-23: Comparison of temperature gradient across cooler surface at 298 K and 3 K 96
Figure 5-24: Comparison of temperature gradient across cooler surface at 298 K, 3 K and in space conditions 97

Figure 5-25: (a) Photo of cell during experiment without filter (b) IV curves for different cases 98
Figure 5-26: Maximum power point calculated for no filter cases 99
Figure 5-27: (a) Photo of cell during experiment with filter (b) IV curves for different cases .. 100
Figure 5-28: Maximum power point calculated for filter cases 101
Figure 5-29: Cell temperature comparison with and without spectral filter 102
Figure 5-30: Temperature gradient across coolers using (a) no filter (b) filter 103
Figure 5-31: (a) Comparison between power output and weight (b) Comparison between cell temperature and weight 104
Figure 6-1: Results of this work compared to existing radiative coolers 107

List of tables

Table 3-1: Properties of designed deployable radiative cooling structures 21
Table 3-2: Properties of coatings used in space 34
Table 4-1: COMSOL parameters for feasibility analysis 39
Table 4-2: List of material combinations for disk-shaped cooler simulations 44
Table 4-3: COMSOL parameters used for panel configuration cases 44
Table 4-4: Horizontal material combinations used in COMSOL simulations 46
Table 4-5: Vertical material combinations used in COMSOL simulations 46
Table 4-6: Diagonal material combinations used in COMSOL simulations 47
Table 4-7: Comparison of material properties 55
Table 4-8: COMSOL validation simulation parameters 66
Table 5-1: Description of experimental cases 85
Table 5-2: PTC heating element experimental results 87

List of symbols

Symbol	Full expression	Units
ΔT	Temperature change	K
A	Area	m^2
C	Conductance	$W/m^2 \cdot K$
c	Speed of light	m/s
C_1	Radiation constant	$W \cdot \mu m^4/m^2$
C_2	Radiation constant	$\mu m \cdot K$
C_T	Interfacial conductance	$W/m^2 \cdot K$
E	Radiative heat flux	W/m^2
E_b	Black-body emissive power	W/m^2
$E_{b\lambda}$	Spectral blackbody emissive power	W/m^2
E_{photon}	Photon energy	J
h	Convection coefficient	$W/m^2 \cdot K$
H	Planck's constant	Js
h_r	Radiative coefficient	W/mK
K	Thermal conductivity	W/mK
L	Length	M
P_{in}	Power input	W
q_{cond}	Conduction heat flux density	W/m^2
q_{conv}	Convection heat flux density	W/m^2
q_{rad}	Radiative power	W
r	Radius	Cm
R_{cond}	Thermal resistance - conductive	K/W
R_{conv}	Thermal resistance – convective	K/W
R_{rad}	Thermal resistance – radiative	K/W
R_T	Thermal contact resistance	$m^2 \cdot K/W$
T	Temperature	℃
t	thickness	cm
T_{bottom}	Bottom surface temperature	K
T_{cell}	Cell temperature	K
T_{top}	Top surface temperature	K
T_∞	Temperature of fluid	K
T_s	Surface temperature	K
T_{surr}	Temperature of surroundings	K
V_c	Constant volume	cm^3
E	Emissive power	W
ε	Emissivity	
λ	Wavelength	m
σ	Stefan-Boltzmann's constant	$W/m^2 \cdot K^4$

List of abbreviations

Abbreviation	Full expression
AMDROHP	Additively Manufactured Deployable Radiator with Oscillating Heat Pipes
CFRP	Carbon Fibre Reinforced Polymer
CVCM	Collected Volatile Condensable Materials
ISS	International Space Station
JAXA	Japan Aerospace Exploration Agency
LEO	Low Earth Orbit
LHP	Loop Heat Pipe
MiSER	Miniature Satellite Energy-Regulating Radiator
NASA	National Aeronautics and Space Administration
NFRA	Near-Field Radiation Assisted
OHP	Oscillating Heat Pipe
PTC	Positive Temperature Coefficient
SMA	Shape Memory Alloy
SRD	Smart Radiation Devices
SRDM	Smart Radiation Devices with Multilayer films
SSO	Sun Synchronous Orbit
TML	Total Mass Loss
TPV	Thermophotovoltaic

1 Introduction

1.1 Problem introduction

Thermophotovoltaic (TPV) systems have been the subject of an increasing number of studies in recent years regarding thermal batteries, waste heat recycling as well as combined heat and power generation amongst others. TPV cells generate electricity via the conversion of infrared light emitted from a heated source. A typical modern TPV system, as shown in Figure 1-1, consists of a heat source, an emitter, a spectral filter, TPV cells, photon reflectors, and a cooling system. [1]

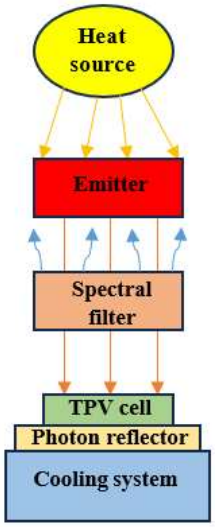

Figure 1-1: Components of a typical TPV system

The emitter is heated to high temperatures ranging from about 1000 K to 2400 K by a heat source which can be concentrated solar power, recycled waste heat, nuclear-based systems, combusted fuel, or combinations of the aforementioned. As a result, the emitter gains sufficient energy and begins emitting photons that are used by a TPV cell to generate electricity. The chosen emitter needs to have high emissivity in the IR range while being robust enough to withstand high temperatures for long periods of time, hence, tungsten is commonly used as the emitter material. Recent research in the TPV field explores other emitter materials such Aluminum Nitride/Tungsten (AlN/W) bilayers, which have demonstrated potential for over 49% efficiency with GaSb cells, a significant improvement over tungsten. [2]

The TPV cells, typically made of GaSb or InGaAs, can solely convert in-band photons, which possess energy greater than the semiconductor band-gap, into electricity. [3] GaSb, for example, has a bandgap of 0.72 eV and operates at wavelengths below 1700 nm. [4] A spectral filter is used to filter out out-of-band photons and a photon recycler, which can be a gold mirror, is used to reflect light. When the photons reach the TPV cells, electron-hole pairs are created and as the electrons get separated from the holes, an electric current can be generated and used in an external circuit. For optimal operation, a cooling system is needed to maintain the TPV cells as

close as possible to their chosen operating temperature thereby maintaining high cell efficiency and preventing any damage.

The distinct advantages of TPV systems are their relatively high heat-to-power conversion efficiencies and simplistic structure which allow them to be light-weight without any moving parts. TPV systems are also recognized as an effective means of waste heat recovery which can lead to higher system efficiencies. [5] These factors make TPV systems particularly suitable for space applications, especially for small spacecrafts, since there is a reduced risk of failure, lower payload, and a suitability for long-term missions.

Furthermore, solar-powered TPV systems can in theory reach a maximum efficiency of 85% with full sunlight concentration which is significantly better than conventional photovoltaic cells directly exposed to sunlight that have their maximum efficiency capped by the Shockley-Queisser limit of 41%. [6] Another problem that could be resolved by a TPV system is the ability to generate electricity at all times through the use of alternate heat sources or thermal energy storage that can be used when there is no sunlight available. This makes the technology more suitable for grid-scale applications since the system would not require any alternate power sources to support uninterrupted power generation. TPV converters have been designed for thermal batteries with 23.2% efficiency at 1.34 W/cm^2. [7] These batteries compensate for interruptions experienced by, for example, solar energy-based power systems.

The focus of this research is on improving cooling for TPV systems that operate in outer space. The temperature of the cell is preferably maintained at a level that can generate a maximum amount of electrical power. The output of a TPV cell typically increases as its temperature decreases, however, extremely low temperatures may cause damage as some electronic components may not function as intended.

Figure 1-2 (a) shows the ideal absorptance spectrum for a PV cell with a bandgap energy of 0.67 eV.

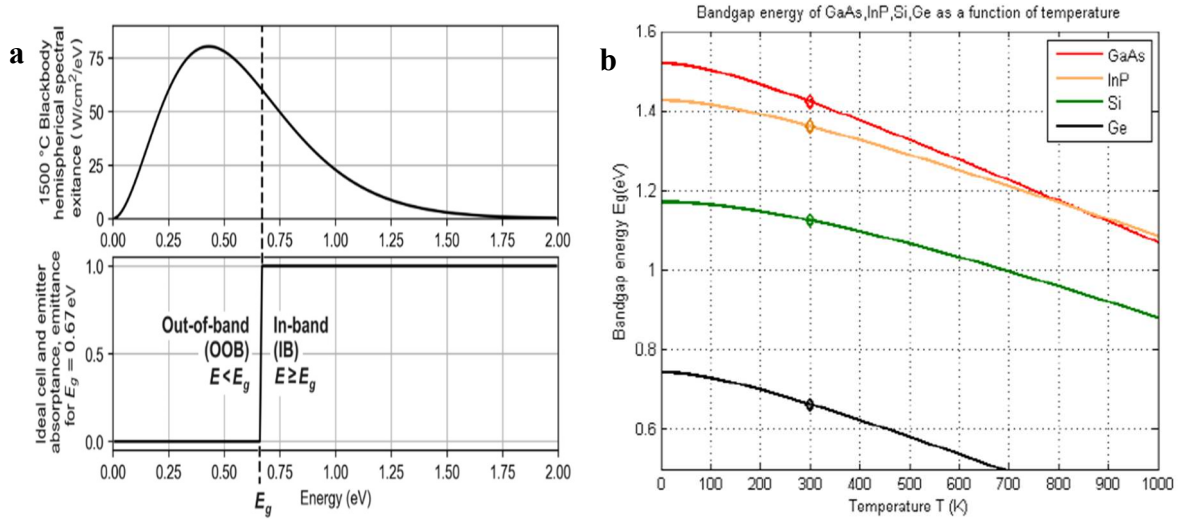

Figure 1-2: (a) Ideal performance [8] (b) Bandgap energy of common semiconductor materials against temperature. [9]

The bottom figure in Figure 1-2 (a) presents the ideal emittance spectra for an emitter operating in a TPV system with a PV cell that has a bandgap of 0.67 eV. All photons radiated from this emitter are in-band and contribute towards improved performance. The highest efficiency reachable by a TPV cell is affected by thermalization losses. The latter occurs when a photon with energy significantly higher than the bandgap is absorbed. The photon energy is transferred to an electron that leaves the conduction band but release its excess energy on its return. This energy is not converted into electrical energy but is instead lost as heat within the cell leading to an increase in the cell's temperature. [10] As a result, there is a greater amount of dark current generated which is current flowing in the reverse direction of photocurrent without contributing to electricity generation. The top graph in Figure 1-2 (a) shows the emission spectrum from a blackbody surface at a temperature of 1500 ℃. The majority of photons emitted from a blackbody at 1500 ºC are out-of-band (having energy less than the band-gap) when the band-gap energy is 0.67 eV. To increase the ratio of in-band photons, the bandgap energy needs to be reduced as much as possible. Figure 1-2 (b) shows how the bandgap energy changes as a function of temperature for certain semiconductor materials. It can be observed that a higher temperature leads to lower bandgap energy, which would lead to more photons being in-band. This would imply that a higher temperature would generate more electricity, however, this is not the case in practice as the performance of a TPV cell worsens with increasing temperature. This occurs due to an increase in dark current, which negatively impacts cell efficiency more significantly than bandgap changes, resulting in reduced performance. [1] Figure 1-3 shows the efficiency of PV cells as a function of increasing cell temperature for different bandgaps and varying emitter temperature.

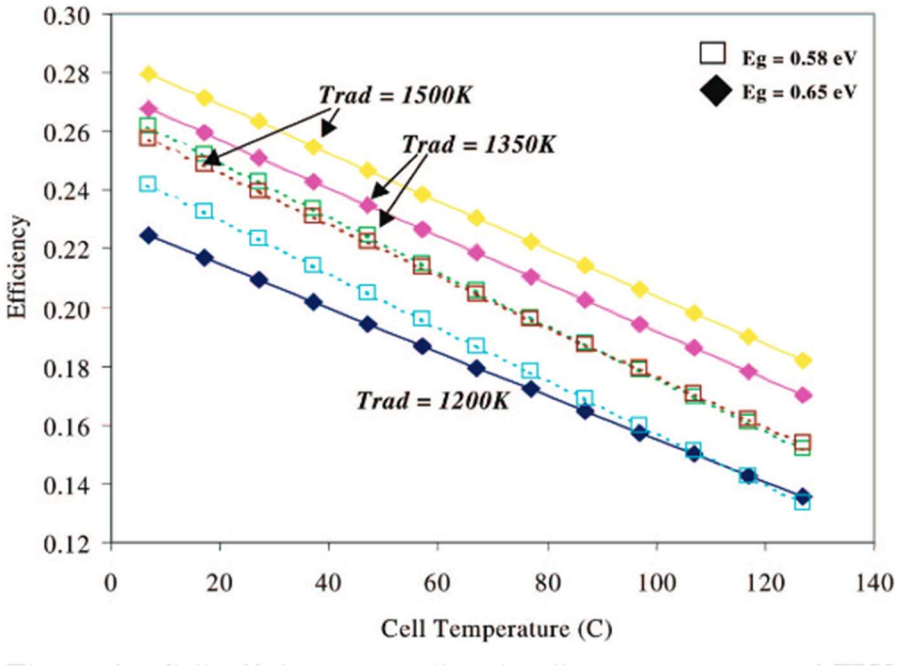

Figure 1-3: Impact of cell temperature on TPV cell efficiency at different bandgaps and emitter temperatures [1]

It can be observed from Figure 1-3 that cell efficiency worsens with increasing cell temperature irrespective of bandgap or emitter temperature. Conversely, efficiency increases as emitter temperature increases for a given cell temperature and bandgap. Furthermore, for a given cell temperature, the efficiency is higher for the lower bandgap case when exposed to 1200 K illumination. However, at higher temperatures, this is no longer the case, as the higher emitter temperature cases with larger bandgaps have higher efficiencies. This can be explained by the fact that at higher temperatures, there are large enough amounts of in-band photons at both bandgaps leading to a lesser impact on efficiency. A larger bandgap leads to a higher voltage and in the presence of sufficient photons, it leads to higher efficiency. Moreover, excessive numbers of high energy photons at the lower bandgap leads to increased thermalization losses and thus, higher dark current leading to lower efficiency. The main takeaway for the purpose of this research is the relation between cell temperature and efficiency. To maximize efficiency, the temperature of a TPV cell needs to be as low as possible.

1.2 Research gap

TPV technology was first introduced by Wedlock in 1963 whereby a power density of 10 W/m^2 and a conversion efficiency of 30% were theorized. [11] Based on this idea, the first solar energy-based TPV system was formulated by Swanson in 1979. [12] At that time, the conversion efficiency of 29 % was achieved and this remained the highest attained for several decades until the recent increased interest in TPV contributed to several breakthroughs in terms of cell efficiency. An efficiency of 31% was reached in 2020 followed by a record 41.1% in 2022, hence, surpassing the threshold representing the efficiency of a steam turbine. [13] Figure 1-4 (a) shows the efficiency achieved by different researchers over the years until 2022.

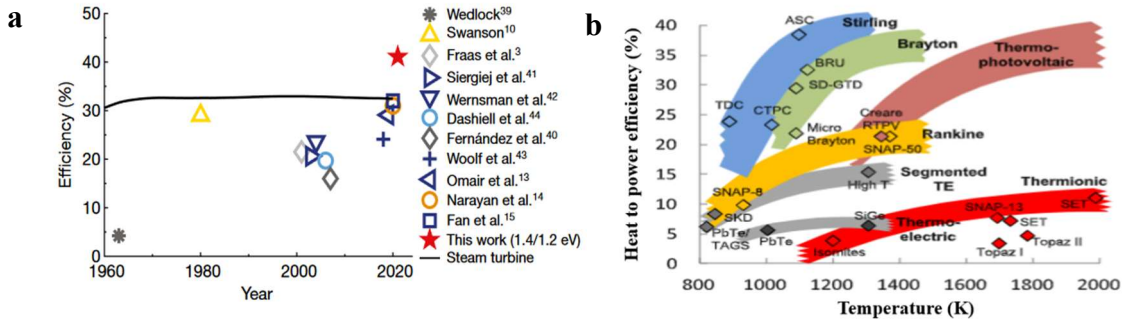

Figure 1-4: (a) TPV efficiency history [13] (b) Heat to power conversion efficiency vs temperature for different systems [14]

More recently, in 2024, a new TPV cell efficiency record of 44% was achieved wherein the emitter was made from SiC and was at a temperature of 1435 ℃. [15] In comparison, the efficiency of 41.1% measured in 2022 was achieved with a tungsten halogen bulb reaching 2400 ℃. [13] These recent breakthroughs have renewed interest in the TPV technology as it allows for greater power density while demonstrating rapid technological progress and increasing potential. As shown in Figure 2 (b), TPV systems have the highest heat to power conversion efficiency at high temperatures among systems which do not require moving parts or fluids. Despite this advantage, historically, thermionic and thermoelectric systems are the only ones used in space applications thus far. The main reasons TPV cells have not yet been used for space applications are that they require large radiators to keep the TPV cells cool, TPV was and is still an unproven technology for long term space missions, and due to the possibility that degraded materials would lead to the contamination of optical elements in the system. [16] However, with increased efficiencies, the weight of TPV systems can be reduced, and their higher power densities are increasing their viability for space applications.

Existing cooling systems operating in space mainly use liquid cooling systems. For a TPV system used for a small satellite or CubeSat, the cooling needs to be more localized since the undesired heat is in close proximity to where the PV cell is located. Hence, existing cooling systems are not well adapted for these types of systems.

Space vessels rely on the slow process of radiation for cooling. Liquid cooling systems typically collect heat across the vessel and transfer it to an external radiator that rejects it into deep space. For CubeSats, due to their standard designs and low payload, their cooling is done via their

external walls which effectively limits their cooling capacity. Assuming an operating temperature of 300 K, a 3U CubeSat has a maximum cooling capacity of 60 W considering its surface area of 0.14 m^2. [17] A solution for this limitation is the use of deployable radiative coolers that can be compactly stowed at take-off before being deployed in space. This minimizes the space needed for the coolers while increasing cooling capacity. A purely radiative cooling system has a lower mass compared to liquid cooling systems.

For space vessels, launch costs have historically been a major economic constraint but there has been significant progress in recent years. As of May 2025, SpaceX's Smallsat rideshare program charges $325,000 per payload of 50 kg and under for Sun Synchronous Orbit (SSO) projects. This results in a price as low as $6500/kg though this is contingent on the payload reaching 50 kg. [18] In comparison, NASA's space shuttle launch to Low Earth Orbit (LEO) cost $54,500/kg. [19] This drop in launch costs spurred an increasing number of small satellite projects. Nonetheless, minimizing weight is still desired in many projects with limited budgets.

Currently, there are very few papers focused on the cooling of TPV systems in space. Hence, this research will be focusing on designing a lightweight passive radiator that keeps the TPV cells cool while occupying a small amount of space during takeoff. The focus will be on making the system suitable for a small satellite or a CubeSat. As a solution to this problem, the use of multi-material deployable structures will be investigated since they have the ability to be compact during takeoff and deploy in space where there is more space available. By integrating materials with lower density into the radiative cooler, the overall system weight can be significantly reduced.

1.3 Objective statement

Based on the research gap discovered and background research regarding existing designs, the three following objectives were chosen for this research:

- Objective 1: Use numerical modeling to design a multi-material deployable radiative cooler with high cooling performance, and low volumetric and gravimetric densities.

  This objective uses COMSOL numerical modeling to predict the behaviour of radiative coolers in space. A parametric study is carried out to determine the best multi-material cooler capable of providing adequate cooling power while being relatively lightweight.

- Objective 2: Build a vacuum based experimental setup to test the radiative coolers.

  The radiative cooler designed in objective 1 needs to be tested in order to validate the simulations and ensure they behave in the real world as predicted by theoretical simulations. The space-like environment needs to be created in the lab with the use of a vacuum chamber. The complete setup is designed taking into consideration performance measurement requirements and built accordingly.

- Objective 3: Using the experimental apparatus from objective 2, build a multi-material cooler and measure its ability to cool a TPV cell within a TPV system.

The radiative cooler performance as part of an actual TPV system is key to demonstrate its effectiveness. It is built and used inside the experimental setup to cool a TPV setup exposed to a sizeable heat flux to prove its cooling capabilities.

1.4 Thesis outline

The thesis is structured to provide adequate background information before proceeding into methodology details and results obtained. The outline is as follows:

- Chapter 2: Relevant theory

  This chapter provides information regarding technical information used throughout the thesis. A brief overview of heat transfer concepts is given along with relevant mathematical equations before exploring the space environment and its thermal impact on a vessel such as a CubeSat.

- Chapter 3: State of the art and literature review

  A review is carried out on existing radiative coolers and their performance metrics prior to exploring their different components namely the materials used, thermal interfaces for heat transfer, and coatings applied on external surfaces. In line with objective 2, a short review is also done regarding thermal vacuum chamber testing.

- Chapter 4: Method

  The methodology used to achieve the three objectives of this research is discussed in Chapter 4 with details provided on COMSOL simulations, the assembly of the experimental setup, and how experiments were carried out in the lab.

- Chapter 5: Results and discussion

  Chapter 5 shows the results obtained after following the steps outlined in Chapter 4 and provides a discussion that links these results to the theory and background information provided in Chapters 2 and 3.

- Chapter 6: Conclusion and future work

  The final chapter provides conclusions based on final research outcomes. The next steps needed to improve the designed radiative cooler and make it suitable for practical use are listed as part of future work.

2 Relevant theory

This chapter examines the relevant theory and key equations that will be needed for this research. The concepts are concisely explained with emphasis on cooling mechanisms and their relevance to the thesis objectives. In outer space, due to the lack of air, heat transfer mainly occurs through conduction and radiation. Heat transfer occurs through and between materials by conduction and this heat is transmitted into outer space through radiation via the external surfaces. Convection does occur in cases where liquid cooling is utilized or inside a space vessel where air is present, although these applications are not relevant to the research carried out in this thesis.

2.1 Conduction

Conduction is the transfer of heat via the vibrational motion of molecules or atoms within a lattice without any bulk motion in the material itself and it is governed by Fourier's law of heat conduction shown in Equation 1 below: [20]

$$q_{cond} = -kA\frac{\Delta T}{L} \qquad \text{Equation 1}$$

Where q_{cond} is the heat flux, k is the thermal conductivity coefficient, A is the area, L is the length and ΔT is the temperature difference. Figure 2-1 (a) shows a conduction example where the heat transfer from one end of a block to the other is considered.

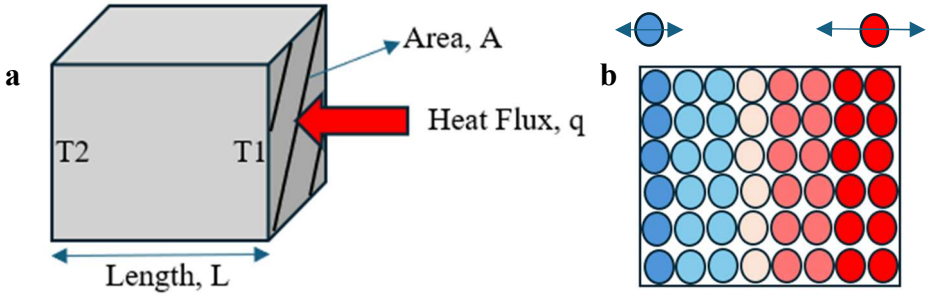

Figure 2-1: (a) Conduction example (b) molecular structure

It can be observed that the area considered is normal to the applied heat flux while the length is the distance along which the heat travels. ΔT is the difference between T1 and T2. Figure 2-1 (b) is a simple representation of what the structure looks like on a molecular level. Heat is transferred from molecule to molecule as they collide with each other. The hotter red colored molecules vibrate faster as the greater heat energy they possess is translated into higher kinetic energy. The heat spreads across the whole structure until it reaches steady state equilibrium which is the point in time where there is no longer any change in temperature assuming there is no change in the incoming heat flux or external conditions.

Conduction takes heat away from a hotter region and transfers it to a cooler region. In order to do so effectively, and the rate at which heat transfer occurs depends on the thermal conductivity of the material. Equation 1 can be rearranged to form Equation 2 as follows:

$$k = -\frac{q_{cond}L}{A\Delta T} \qquad \text{Equation 2}$$

The thermal conductivity coefficient, k, is related to thermal conductance, C, as per Equation 3:

$$C = \frac{k}{L} \qquad \text{Equation 3}$$

Another term related to conductance is the thermal contact resistance, R_t, which is the inverse of conductance as shown in Equation 4:

$$R_t = \frac{1}{C_t} \qquad \text{Equation 4}$$

R_t represents the resistance to heat transfer occurring across an interface. The higher the thermal contact resistance, the slower the heat transfer and, inversely, the higher the conductance, the quicker the heat transfer can occur. The conductance across an interface between two materials depends on a multitude of factors namely:

1. Surface roughness
   Since conduction occur at the interface between two materials, the surface roughness can greatly impact conductance values. Figure 2-2 shows the interface between two materials with rough surfaces.

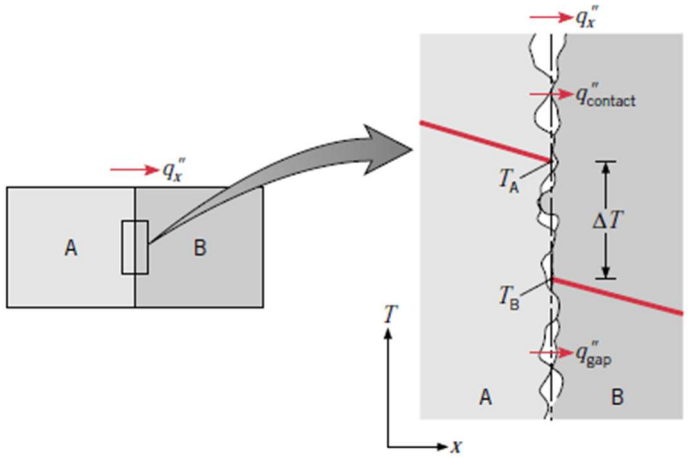

Figure 2-2: Surface roughness at an interface [20]

It can be observed in Figure 2-2 the contact area between the two materials with rough surfaces is not as large as the interfacial area looks to the naked eye. At a microscopic level, the surface imperfections between materials cause gaps between the materials and reduce the actual contact area. Depending on how polished the surfaces are and what their surface roughness is, the conductance can vary greatly. Two perfectly polished surfaces in contact with each other will have significantly higher conductance than two rough surfaces since the contact area will be greater.

2. Contact pressure

Two metals joined together under higher pressure will have better contact with each other as the applied pressure will improve the contact area between the two. As shown in Figure 2-2, a surface has asperities depending on its roughness. When pressure is applied, the peaks along the surface get compressed, hence, leading to less air gaps and better contact area. A surface with taller peaks, would need higher pressure to improve contact area and hence, conduction.

3. Temperature and applied heat flux

   The temperature is a direct result of the applied heat flux and hence, both are related to each other and can impact conductance. Since conduction occurs through the vibration of molecules or atoms within a material, the temperature also plays a role regarding conductance. A higher temperature would lead to higher kinetic energy held by the molecules or atoms which will vibrate more vigorously and hence, transfer heat quicker to each other allowing for a higher conductance. However, the rate of heat transfer depends on the temperature gradient between the two materials. The larger the difference in temperature, the greater the difference in vibrational kinetic energy possessed by the molecules, hence, allowing a net momentum transfer from the faster molecules or atoms to the slower ones. To summarize, the conductance value increases as the difference in temperature between two materials increases.

   High temperatures can also impact the material interface through deformations and phase changes in regions of high temperature and pressure that would change the conductance value. This would change the contact areas caused by the surface roughness and can hence, change the conductance value. In general, conductance increases with increasing temperature and pressure, however, the extent to which this happens is hard predict due its dependence on surface topography.

4. Trapped gases

   The gaps between the materials become filled with the surrounding air on Earth. In space, if the materials are in a vacuum, that space remains empty. With trapped gases present, conductance values are affected by a small amount of convection and radiation which allow heat to flow from one material to another. However, in space, when the gap between the materials remains empty, convective heat transfer does not occur, resulting in a slightly lower conductance value than would be observed on Earth. Additionally, convection increases with temperatures rise. Hence, the impact of trapped gases on conductance becomes more significant at higher temperatures.

The impact of these factors was demonstrated in the literature [21] using the interface between aluminum and copper alloys. In Figure 2-3, σ_s represents the surface roughness finish with 0.85 μm being the smoothest finish and 1.84 μm being the roughest finish.

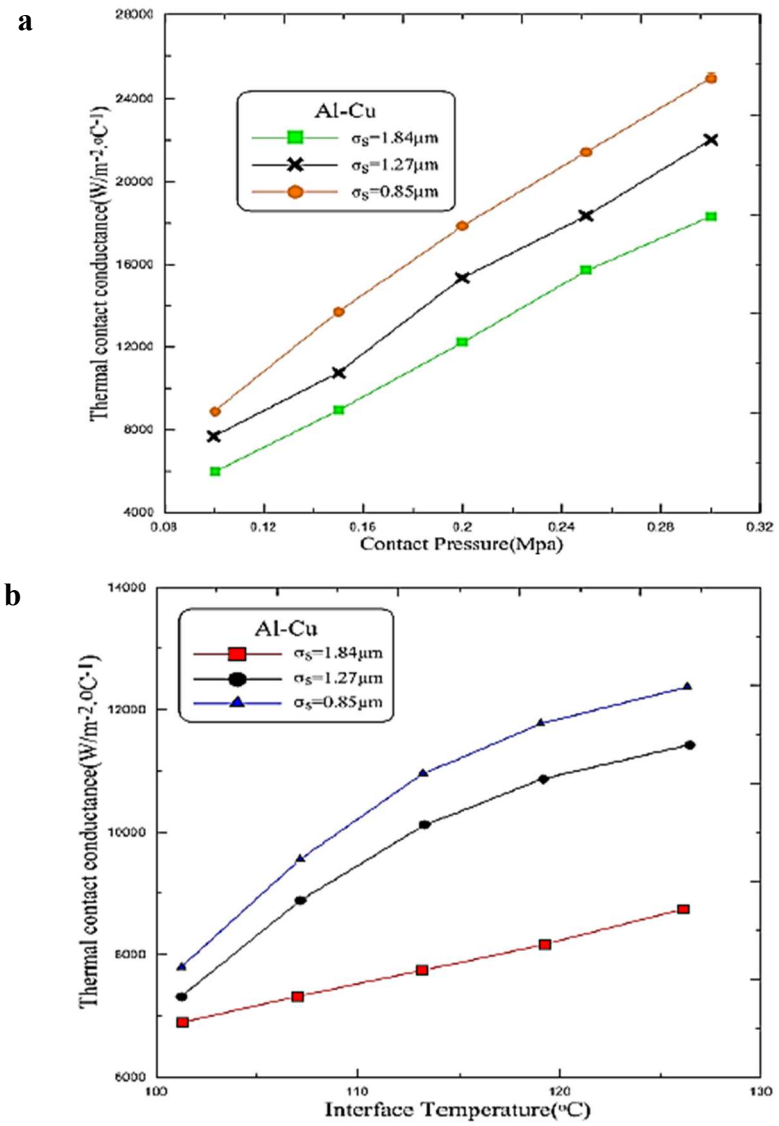

Figure 2-3: (a) Impact of contact pressure on conductance (b) Impact of temperature on conductance [21]

It can be observed that in both graphs the smoother surface finish has the highest conductance at all contact pressures and temperatures. This is expected as the contact area between the two materials is highest in this case. The impact of the contact pressure in Figure 2-3 (a) is shown to be significant. Considering the 1.84 μm surface roughness case, at a contact pressure of 0.10 MPa, the thermal conductance is around 6000 $W/m^2 \cdot K$. Doubling the contact pressure to 0.20 MPa leads to a thermal conductance of 12000 $W/m^2 \cdot K$. This is also caused by an increase in contact area induced by deformation at the contact points caused by the applied pressure. The impact of temperature is shown in Figure 2-3 (b). For all cases, conductance increases with increasing temperature. This occurs due to factors such as increase in vibrational kinetic energy of molecules or atoms, convection through trapped gases, as well as increase in contact area due to temperature induced surface deformations.

2.2 Convection

Convection is the transfer of heat through a fluid via the combined mechanisms of random molecular motion and bulk motion of the fluid itself. [20] Due to the presence of a vacuum in space, convection does not naturally occur as it requires a fluid as a medium. However, liquid cooling is commonly used internally within large structures with multiple systems generating heat as the liquid can circulate throughout the structure and cool down multiple systems at the same time. The liquid can then transfer this away to an external radiator through conduction. Convection is governed by Newton's law of cooling shown in Equation 5.

$$q_{conv} = hA\Delta T \qquad \text{Equation 5}$$

Where q_{conv} is the heat flux density, h is the convection coefficient, A is the surface area, and ΔT is the temperature difference.

2.3 Radiation

Radiative heat transfer occurs through the emission of photons by matter possessing a temperature above absolute zero. A photon is the smallest quantifiable unit within electromagnetic radiation and carries energy away from a body when emitted by that body. Unlike convective heat transfer a medium is not required for a photon to travel, and radiative heat transfer occurs in space. The energy possessed by a photon can be calculated using Equation 6:

$$E_{photon} = \frac{Hc}{\lambda} \qquad \text{Equation 6}$$

Where E_{photon} is the energy possessed by the photon, H is the Planck's constant (6.626×10^{-34} J/s), c is the speed of light (3×10^{8} m/s in a vacuum) and λ is the wavelength of the photon. Radiative heat transfer is governed by the Stefan-Boltzmann law shown in Equation 7.

$$E = \sigma \varepsilon T_s^4 \qquad \text{Equation 7}$$

Where E is the emissive power, σ is the Stefan-Boltzmann constant (5.67×10^{-8} W/m^2· K^4), ε is the surface emissivity, and T_s is the temperature of the surface emitting radiation. For engineering problems, the more commonly used form of this equation is shown in Equation 8.

$$q_{rad} = \sigma A \varepsilon (T_s^4 - T_{surr}^4) \qquad \text{Equation 8}$$

Where q_{rad} is the heat flux, A is the surface area, and T_{surr} is the temperature of the surroundings.

The emissivity of a surface represents the amount of radiation emitted by a surface relative to a black body as shown in Equation 9.

$$\varepsilon = \frac{E}{E_B} \qquad \text{Equation 9}$$

A black body has the highest possible emissivity value of 1 and is considered to be a perfect emitter due to its ability to absorb the maximum amount of radiation. Emittance and absorptance are related by the Kirchhoff's law of thermal radiation which states that the spectral directional absorptance of a body is equal to its spectral directional emittance at thermal equilibrium. [20]. Going back to Equation 6, we know that photon energy is a function of wavelength. Hence, emissivity is also dependent on wavelength. The emissivity of a black body in a vacuum can be found using Equation 10 derived from Planck's law.

$$E_{B\lambda} = \frac{C_1}{\lambda^5[e^{C_2/\lambda T} - 1]} \qquad \text{Equation 10}$$

Where $E_{B\lambda}$ is the blackbody emissive energy at a specific wavelength, $C_1(3.7418 \times 10^8\ \mathrm{W\,\mu m^4/m^2})$ and $C_2(14{,}388\ \mu\mathrm{m\ K})$ are radiation constants, λ is the wavelength, and T is the temperature. Planck's law in Equation 10 and Stefan-Boltzmann's law from Equation 8 can be combined along with Equation 9 for emissivity as shown in Equation 11.

$$\varepsilon = \frac{\int_{\lambda_1}^{\lambda_2} \varepsilon_\lambda E_{B\lambda} d\lambda}{\sigma T_s^4} \qquad \text{Equation 11}$$

In the numerator, the integral of the emissivity of the surface multiplied by the blackbody emittance at each wavelength is used to calculate the total emissivity of the surface. In the denominator, the emissivity of a black body is calculated using the Stefan-Boltzmann law.

Another factor to be considered is the direction of travel of the radiative rays emitted by a surface. Radiation occurs in all directions. Thus, the emission from a point result in radiation forming a hemispherical shape. There are four ways of measuring the emissivity of a body due to its dependence on wavelength and direction. They are as follows:

1. Spectral directional emissivity
   This provides information regarding rays with a specific wavelength and traveling in a specific direction.
2. Total directional emissivity
   Only one direction is considered, however, this value is integrated across all wavelengths in that specific direction.
3. Spectral hemispherical emissivity
   All directions are considered across the hemispherical shape of the emitted rays, however, only a specific wavelength is considered.
4. Total hemispherical emissivity
   This value is the most comprehensive measure of radiative emission with all directions and every spectrum evaluated.

These equations and measurements provide a brief overview of the concepts involved in this research and some of them will be referenced throughout this thesis.

2.4 Thermal circuit

Heat transfer problems are often represented by thermal circuits which are based upon electrical circuits. This allows for problems to be simplified into a simpler and easier to understand task. It is only used for problems where there is no internal heat generation and properties remain constant. In these circuits, resistances are found by using Fourier's law of conduction, Newton's law of cooling and the Stefan-Boltzmann law. The derived equations for the thermal resistances are shown below:

$$R_{cond} = \frac{T_1 - T_2}{q} = \frac{L}{kA}$$ Equation 12 [20]

$$R_{conv} = \frac{T_s - T_\infty}{q} = \frac{1}{hA}$$ Equation 13 [20]

$$R_{rad} = \frac{T_s - T_{surr}}{q_{rad}} = \frac{1}{h_r A}$$ Equation 14 [20]

These equations are used as part of the thermal circuits based on the heat transfer mechanism taking place and can be used to simplify a problem and calculate required variables such as an unknown surface temperature or a convection coefficient.

The temperatures of surfaces being considered as well as surroundings are also included in the thermal circuit. An example of a circuit diagram can be shown in Figure 2-4.

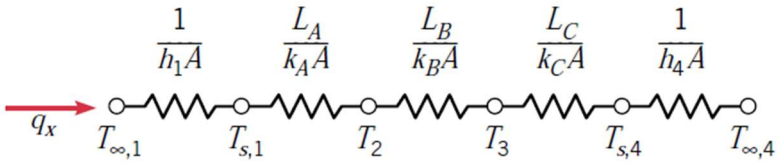

Figure 2-4: Example of a thermal circuit [20]

Figure 2-4 shows how a thermal circuit looks like with the incoming heat flux represented with an arrow. Temperatures are shown at every boundary where there is a change in heat transfer mechanism or a change in material. The corresponding coefficient for convective heat transfer or conductive heat transfer are used based on the material or fluid present.

2.5 Space environment

In space, the radiative cooler will be subjected to heat fluxes coming primarily from the TPV cell. However, there will be also a certain amount of radiation emitted from spatial bodies. To better understand radiation and to introduce other related terms, the example shown in Figure 2-5 (a) is considered.

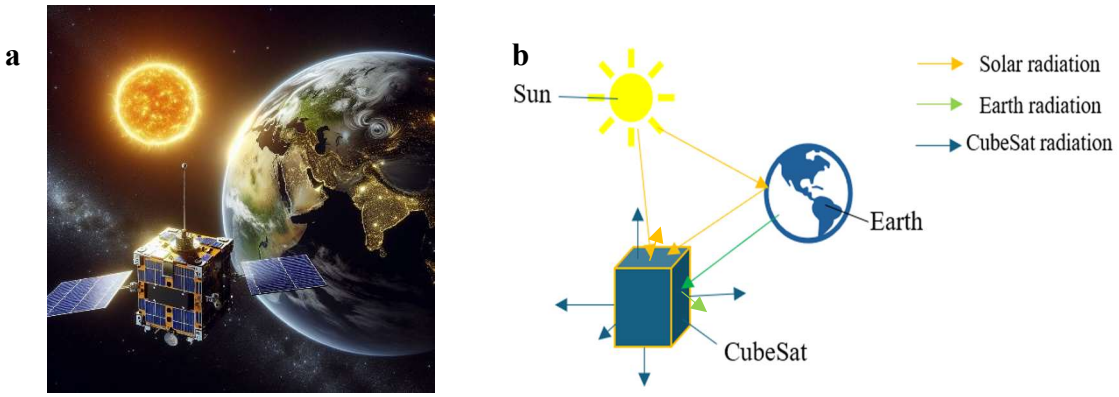

Figure 2-5: (a) CubeSat in space [18] (b) Diagram showing radiation rays

A CubeSat in space facing both the sun and the Earth is examined. The CubeSat, in Figure 2-5, is simplified as a cube and used in a drawing to show radiation pathways. It can be observed that the CubeSat receives radiation from 3 sources:

1. Radiation from the sun
2. Radiation from the Earth
3. Reflection of solar radiation off the Earth or more commonly known as the Earth's albedo.

This example also allows for the introduction of another key term in radiation: the view factor. The view factor essentially is a measure of the fraction of radiation that gets directly transferred from one surface to another surface. It is related to the surface positions in regard to each other and this affects the amount of radiation rays that are absorbed. From Figure 2-5, it can clearly be seen that the number of rays reaching a specific point on the CubeSat is determined by its position relative to the sun, and the Earth. If both are in front of the CubeSat, the backside does not receive any rays and hence, does not heat up nearly as much as the front of the CubeSat. That side is facing deep space and is transferring heat to it through radiative emission. The deep space temperature used in calculation is typically 3 K. Cooling is mainly done through the sides of the structure facing deep space due to the large temperature gradient. Referencing Equation 8, the lower the T_{surr}, the greater the amount of emissive heat losses. Hence, a radiative cooler should have a view factor as high as possible to deep space for maximized cooling and should minimize its view factor to itself that could arise with angled panels leading to reduced heat rejection.

The intensity of the radiation emitted by the sun vary based on wavelength. The solar radiation spectrum at air mass zero, which is in a vacuum, is shown in Figure 2-6.

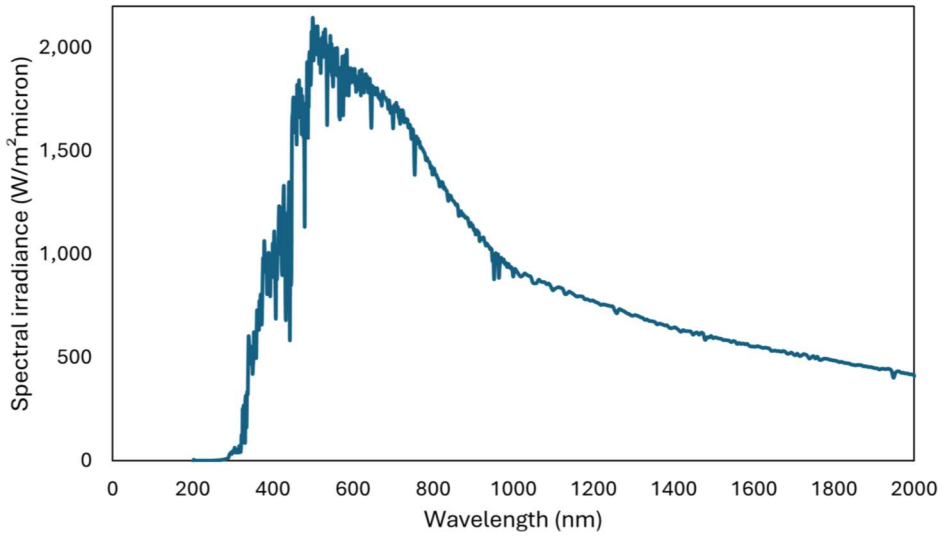

Figure 2-6: 2000 ASTM Standard Extraterrestrial Spectrum Reference E-490 [22]

The ASTM E-490-00 standard was created using solar irradiance data collected during space missions. It resulted in the spectrum shown above in Figure 2-6. In the space industry, the solar heat flux value commonly used is 1366.1 W/m^2 for satellites in orbit based on historical data. [22] Radiation incident onto a surface is either absorbed, reflected, or transmitted as shown in Figure 2-7.

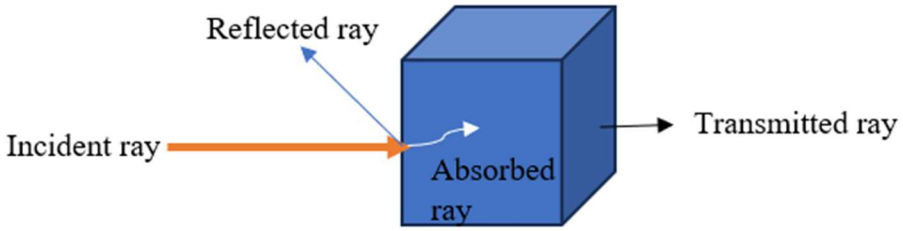

Figure 2-7: Incident ray on an object

This leads to the relationship shown in Equation 15:

$$Absorptance + Reflectance + Transmittance = 1 \qquad \text{Equation 15}$$

Since a radiative cooler is completely opaque its transmittance is 0 and incident radiation can only be absorbed or reflected. The amount of radiation absorbed or reflected depends on the radiative properties of the surfaces. Typically, a coating with low solar absorptivity and hence, high reflectivity, is used to minimize the amount of radiative heat transfer through solar radiation. Figure 2-8 shows the reflectance spectrum of a coating used in space, namely, AZ-400 from AZ technology.

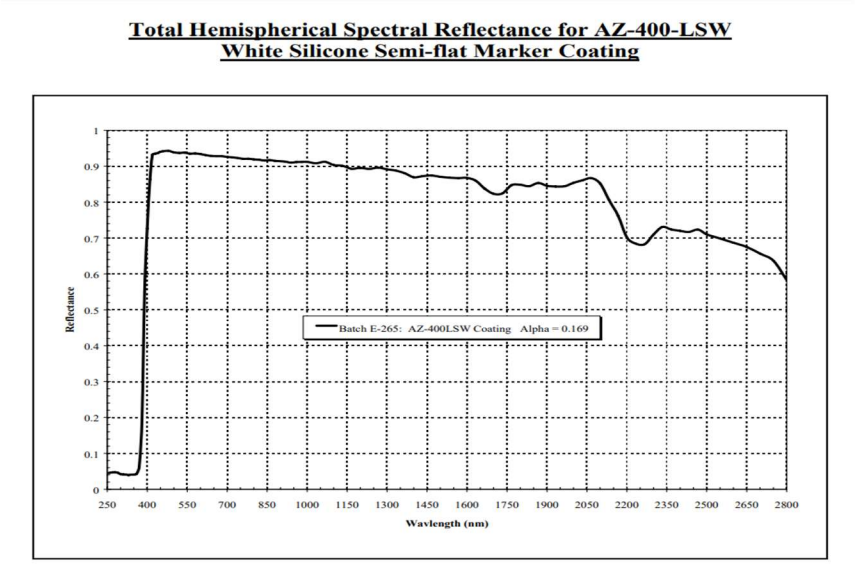

Figure 2-8: Reflectance data for AZ-400 paint [23]

A comparison between the ASTM E-490-00 solar radiation spectrum from Figure 2-6 and the reflectance data above in Figure 2-8 shows that this coating has high reflectivity in the same wavelength range of 400 nm to 2000 nm where the solar irradiance is the highest. This coating only absorbs 16.9% of the incoming solar radiation and reflects the rest, thus, contributing to the thermal management of a space structure such as a CubeSat as shown in Figure 2-5. Since the albedo of the Earth is simply a ratio measuring the reflection of solar radiation attenuated by the Earth's atmosphere and surface absorption, the coating is still suitable to reflect the majority of incoming radiation. On the other hand, the emission spectrum of the Earth happens at higher wavelengths above 6000 nm. However, due to the temperature differences between the sun (5777 K) and the Earth (300 K), the impact of radiation from Earth on heating is significantly lower.

The radiation absorbed by the CubeSat would cause its temperature to rise and hence, cause an increase in emission through radiative heat transfer as per Stefan-Boltzmann law. This information about the space environment is key for simulations and designing a cooling solution.

3 State of the art and literature review

In this chapter, existing cooling systems used in space are reviewed in depth with their operational performance compared and a deeper dive into materials and coatings used based on literature reviews and NASA reports.

3.1 Existing cooling systems in space

Space missions involve the use of multiple heat generating components such as electronics and propulsion systems. It is critical to manage that heat via a lightweight efficient cooling system to ensure continuous operation of all systems while limiting payload. There are various such systems with different designs based on multiple factors including the size of the spacecraft, cooling demand, location of electronics, weight or available space amongst others. In practice, large spacecraft or space stations are cooled using liquid cooling systems comprising of refrigerants such as anhydrous ammonia flowing throughout the whole structure before being directed towards louvers that provide a large surface area for heat dissipation to occur. Figure 3-1 (a) and (b) below show the radiators that form part of the cooling system used on the International Space Station (ISS) along with a demonstration of its deployment mechanism.

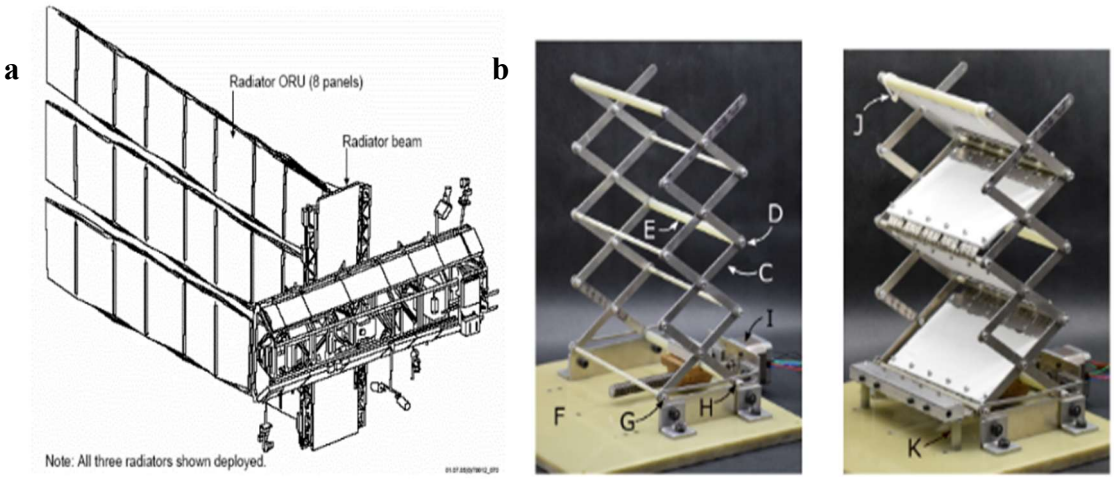

Figure 3-1: (a) Spacecraft louvers [14] (b) Model showing louver mechanism [15]

Figure 3-1 (a) shows the fully deployed form of the radiator when in space while Figure 3-1 (b) shows a model of how the louver mechanism operates. The ISS has high cooling demand due to its large size, large number of power intensive equipment and the fact that it is manned. It has a cooling power capability of 70 kW. [24]

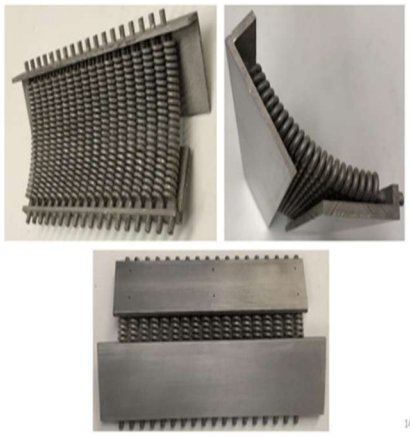

Figure 3-2: AMDROHP design [16]

Figure 3-2 shows an additively manufactured deployable radiator with oscillating heat pipes (AMDROHP) which is a two-phase liquid cooling structure recently designed for CubeSat missions. It weighs 650 g and can provide 50 W of cooling power. While the louver system is a proven and reliable technology, it is not suitable for small spacecraft due to its weight. The AMDROHP is designed for CubeSats, but the use of liquid cooling further adds to the payload which would decrease the overall efficiency of a TPV system. The examples shown are made from 6061 aluminum. The surfaces are also coated with paints with high emissivity and low solar absorptivity.

There are designs, shown in Figure 3-3, that have been made for deployable cooling system but have not yet been used in actual space projects.

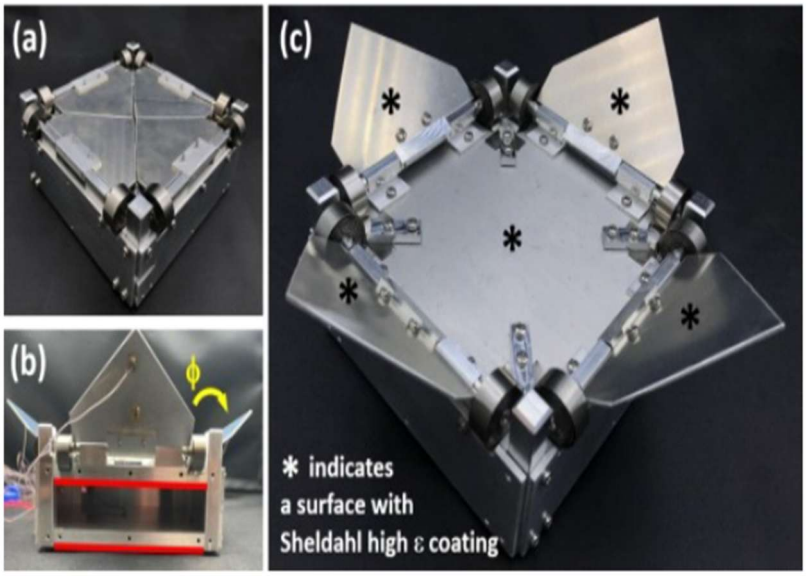

Figure 3-3: Actuator controlled triangular fin array [17]

In Figure 3-3, triangular fins are arranged in a rectangular shape and are deployed using an actuator. 6061 aluminum is also used in this case. This design can control the deployment angle

of the fins in order to reduce the view factor with regards to deep space. This allows for more control over the cooling rate to avoid excessive cooling. The actuator in this case is made using a bimetallic coil which expands as it heats up. The resulting expansion leads to 4 degree angular rotation for every 1 ℃ rise in temperature. [25]

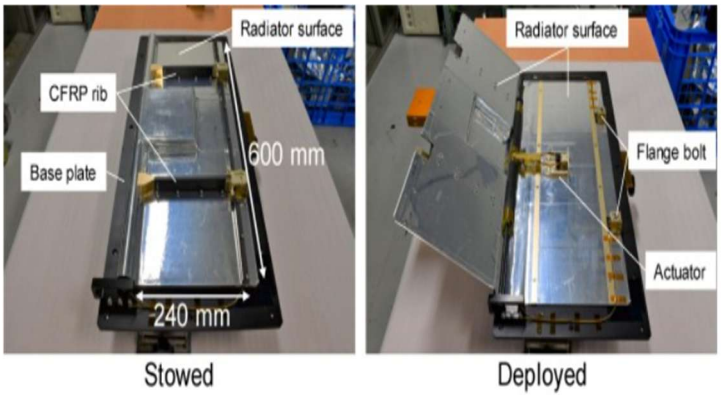

Figure 3-4: Deep-space explorer deployable radiator [18]

Figure 3-4 shows another deployable radiator made with larger panels. The material in this case is graphite sheets with Ag-teflon sheets adhered onto them. A drive crank and torsion bar mechanism is used to open and close the radiator panel. This design is expected to be deployed on Destiny + which will be a deep space exploration technology demonstrator. [26]

One example of a deployable radiative cooler successfully tested in space was aboard the Dellingr CubeSat in 2018. The design is shown in Figure 3-5 below.

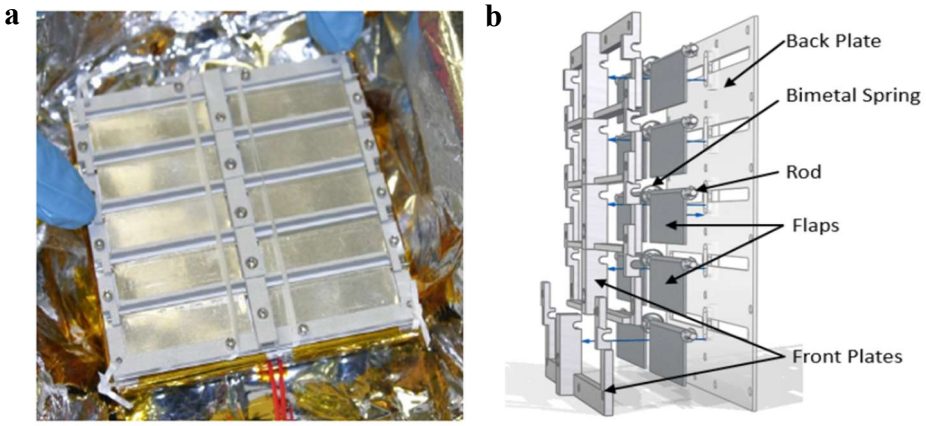

Figure 3-5: (a) Thermal louver top view (b) labeled design [27]

This design allows for control of the cooling rate through a mechanism similar to the triangular fins mentioned above. In this case, a bimetal spring, located as shown in Figure 3-5 (b), acts as an actuator and deploys the aluminum flaps as its temperature changes. This design demonstrated cooling power ranging from 0.5 to 0.9 W. [27]

These designs show interesting features related to this research especially regarding the deployment mechanism. However, they only use one material and the designs with smaller panels have low cooling power. Table 3-1 shows a larger list of radiative cooling structures focusing on smaller designs and providing performance metrics for comparison.

Table 3-1: Properties of designed deployable radiative cooling structures

Deployable Radiative Cooling Structure	Cooling Power (W)	Deployed Area (m²)	Radiative surface thickness (mm)	Cooling power / Area (W/m²)	Reference
Tested in lab					
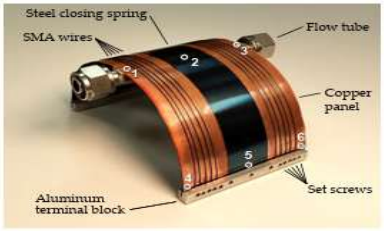 *Figure 3-6: NASA/Texas A&M SMA Morphing Radiator*	10	0.0135	0.178	741	[28]
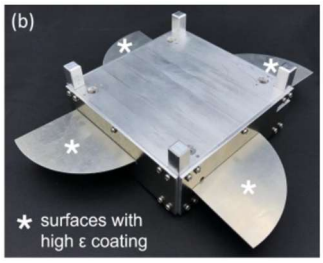 *Figure 3-7: BYU Radial Fin*	30	0.0188	1	1595.74	[29]
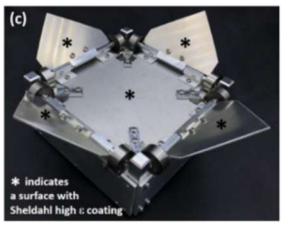 *Figure 3-8: BYU Triangular Fin*	35	0.021	1	1666.67	[25]

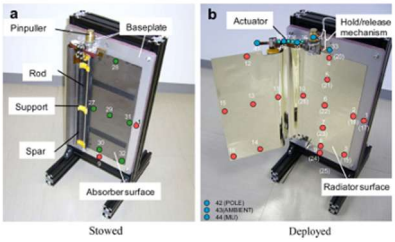 *Figure 3-9: Nagoya University reversible thermal panel*	47.9	0.09	1	532	[30]
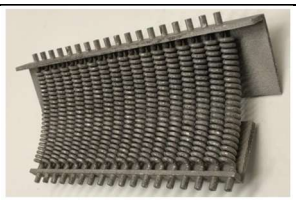 *Figure 3-10: AMDROHP*	50	0.101	2	495.0	[31]
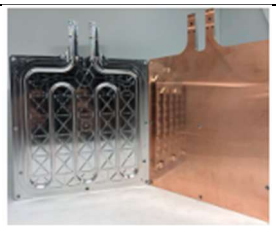 *Figure 3-11: Utah State University Active Thermal Architecture*	60	0.04	6	1500	[32] [33]
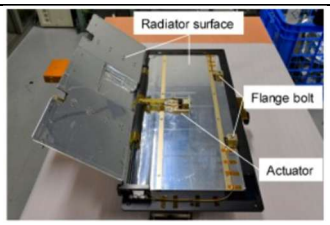 *Figure 3-12: JAXA Re-Deployable Radiator*	100	0.288	1.7	347.2	[26]
 *Figure 3-13: ACT 3D Printed LHP with Deployable Radiator*	250	0.6887	0.8	363.0	[34]

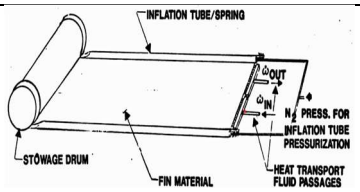 *Figure 3-14: Vought Corp Flexible Radiator*	1330	16.1	0.26	82.6	[35]
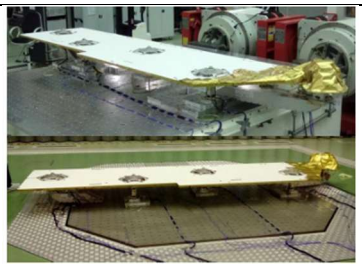 *Figure 3-15: Alphabus Extension deployable panel radiator*	1750	4.62	N/A	378.8	[36]
Manufacturer data					
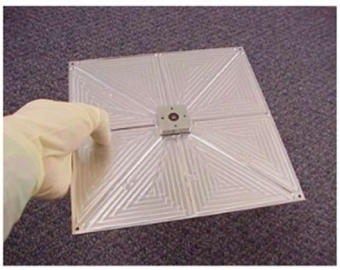 *Figure 3-16: Sierra Space - Miniature Satellite Energy-Regulating Radiator (MiSER)*	12	0.47	1.9	255	[37]
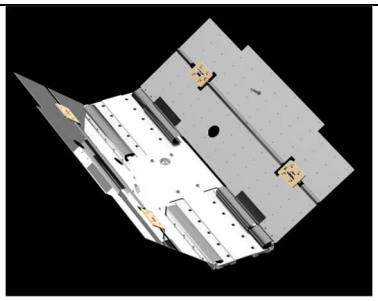 *Figure 3-17: DcubeD (aka FENNEC) Deployable Radiator*	50	0.0299	N/A	1672	[38] [39]
 *Figure 3-18: Sierra Space - Passive thermal louver (20 blades)*	52.9	0.16	N/A	330	[37]

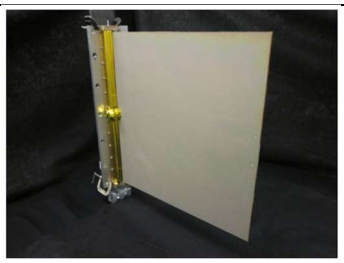 *Figure 3-19: Thermal Management Technologies - Deployable Radiator*	100	0.109	6.3	917	[40] [41]
 *Figure 3-20: Redwire Space Q-Rad*	100	0.04	N/A	2500	[42] [32]
 *Figure 3-21: ThermAvant oscillating heat pipe (OHP) radiator*	215	0.6	3	358	[43]
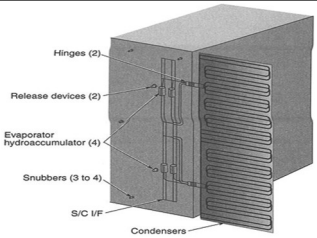 *Figure 3-22: Swales Aerospace - Alpha Deployable Radiator*	1250	4	3.4	312.5	[44]
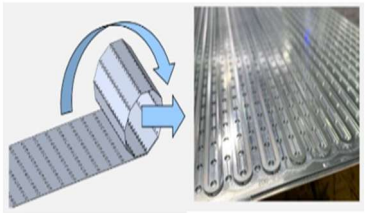 *Figure 3-23: ThermAvant unspooling OHP radiator*	1500	0.34	2.5	4411	[32]

Deployed in space					
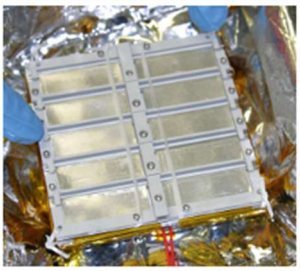 *Figure 3-24: Dellingr CubeSat louver*	0.9	0.06	1	15	[27]
Conceptual / simulated designs					
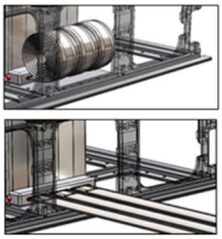 *Figure 3-25: Pumpkin/YSPM Rollout Deployable Radiator*	330	0.56	N/A	589.3	[32] [45]

Table 3-1 shows a large number of different radiative cooler designs. Most of them are passive with the use of purely radiative cooling or the use of oscillating heat pipes (OHP). Coolers compromising OHPs are typically designed with a fixed surface area and hence, do not have as much flexibility in controlling the temperature via view factor changes. A wide range of cooling power and sizes are available for different design types. The radiating surface area in most of these designs can be controlled by the following methods:

1. Louvers

   They are reliable due to their simple mechanism previously shown in Figure 3-1 (b) allowing them to become the most commonly used deployment method. Radiator panels can be easily folded regardless of size and deployed once required.
2. Rollout mechanisms

   This mechanism is used in designs such as Pumpkin/YSPM (Figure 3-25) and Vought Corp rollout radiators (Figure 3-14) but has been rarely used so far. This type of mechanism has been considered since the 1980s but there is little information about its use in real space missions. It involves the use of very thin coiled up radiative panels that can be rolled out along a deployable boom and can provide significant cooling as shown by the 330 and 1330 W of cooling power provided by these two designs. The radiative area can be quite large as it is mainly limited by the length of the boom.
3. Heat sensitive shape memory alloys (SMA)

   The use of SMAs is more modern and an example is the NASA/Texas A&M SMA morphing radiator (Figure 3-6). Materials, such as Nitinol, have the ability to expand or

contract due to its temperature and return to its original shape once it returns to its original temperature. The material is used in the form of strips, wires, or films that are in close contact to the heat source that needs to be cooled. [46] This makes it very attractive for cooling as SMAs can be designed with a specific range of operating temperature. If that temperature is exceeded, the SMAs can expand and lead to the deployment of radiative panels, thereby, increasing the surface area of the radiative cooler. If the SMA returns to its operating temperature, it can contract and retract the panels, thus, reduce cooling and preventing the equipment from getting excessively cooled. This behavior is the reason why it can be named a morphing radiator. The downside of these designs is the fact that SMAs can exert a relatively small force. Hence, they are only suitable for small lightweight radiative coolers used on CubeSats. Additionally, the material can only contract and expand over a limited number of cycles due to fatigue making it potentially unsuitable for longer term missions.

4. Bi-metal coils or springs

   The use of bi-metal springs was shown on the Dellingr deployable radiator (Figure 3-24) but bi-metal coils can also be used in design such as the two BYU radiative coolers (Figure 3-7 and Figure 3-8) with the same principle applied. It involves two thin metals with distinct thermal expansion coefficients. As one of the metals expands more than the other when it is heated, it causes torsional movement in the coil or spring. The longer the coil, the greater the amount of movement caused. Conversely, as the metals cool down, the same metal contracts faster that the other leading to movement in the opposite direction. This type of phenomena has been used for several decades in appliances such as thermostats and toasters. In space, it provides similar advantages to SMAs where it can be designed for specific temperature ranges but also has the disadvantage of being limited to small lightweight radiators and affected by material fatigue over a large number of cycles.

5. Adjusting the angles of the radiating panels

   This type of mechanism is shown in the JAXA re-deployable radiator (Figure 3-12). It is very simple with the panels attached with hinges and deployed using an actuator. The angle of the panels can be controlled by only partially folding the panels, thus, reducing the view factor of the panels related to deep space or the incoming radiating rays. This allow more intricate cooling depending on the position of the spacecraft or cooling requirements that are changing depending on which equipment is in operation.

Another important factor to consider in these designs is their weight. Mechanisms that require actuators, motors, or liquids are heavier than bi-metal and SMA designs. As discussed in section 1.1, heavier payloads lead to higher costs. The designs shown in Table 3-1 have various weights due to the diverse designs. A comparison between the cooling power and weight of some of these designs is shown in Figure 3-26.

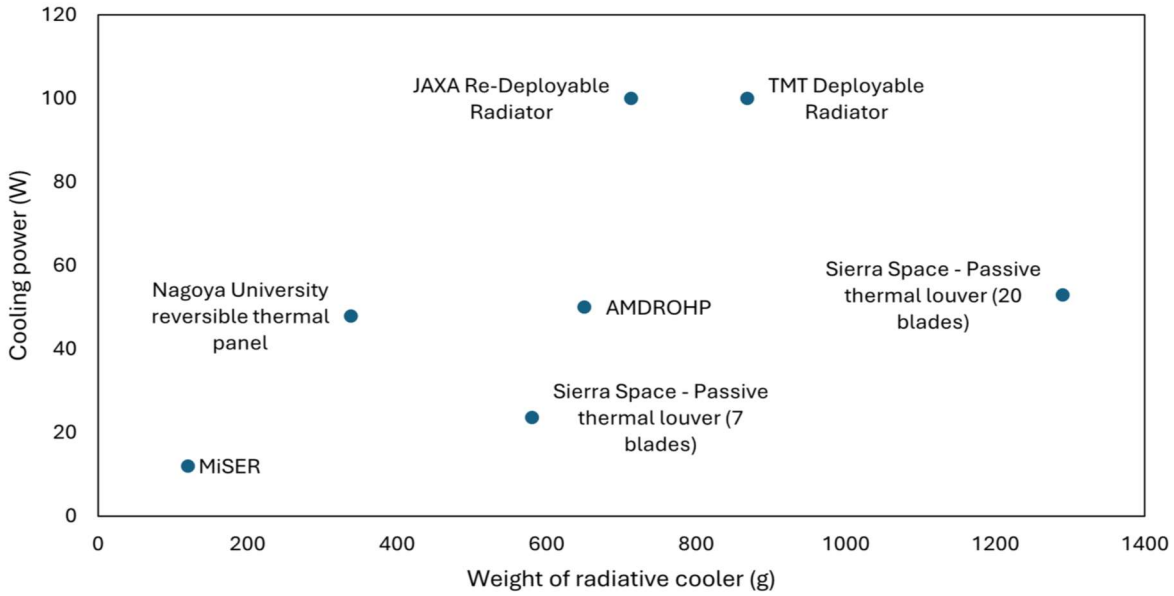

Figure 3-26: Comparison of cooling power and weight for multiple radiative cooling structure designs [31] [26] [30] [41] [30] [37]

The weights in Figure 3-26 were taken from literature and are focused on the radiative coolers along with their mechanism. Baseplates and other supports are excluded where possible to allow a greater focus on their deployable radiative cooling capabilities. Several designs from Table 3-1 lacked information regarding weight and were not considered. The Nagoya University reversible thermal panel (Figure 3-9) performs the best for cooling structures that provide cooling powers of 50 W and under as it provides the highest amount of cooling at a relatively low weight. The Sierra Space passive thermal louver (Figure 3-18) is commercially available for multiple different designs. The 7-blades and 20-blades designs are compared, and it can be observed that their cooling power/weight ratios are both around 0.04 W/g. The number of blades in this design can be changed to fit cooling demands. The JAXA re-deployable radiator (Figure 3-12) provides the best cooling power/weight ratio in the higher cooling power structures. This metric is influenced by the materials used for each cooler, and this will be further discussed in the next section.

3.2 Suitable materials

Materials used in radiative coolers are key to optimize cooling while minimizing weight. However, there are few materials suitable for use in outer space due to the presence of a vacuum. NASA developed an industry accepted standard for material testing and acceptable criteria outlined in ASTM E595-15. The materials need to be tested for a day at 125 °C in a vacuum with a maximum pressure level of 5×10^{-5} torr. During that time, trapped gases within the material structure will be released causing mass loss and the release of volatile substances in the vacuum chamber. The Total Mass Loss (TML) and Collected Volatile Condensable Materials (CVCM) are measured after the 24 hours are completed. A suitable material needs to have a TML of 1 % or less along with a CVCM of 0.1 % or less to be deemed suitable. These numbers imply that a small

amount of outgassing is acceptable, however, if equipment sensitive to these depositions are involved, stricter standards or other tests need to be carried out. [47]

Materials in space may also face degradation due to exposure to ultraviolet rays, ionizing radiators, and atomic oxygen in low-Earth orbit missions. These can heavily affect polymers leading to early degradation and potential structure weaknesses. Degradation has been previously observed in FEP-Teflon, a material used in the Vought Corp flexible radiator (Figure 3-14) design. [48]

An analysis was conducted on the materials used in Table 3-1. The materials used were counted based on their presence in the cooling structures and the results are shown in Figure 3-27 below.

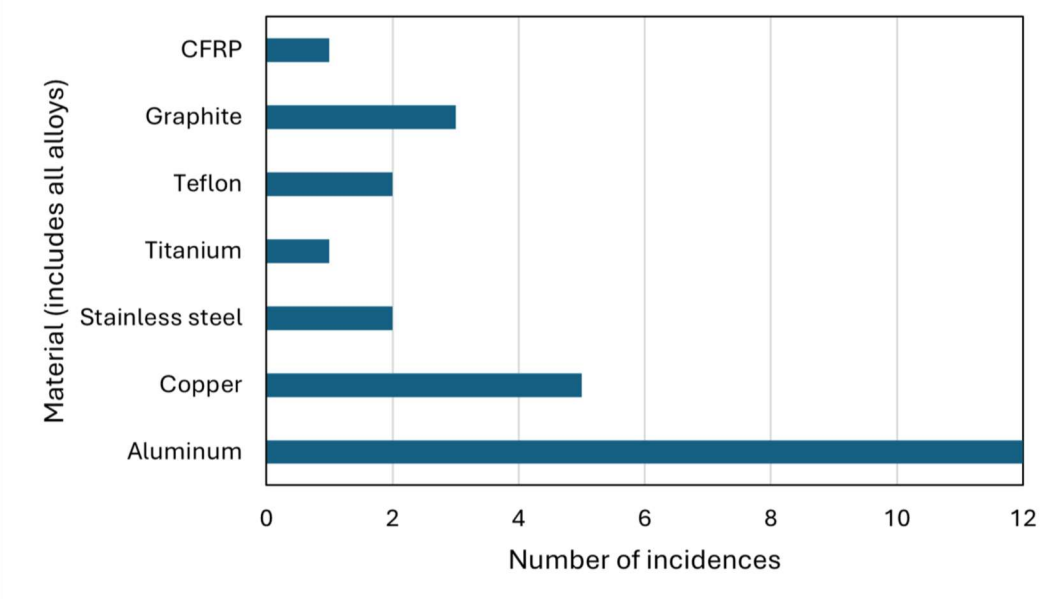

Figure 3-27: Number of incidences by material in radiative coolers

All alloys were considered for each material. For example, 6061-Aluminum, 7075-Aluminum, and 1050- Aluminum were all counted as part of aluminum is Figure 3-27 above. This was done since a lot of structures did not specify the alloy used, however, among those listed, 6061-Aluminum was the most commonly used of all materials. Aluminum, copper, and graphite were the three most commonly used materials. Teflon was used in some designs but as mentioned some Teflon composites degrade in space. Stainless steel and titanium were mainly used for structural purposes and had little to do with cooling. Carbon fibre reinforced polymer (CFRP) was also used but carbon fibre composites can have wide ranges of thermal conductivity. Since the goal of this research is to maximize cooling while reducing weight, a comparison of density and thermal conductivity can provide valuable information. This comparison was performed and is displayed in Figure 3-28.

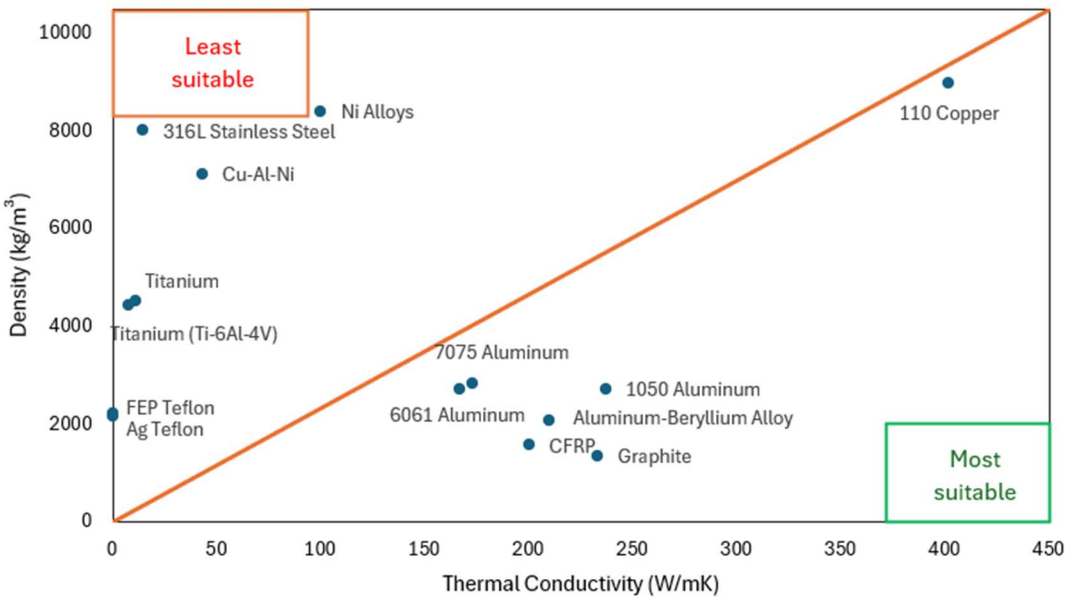

Figure 3-28: Comparison of density and thermal conductivity of materials

The most suitable materials have the highest conductivity while having the lowest density as shown in the bottom right of Figure 3-28 with the top left being the opposite. It can be observed that there is no material in the ideal region. Materials with high conductivity, like copper, has high density while aluminum alloys, graphite and carbon-fibre are lightweight with lower conductivity compared to copper. The high number of incidences for aluminum observed in Figure 3-27 indicates that lowering weight is typically more favored over higher thermal conductivity. However, this varies by design. A multi-material cooler could potentially fill this gap between aluminum alloys and copper with a design solution consisting of an effective thermal conductivity higher than aluminum and an effective density lower than copper.

Among the designs outlined in Table 3-1, there were also other composites made of carbon-fibre and graphite used with higher thermal conductivity. Figure 3-29 shows a few carbon fibre composites used in space.

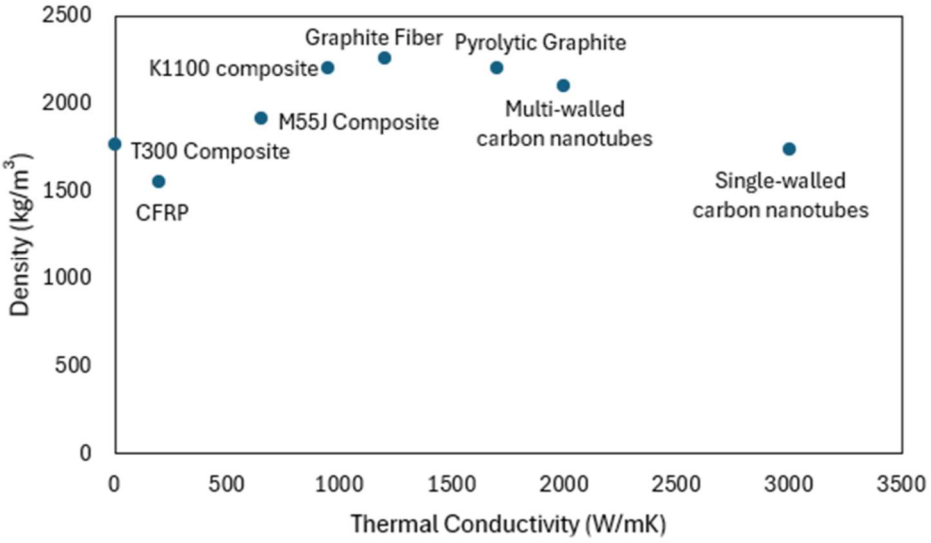

Figure 3-29: Carbon fibre composites density vs thermal conductivity

It can be observed that the materials in Figure 3-29 reach very high thermal conductivities while having low density. They are within the ideal region to be used for a radiative cooler and are better than copper while having strong tensile strength. However, when exposed to a space environment, carbon nanotubes, for example, have shown to be damaged by ultra-violet rays, ionic radiation, and atomic oxygen resulting in 40-65 % reductions in tensile strength. [49] The Nagoya university reversible thermal panel (Figure 3-9) used pyrolytic graphite as part of its design resulting in good performance but due to the frailty of the 10 μm thick sheets, they had to be woven with copper fabric. It was used primarily to enhance heat absorption and transfer of heat across the structure. [30] CFRP is the most commonly used amongst these materials and its thermal performance is more comparable to aluminum alloys as shown in Figure 3-28. More research needs to be done for the use of some of the higher conductivity materials, but they can however be used as interior thermal interface material to transfer heat more effectively. More details about these types of materials are discussed in the next section.

3.3 Novel materials

There are currently novel materials being researched that can be used in the future to improve cooling performance in space but are currently at low technological readiness levels. Some examples are as follows:

1. Tunable emissivity

   These materials have the particular characteristics of being able to adjust their emissivity or absorptivity based on temperature. One example is the use of Vanadium dioxide (VO_2) which undergoes a change in its optical properties at 68 ℃. Typically, the emissivity of VO_2 gets reduced at high temperatures, however, combining the materials with others such as BaF_2 creates a suitable option for space cooling that shows great potential. [50] Further research is also being done on tunable emissivity through the use of

Near-Field Radiation Assisted (NFRA) smart skin which controls emittance via changes in voltage [51] and on multifunctional nanostructures with controllable band-gaps which control emission via optical gap control. [52]

2. Advanced phase change materials

   Phase Change Materials (PCMs) can store heat by for example changing from a solid to a liquid. This allow a large amount of heat energy to be stored and can help in space cooling. Use of materials such as paraffin are being investigated for thermal control and mechanical actuation. [53]

3. Adaptive metamaterials

   Adaptive metamaterials include SMA with some examples shown in Figure 3-6 where radiators can morph their shape to increase or decrease the surface area based on temperature. They are able to return to their original shape after undergoing thermally induced deformation. This enables thermal control by controlling radiative emissions.

These aforementioned novel materials offer a lot of promise for future thermal control designs. More research and testing is required before they can be used in real world projects.

3.4 Thermal interfaces

Thermal interface materials enhance heat transfer between surfaces in contact with each other. They are placed in between heat-generating components and cooling systems to maximize thermal transfer efficiency. In space, there are restrictions regarding the suitability of materials due to contamination risks and outgassing concerns. For instance, silicon-based greases were commonly used in early space missions but were found to be a cause of contamination. [54] Some examples of thermal interfaces are as follows:

1. Loop heat pipes and heat pipes

   Examples of this type of thermal interfaces were listed in Table 3-1 in designs such as the 3D printed loop heat pipe design illustrated in Figure 3-13. Heat pipes allow the transfer of heat via phase change fluids that carry heat away from heat sources and towards radiators for heat rejection.

2. Thermal straps

   These are typically made of copper or aluminum and can be flexible. Heat travels via the highly thermally conductive material from one material to another. An example from Thermal Management Technologies is shown in Figure 3-30 below.



Figure 3-30: Thermal strap [55]

As shown above in Figure 3-30, it is a very simple design that can be flexible or rigid depending on circumstances. Straps can take various shapes and be made from braids, films or sheets. Pyrolytic graphite can also be used as a material. [56]

3. Thermally conductive materials

   The use of thin highly conductive materials sandwiched between two surfaces is a simple way of enhancing heat transfer through the lowering of thermal contact resistances.

4. Bolted-joint conductance

   In section 2.1, the impact of pressure on thermal conductance was discussed. Using the same principle, bolts under various torques can be used to increase the pressure between two materials, hence, enhancing conductance. [56]

5. Thermal pads

   A thermal pad is made of a highly thermally conductive material that can be place between a heat source and a cooler as shown in Figure 3-31.

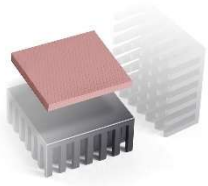

Figure 3-31: Parker Chomerics THERM-A-GAP 579 thermal pad [57]

These pads can be of various thickness and can provide electrical insulation as well.

6. Thermal switches

A thermal switch can be seen in the MiSER design (Figure 3-16). It is a small square shaped switch in the middle of the design meant to control heat transfer from the heat load to the radiative cooler. It is designed for a set point temperature and when this is surpassed, the conductance of the switch increases, thus allowing more heat transfer to occur. [37]

7. Phase change materials

   These materials can conduct heat away from a heat source while also acting as a thermal storage unit via solid to liquid phase changes. They are useful in designs involving thermal cycling. [37]

The examples above show various ways of transferring heat from one surface to another. Their suitability depends on the design problem being solved and their specific constraints. The materials used, and the thermal interfaces in radiative cooling structures have been discussed, however, there has been more of a focus on thermal conductivity and not on the emissivity of the heat rejection surfaces. This is determined by the coatings used in space and discussed in the next section.

3.5 Thermal control coatings

As shown in the Stefan-Boltzmann equation, radiation is a function of emissivity. Additionally, in a space environment, the cooler is exposed to radiation coming from the sun, the Earth, and reflected rays. Hence, the outer surface properties of a cooler is a key factor for thermal control. If the goal is to cool a structure as much as possible, the outer surface needs to have low solar absorptivity to reflect as many incoming rays as possible while having high thermal emissivity to maximize radiative heat transfer. Coatings, such as AZ-400 shown in Section 2.5, are applied on the outer surface to achieve this goal. Table 3-2 shows a list of coatings used in space found from literature and manufacturer data.

Table 3-2: Properties of coatings used in space

Coating	Type	Solar Absorptivity	Thermal Emissivity	Source
Aeroglaze 276 White Gloss	White	0.17	0.88	[58]
AZW/LA-II	White	0.09	0.91	[59]
AZ-83	White	0.17	0.85	[60]
AZ-93	White	0.15	0.91	[60]
AZJ-4020	White	0.15	0.88	[61]
AZ-400	White	0.15	0.89	[61]
Chemglaze A276	White	0.26	0.88	[62]
EKOM-1 (white)	White	0.302	0.88	[58]
GSFC White Paint NS43C	White	0.2	0.92	[63]
Magnesium Oxide	White	0.09	0.9	[59]
White Silicone Paint PCBE	White	0.27	0.88	[58]
White Silicate Paint PSBN	White	0.15	0.92	[58]
White Silicone Paint SG121FD	White	0.2	0.88	[58]
YB71	White	0.18	0.9	[62]
Zinc Orthotitanate with Potassium Silicate	White	0.13	0.92	[62]
Zinc Oxide with Sodium Silicate	White	0.15	0.88	[62]
AZ-2000-IECW	Conductive	0.25	0.88	[61]
AZJ-3700	Conductive	0.2	0.87	[60]
AZ-1000-ECB	Conductive	0.97	0.89	[61]
GSFC NS43G	Conductive	0.26	0.9	[62]
MLS-85-SB-C	Conductive	0.98	0.91	[61]
Z93SC55	Conductive	0.14	0.94	[62]
EKOM-2 (black)	Black	0.95	0.87	[58]
Anodize black	Black	0.88	0.88	[62]
Black Silicone Paint PN	Black	0.95	0.9	[58]
RM-550-IB	Black	0.97	0.91	[61]
TMJ-20-LSB	Black	0.96	0.91	[61]
Z302 Black, Gloss	Black	0.962	0.83	[58]
Z306 Black, flat	Black	0.97	0.91	[58]
AMJ-400-IG	Green	0.56	0.9	[61]
AMJ-600-IR	Red	0.45	0.91	[61]
AMJ-700-IBU	Blue	0.75	0.88	[61]
TMS-800-IY	Yellow	0.36	0.89	[61]
AMJ-450-LSG	Green	0.56	0.85	[61]

It can be immediately observed from Table 3-2 that there are multiple types of coatings that are used with various thermal-optical properties. This is to allow more flexibility in the thermal

control design as excessive cooling can be harmful to electronics and coatings The four types listed in Table 3-2 above are:

1. White paint

   This is the most used paint with solar absorptivity values ranging from 0.09 to 0.3 and thermal emissivity values between 0.88 and 0.92. It maximizes radiative cooling while minimizing absorption of incoming rays, hence, providing maximum cooling.

2. Black paint

   Black paint has similar thermal emissivity values as white paint, however, its solar absorptivity values are much higher between 0.88 to 0.97. Depending on the design of a spacecraft or satellite, it can be beneficial to absorb more incoming rays and heat up some areas within the structure to avoid excessive cooling. Additionally, black paint is also used to reduce visibility in the night sky as bright structures would stand out and affect astronomers conducting planetary observations.

3. Conductive paint

   This type of paint can be of any color, and it is specifically designed to be electrically conductive. It was designed following observation of surface charging in missions carried out between the 1970s and early 1990s. This charge build up stemmed from the spacecraft interactions with the components inside it, ions from space plasma, and charged particles causing damage to electronic equipment inside them. [64] These conductive paints were developed to properly conduct and discharge these charged particles to protect areas where they could cause damage.

4. Colored paint

   The other colored paints are mostly used for logos but due their wide range of thermal emissivity values they can be used strategically to control the temperature in some areas of a spacecraft or satellite.

There exist a large number of different coatings used in missions by various countries but they mostly fall within the same range of thermal emissivity and solar absorptivity based on the types of paint. Figure 3-32 shows some more coatings and polished metals. Smart radiation devices (SRD) are made from novel materials with variable emissivity for space use. They can be made in the form of single sheet ceramic tiles or with multilayer films (SRDM). [65]

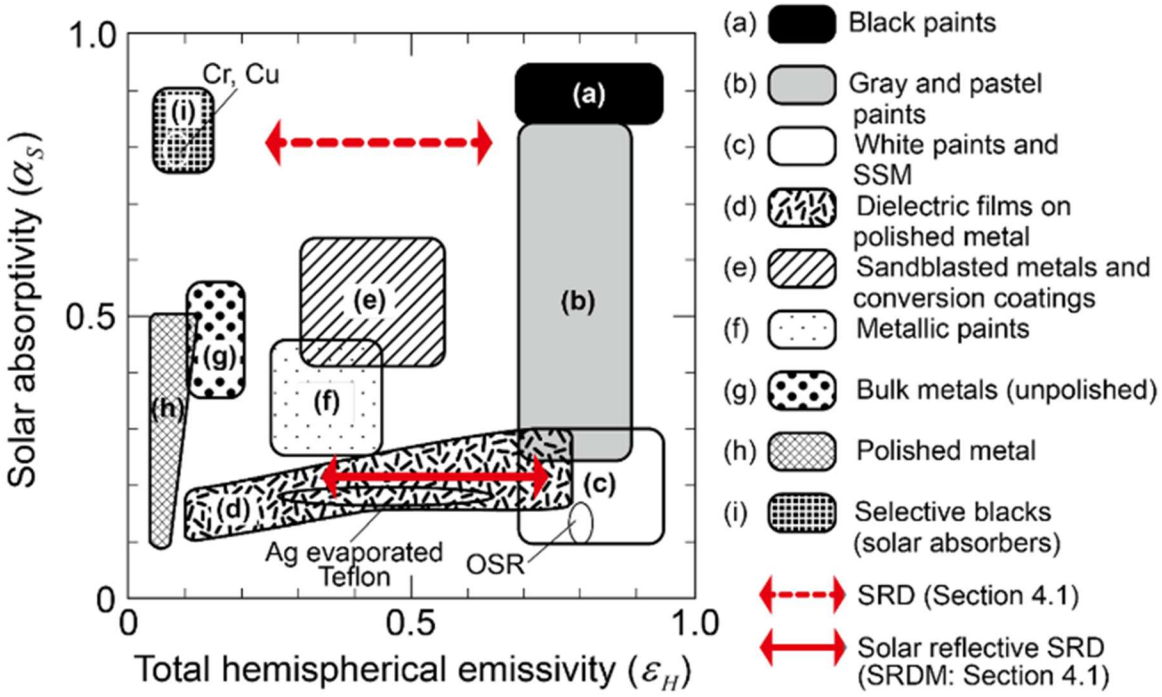

Figure 3-32: Solar absorptivity and total hemispherical emissivity values for various paints and films used for conventional thermal control and smart radiation devices (SRD) [65] [66]

Figure 3-32 above shows the similar range for white paint and black paint as compared to Table 3-2. Polished metals show the lowest emissivity values along with low solar absorptivity values. There is a variety of thermal optical properties that can be used for different designs depending on their goals. For this research, white paint will be the one considered as the main goal is to maximize cooling.

3.6 Thermal vacuum chambers

One of the objectives of this research involves the design of a practical experiment to validate the numerical results generated using COMSOL and to evaluate their level of accuracy. The experiment will be carried out in a vacuum chamber to replicate space environment with a goal of testing a radiative cooler and determining its radiative cooling power. This section looks at the key elements required to design an experimental setup. Figure 3-33 shows three thermal vacuum chambers used for testing by the National Aeronautics and Space Administration (NASA) and European Space Agency (ESA).

c

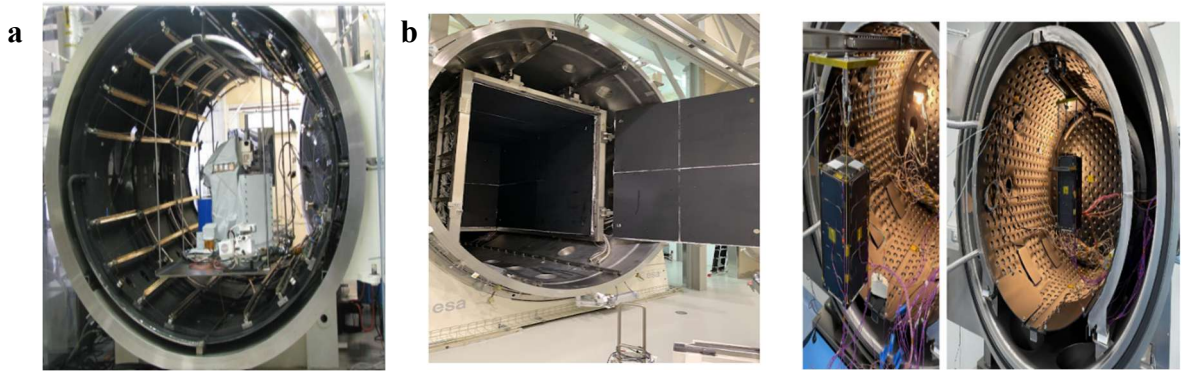

Figure 3-33: Large-scale thermal vacuum chambers (a) NASA [67] (b) Phenix facility [68] (c) EASA CubeSat support facility [69]

Based on these thermal vacuum chamber designs, the main components can be divided as follows:

- Vacuum chamber

  Chambers are typically made of stainless steel that can be cooled or heated depending on the test being performed. For this project, the chamber walls would need to be cooled which is achieved using thermal shrouds that are in contact with cooling lines filled with cryogens such as liquid nitrogen. This allows the temperature of the walls to drop as low as -150 °C. [67]
- Vacuum chamber walls

  The walls shown in Figure 3-33 are painted black in order to replicate deep space. Since all radiation emitted in space travel away from the emission source, the walls need to replicate the same environment by minimizing the amount of radiation reflected back onto the test object. Hence, a black colored wall with high absorptivity is required.
- Lamps

  Quartz IR lamps are installed in these chambers to represent the impact of solar radiation. The lamps are separated into different zones and can produce up to 5000 W of heat output per zone. [67] This allows different testing at different solar view factors based on the angle at which the test object is expected to face the sun.
- Thermally-controlled platen

  The platen is the platform where the test object is placed. Its temperature can be controlled depending on the test being conducted. [70]

4 Method

4.1 Preliminary modeling

The initial phase of this research consisted of confirming the viability of radiative cooling as a cooling method for a TPV cell. The feasibility of this method was assessed via finite element simulations on COMSOL.

4.1.1 Feasibility analysis

The TPV setup considered for this research is based on a research paper titled "Ellipsoidal Optical Cavities for Enhanced Thermophotovoltaics". [3] Simulations in this paper determined a 40 W cooling power requirement for the TPV setup. A simple calculation, determining the required surface area for this cooling power, can assess the suitability of radiative cooling. The Stefan-Boltzmann equation can be rearranged as follows:

$$A = \frac{q_{rad}}{\sigma\varepsilon(T_S^4 - T_{surr}^4)} \qquad \text{Equation 16}$$

In an ideal case, the radiative cooler was assumed to have a uniform temperature, rejecting all absorbed heat from the cell into space. The cell would be placed in contact with the center of the radiative cooler as the heat source. The temperature of the structure is considered to be 300 K as this is the recommended operating temperature of TPV cells and the temperature of surroundings is considered to be 3 K to represent deep space. The emissivity is assumed to be 0.91 similar to the total hemispherical emissivity of AZ-93 paint. This resulted in a reasonable required surface area of 0.0957 m^2, thus, indicating that a purely radiative cooler of a manageable size is feasible.

However, it is to be noted that in practice the temperature across the surface will vary based on the distance from the cell which is the heat source. The Stefan-Boltzmann equation assumes the surface temperature is uniform with the heat spread out evenly across the surface. In practice, the temperature at the center of a radiative cooler would be higher than the average surface temperature and the outer edges of a cooler would be lower than average. Additionally, the TPV cell would be inside of a satellite and at a temperature much higher than 3 K with surrounding temperatures around 298 K instead. A COMSOL simulation was performed to account for these variations and model the temperature gradient across the radiative cooler's surface. The heat transfer and surface-to-surface radiation modules were used. The model used is shown in Figure 4-1 below.

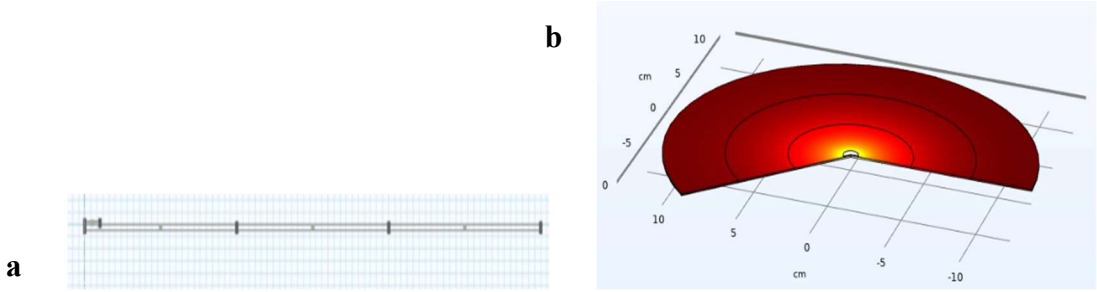

Figure 4-1: (a) 2D revolution geometry (b) Resulting model

A 2D revolution model of a disc shaped radiative cooler was used on COMSOL for faster computation. The radius resulting in a radiating area of 0.0957 m^2 after taking into account the cell area was found to be 12.3 cm as used in Figure 4-1 (a). The radiative cooler was made of copper and has a thickness of 1 mm. Table 4-1 shows the simulation parameters used.

Table 4-1: COMSOL parameters for feasibility analysis

Module	Parameter	Value [units]
Material	Copper – thermal conductivity	400 [W/mK]
	GaSb – thermal conductivity	320 [W/mK]
Heat transfer	Ambient temperature	3 [K]
	Heat flux	40 W
Surface-to-surface radiation	Emissivity: TPV cell	0.5
	Emissivity: panels	0.87
	Ambient temperature (cell)	298 [K]
	Ambient temperature (panels)	3 [K]
Mesh	Maximum element size	0.1 [cm]
	Minimum element size	$1 * 10^{-4}$ [cm]
	Maximum element growth rate	1.3
	Curvature factor	0.2
	Resolution of narrow regions	1

As shown in Table 4-1, for the boundary conditions, an ambient temperature of 3 K, a heat flux of 40 W, and an emissivity value of 0.91 for the surface of the radiative cooler is used. The term “ambient temperature” represents the temperature of the surroundings where heat is being rejected through radiation. A disk-shape heat element, approximating a GaSb TPV cell, was added to represent the heat source with a radius of 0.5 cm and thickness of 0.5 mm. The ambient temperature around the cell was considered to be 298 K as in practice, the interior of a small satellite or CubeSat is heated to avoid component damage related to excessively low temperatures. The simulation used a mesh with a minimum element size of 1×10^{-4} cm and maximum element size of 0.01 cm. Only radiation and conduction were considered as heat transfer mechanisms. A complete vacuum was assumed with no convection taking place. A close up of the mesh around the cell is shown in Figure 4-2.

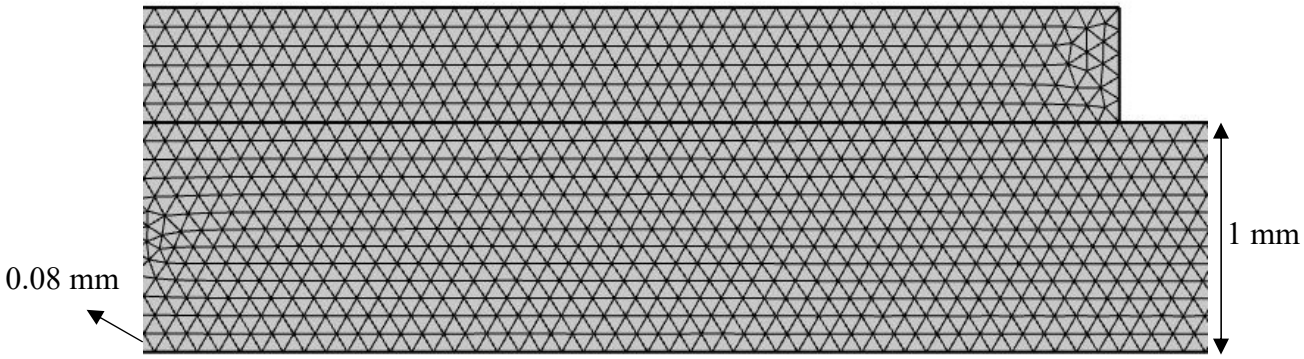

Figure 4-2: Mesh close-up

Figure 4-2 shows that the mesh divided the structure into adequately small pieces for analysis. The gradient across the surface of the cooler was plotted by using a straight line from the center to the outer edge and shown in the results section. The radius of the radiative cooler was further increased to obtain a temperature of 298 K at its center which represents the operating temperature of the TPV cell. The temperature gradient across multiple radii was also obtained.

The heat transfer process can be represented by a thermal circuit diagram as shown in Figure 4-3 below.

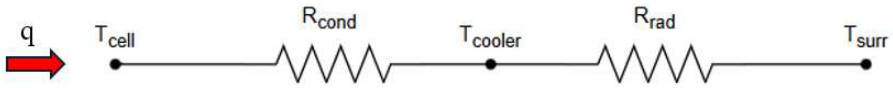

Figure 4-3: Thermal circuit diagram

In Figure 4-3, T_{cell} is the temperature of the TPV cell, T_{cooler} is the temperature of the radiative cooler, T_{surr} is the temperature of the surroundings, in this case, deep space, R_{cond} is the thermal resistance for conduction and R_{rad} is the thermal resistance for radiative heat transfer.

4.1.2 Model verification

A finite element software performs calculations based on inbuilt mathematical equations and models. In order to ensure that the math is being handled properly, it is important to conduct a verification process before proceeding. The results obtained for the feasibility analysis can be easily verified through the Stefan-Boltzmann equation. At steady-state, the amount of power applied to the cooling structure is the same as the amount of power radiated away from the cooler. Radiation coming from other spatial bodies was not considered here as it was not part of the feasibility analysis due its relatively low significance. The following equation can, hence, be used to calculate the cell temperature, T_{cell}.

$$T_{cell} = \sqrt[4]{\frac{P_{in}}{A\sigma\varepsilon} + T_{surr}^4} \qquad \text{Equation 17}$$

P_{in} represents the input power of 40 W, A is the radiating area of 0.0957 m^2, T_{surr} is the temperature around the cell surroundings (298 K), σ is the Boltzmann constant value of 5.67 x 10^{-8} $W/m^2 \cdot K^2$ and ε is the emissivity value of 0.91. Based on these values, a cell temperature of 355 K was obtained. That value was the same as the temperature obtained when considering the surrounding temperature where the cell would be located in practice as well as temperature gradients.

4.1.3 Impact of size changes

This section studies the impact of size changes on cell temperature regarding thickness and for fixed volume cases. The simulation carried out in Section 4.1.1 used a uniform thickness of 1 mm and the radius of the structure was increased to vary the temperature. To gain a better understanding of the impact of different thicknesses, a parametric sweep was conducted using the same boundary conditions shown in Table 4-1 wherein thicknesses over the range from 0.1 mm to 2 mm were simulated in 0.1 mm increments. Moreover, simulations were carried out for fixed volume cases using the same boundary conditions to compare the impact of geometry changes for an unchanged volume of material. A cooler made of copper with a diameter of 30 cm and a thickness of 1 mm was used as a base case for the volume size. A constant volume value, V_c, of 70.7 cm^3 was calculated. A parametric sweep was conducted with the radius varied and the thickness value found according to Equation 18.

$$t = \frac{V_c}{\pi r^2} \qquad \text{Equation 18}$$

Some of the resulting coolers are illustrated in Figure 4-4 with three different radii shown.

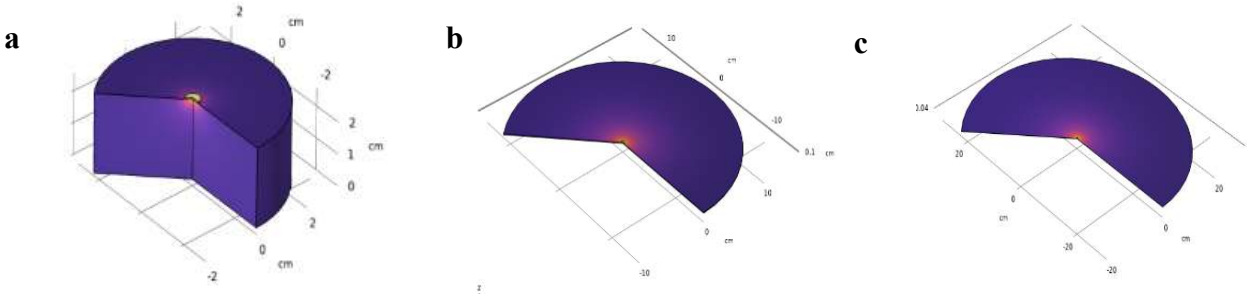

Figure 4-4: Fixed volume cases (a) 3 cm radius (b) 15 cm radius (c) 30 cm radius

As shown in Figure 4-4, the cooler gets thinner as its radius increases ensuring a constant volume and, hence, weight. Radii in the range of 3 cm to 30 cm were considered using 3 cm intervals resulting in 10 different cases. The temperatures at the center of the cooler, which is assumed to be same as the TPV cell, and at the outer edge of the cooler were recorded at steady-state and plotted for further analysis.

4.1.4 Impact of materials

The thermal conductivity of a material plays an important role in cooling as it determines the effectiveness of heat transfer through conduction. The heat present at the cell needs to be transferred to the cooling structure as fast as possible. While this does depend on the conductance, the temperature gradient is also important. A larger temperature gradient increases the amount of heat transferred through conduction. Hence, the temperature at the center of the cooling structure needs to be as low as possible to enable the heat from the cell to be transferred as fast as possible. Additionally, the thermal contact conductance between the materials, namely from the cell to the radiative cooler and across the material intersections within the cooler, needs to be as high as possible. An effective radiative cooler would have a large temperature gradient between the heat source and itself at the point of contact since the heat would be transferred away from the center towards its edges. The impact of using different materials is compared using the same model as above with a fixed thickness of 1 mm.

4.1.5 Panel configurations

A deployable structure can be made from multiple materials taking advantage of the fact that the heat flux decreases as the distance from the center of the radiative cooler increases. Figure 4-5 shows an example of a configuration consisting of 3 squares with uniform thickness.

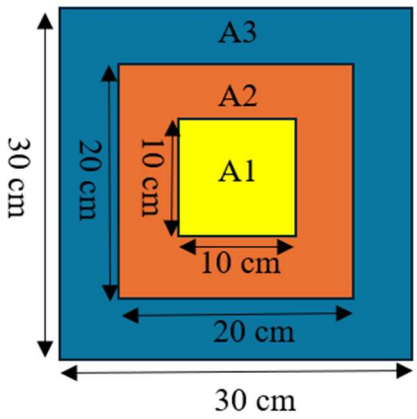

Figure 4-5: Example of a panel configuration

Figure 4-5 shows three different areas for each square representing the area available for radiative heat transfer. In this example, A1 is 100 cm^2, A2 is 300 cm^2, and A3 is 500 cm^2. Only one side facing a low temperature surrounding is considered. In a configuration where a TPV cell is cooled by placing it at the middle of A1, the area available for heat rejection through radiative cooling increases with increasing distance from the TPV cell at the center of the cooling panel. The heat flux from the TPV cell to the panel is concentrated in the middle of the cooler at the TPV cell location and is dissipated across the cooler before being radiated away to the surroundings. A more conductive material would allow the heat to be transferred away from the cell quicker. As the heat flux gets dissipated across the cooler further away from the cell, a larger area is available

to absorb that heat and radiate it away leading to a decreasing temperature gradient from the center to the edges. The lower temperature gradients closer to the edge of the radiative cooler imply there is a lesser need for highly conductive material at these regions. It follows that other criteria, such as density, may dominate material selection at the outer regions of the radiative cooler since the requirements for high thermal conductivity are less stringent. In this regard, a multi-material configuration can enable weight reduction of the structure and hence, the payload cost during the launch of a small satellite or CubeSat. Varying the materials used across a radiative cooler can have distinct benefits. In order to maximize cooling, the positioning of the materials relative to the heat source needs to be investigated. The initial hypothesis suggests that placing the material with the highest thermal conductivity at the center, followed by materials with progressively lower density and thermal conductivity further out, would be the best option assuming constant emissivity. This would potentially allow the heat flux to be dissipated using an effective and lightweight radiative cooler.

Three materials were chosen to numerically simulate the performance of the multi-material radiative cooler, namely, carbon fibre composite (C), aluminum (Al), and copper (Cu). Figure 4-6 (a) shows the configuration used for the simulations.

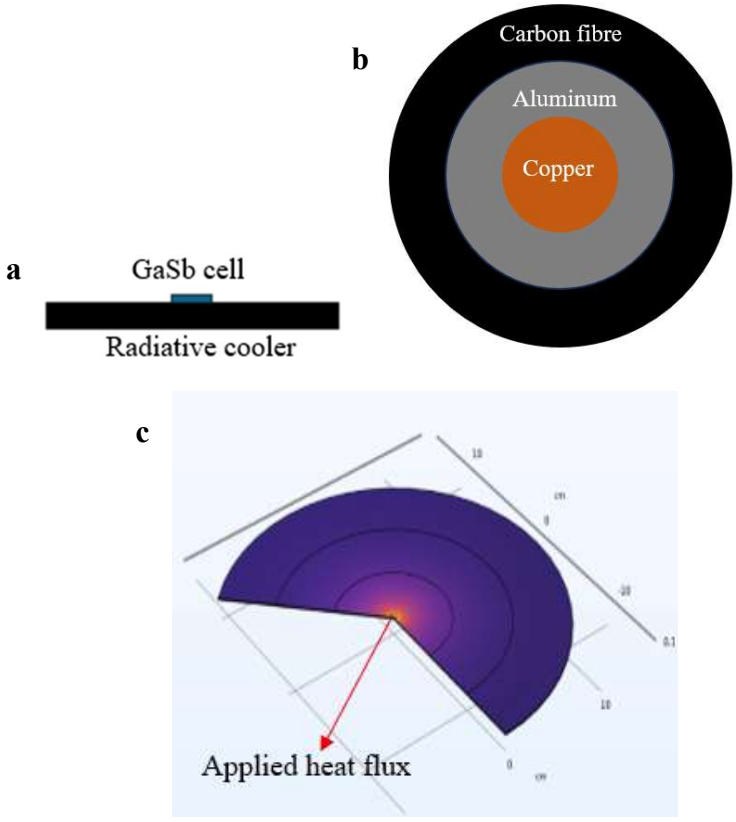

Figure 4-6: (a) Cross-section (b) Model layout from top view (c) COMSOL model with location of applied heat flux shown

These three materials were chosen due to their distinct thermal conductivity and their prevalence in space use. A 2D revolution simulation was carried for faster computation with a material sweep applied in three circular sections to vary the order of the three materials. A total of nine combinations were used as shown in Table 4-2.

Table 4-2: List of material combinations for disk-shaped cooler simulations

 Cu-Cu-Cu	 Al-Al-Al	 C-C-C
 Cu-Al-C	 Al-Cu-C	 C-Cu-Al
 Cu-C-Al	 Al-C-Cu	 C-Al-Cu

The combinations shown in Table 4-2 start from the middle (left-side area) to the outer edges (right side area) of the cooler. Table 4-3 shows the parameters used on COMSOL.

Table 4-3: COMSOL parameters used for panel configuration cases

Module	**Parameter**	**Value [units]**
Material	Copper – thermal conductivity	400 [W/mK]
	Aluminum – thermal conductivity	238 [W/mK]
	Carbon fibre - thermal conductivity	200 [W/mK]
	GaSb – thermal conductivity	320 [W/mK]
Heat transfer	Initial temperature	298 [K]
	Heat flux	40 W
Surface-to-surface radiation	Emissivity: TPV cell	0.5
	Emissivity: panels	0.91
	Ambient temperature: TPV cell	298 [K]
	Ambient temperature: panels	3 [K]
Mesh	Maximum element size	0.008 [cm]
	Minimum element size	$1 * 10^{-5}$ [cm]
	Maximum element growth rate	1.1
	Curvature factor	0.2
	Resolution of narrow regions	1

Table 4-3 shows that a heat flux of 40 W was applied. Figure 4-6 (c) shows its location which is at the middle of the cooler to represent the heat generated by the TPV cell. An emissivity

value of 0.91 was used for all surfaces since it is assumed that they will be painted with a high emissivity paint such as AZ-93. Regarding the mesh, a maximum element size of 0.008 cm and a minimum size of $1x10^{-5}$ cm were used.

Next, the simulations involved varying the materials horizontally, vertically, and diagonally to examine the performance of radiative coolers with multiple materials used in different configurations. Figure 4-7 displays the structure used with nine sections.

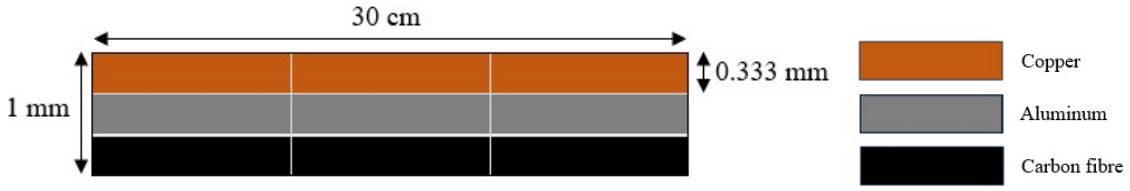

Figure 4-7: Sandwich structure with 9 sections with material legend

Figure 4-7 shows the three materials stacked vertically within the sandwich structure. The 2D revolution COMSOL simulation studied the impact of changing the order of these materials while using the same material in each row. The same boundary conditions were used as in Table 4-3. A material sweep was carried out for different configurations namely vertical, horizontal and diagonal as shown Figure 4-8.

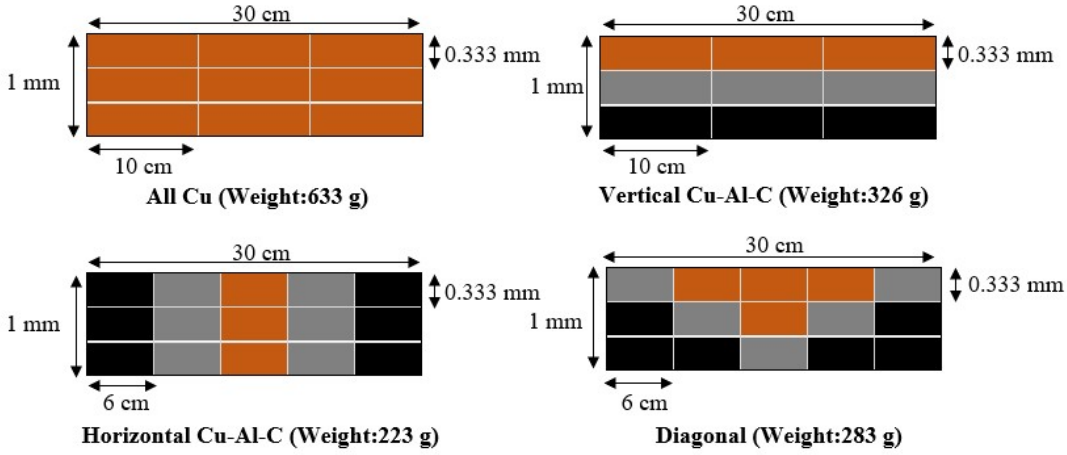

Figure 4-8: Cross-section of various circular multi-material structures with weight

These configurations help us determine how to arrange the different materials within the radiative cooler. Material sweeps were carried out for each multi-material case with a material only used once. Table 4-4, Table 4-5, and Table 4-6 show a cross-section of the cooler with all combinations used for the horizontal, vertical, and diagonal cases.

Table 4-4: Horizontal material combinations used in COMSOL simulations

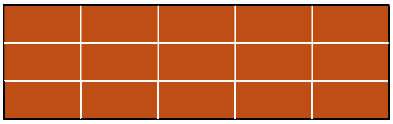 Cu-Cu-Cu	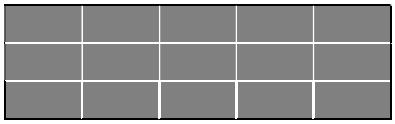 Al-Al-Al	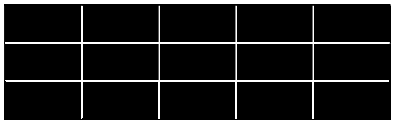 C-C-C
 Cu-Al-C	 Al-Cu-C	 C-Al-Cu
 Cu-C-Al	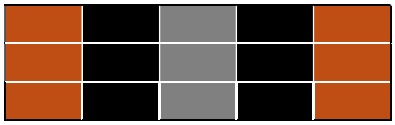 Al-C-Cu	 C-Cu-Al

Table 4-5: Vertical material combinations used in COMSOL simulations

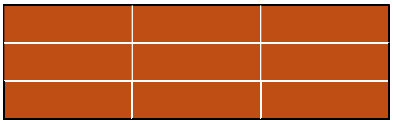 Cu-Cu-Cu	 Al-Al-Al	 C-C-C
 Cu-Al-C	 Al-Cu-C	 C-Cu-Al
 Cu-C-Al	 Al-C-Cu	 C-Al-Cu

Table 4-6: Diagonal material combinations used in COMSOL simulations

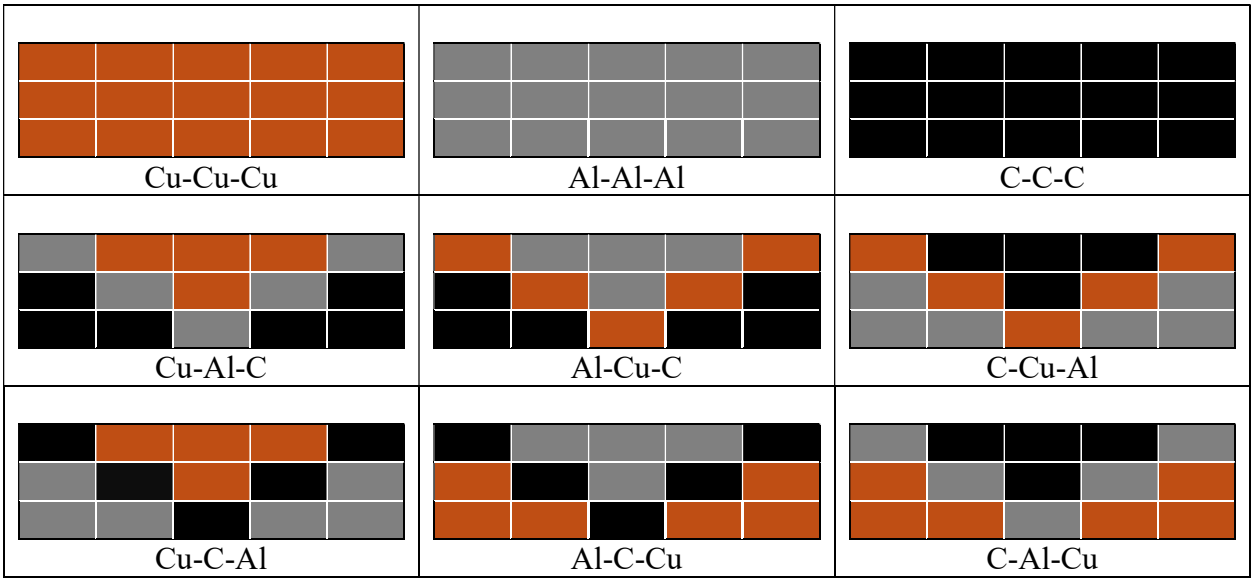

As shown in Table 4-4, Table 4-5, and Table 4-6, cases for only one material were considered as well as multi-material ones. The boundary conditions were again unchanged for all cases. Figure 4-8 also shows the weights of these cooler designs, highlighting that incorporating multiple materials can significantly reduce weight (from 633 g for copper-only to as low as 223 g) compared to using only copper. The results for all these cases were plotted and studied in order to determine the best option to be used in the experimental phase.

4.2 Experimental setup

Section 3.6 explored the key elements required for an experimental setup replicating space environment. Based on this information and testing requirement for this research, a designed experimental setup is shown in Figure 4-9.

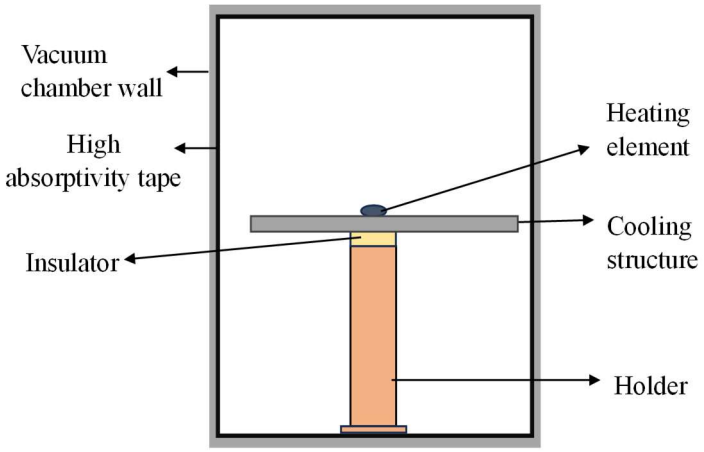

Figure 4-9: Experiment's vacuum-based setup for testing the radiative coolers

The goal of this experimental setup is to provide a method of measuring the cooling power of the test structure. In order to minimize the number of variables and reduce errors, the IR lights representing the sun are not used. To replicate the heat generated by a TPV cell, a heating element with a known power input is used. Additionally, a thermal insulator is used to minimize the amount of heat transfer via conductor to the test object holder.

4.2.1 Assembled experimental setup

The experimental setup within the vacuum chamber based on the designed setup in Figure 4-9 can be seen in Figure 4-10 (a).

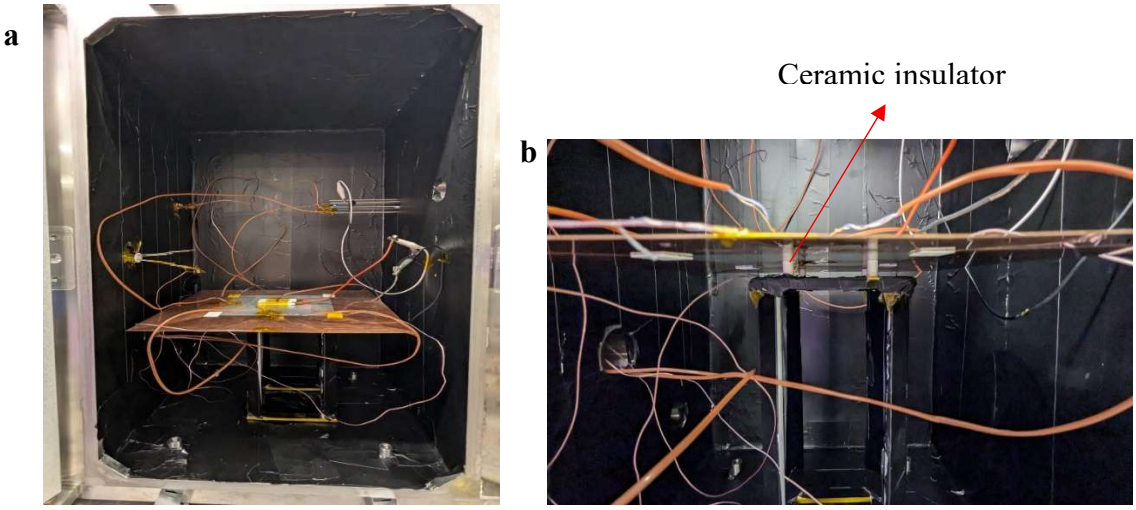

Figure 4-10:(a) Experimental setup (b) Ceramic thermal insulator

A black aluminum oxide tape was used on the walls of the vacuum chamber. An aluminum holder is used to hold the equipment with ceramic thermal insulators, shown in Figure 4-10 (b), glued on top. The purpose of the insulators is to minimize the heat transferred to the stand through conduction, hence, ensuring that the majority of the cooling is done through radiation. For the purpose of this experiment, the TPV cell was not used initially as the goal is to validate the results of the simulation regarding the cooling power. A heating element is used instead to act as the heat source. Multiple T-type thermocouples were used in the chamber to monitor the temperature of different parts of the cooling structure, the stand, and the chamber walls. The locations used are shown in Section 4.3.3 as part of the experimental measurement details. The radiative coolers discussed in section 4.2.7 were tested using this setup.

4.2.2 Vacuum chamber

The vacuum chamber selected was bought from Kurt J. Lesker Company. It has a dimension of 12” depth, 12” width, and 24” height. In order to measure the vacuum pressure, a vacuum gauge connected to a KJL 375 series benchtop controller was installed. [71] The pump used was a Varian SD-301 model which has an ultimate pressure of 1.5×10^{-3} torr. [72] The equipment used is shown in Figure 4-11.

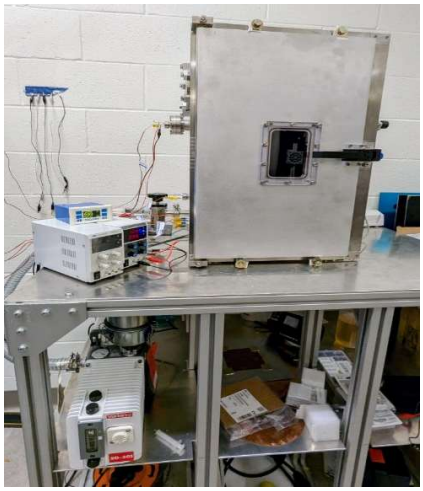

Figure 4-11: Experimental setup showing shelf, vacuum chamber, pump, power supply and benchtop controller

Installing the vacuum chamber in the lab required the design of a shelf capable of withstanding its weight. The shelf was designed on Solidworks and assembled in the lab. Aluminum extrusions measuring 45 mm by 45 mm were used as support along with a 4 mm thick aluminum sheets. The vacuum chamber was bolted to the Aluminum sheet.

4.2.3 Vacuum chamber wall temperature

Due to budget constraints, bringing the vacuum chamber to low temperatures comparable to that of outer space was not feasible. Thus, a suitable alternative had to be found. Simulations were carried out on COMSOL to analyze the impact of changing the wall temperature. The model used is shown in Figure 4-12.

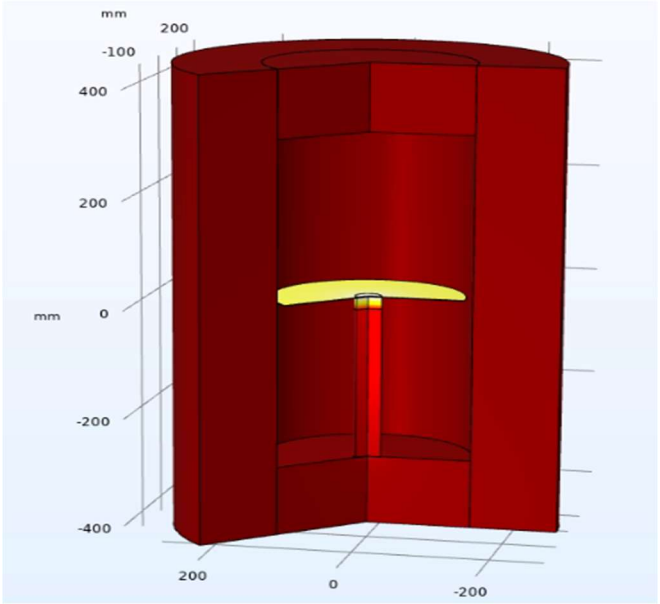

Figure 4-12: Vacuum chamber model

A 2D revolution simulation was carried out with a radiative cooler placed on a stand inside a chamber. A heat source is place on top of the cooler to represent a TPV cell and a ceramic thermal insulator is placed underneath the cooler to minimize conduction. The size of the walls was similar to the one used in the lab, however, it was approximated as a cylindrical shape for faster computation. The model had an interior height of 24" with a diameter of 12" compared to the real chamber which had the same height but a 12" by 12" square interior. An extremely fine triangular mesh was used with a minimum element size of 0.0172 mm and a maximum of 8.61 mm. A heat flux of 100 W was applied to the top of the heat source. The wall temperature is represented by the ambient temperature. The model was analyzed for three different temperatures, namely 100 K, 200 K, and 298 K. The temperature gradient across the radiative cooler was compared and the results are shown in Figure 4-13.

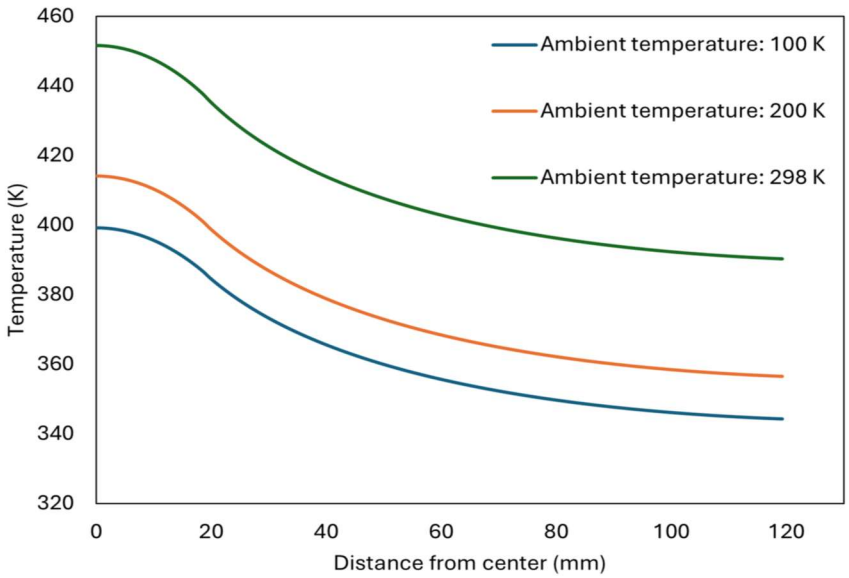

Figure 4-13: Temperature gradient across cooler for different ambient temperatures.

The results show that the temperature across the cooler rises as the ambient temperature rises. The temperature gradients are similar with smaller gradient near the heat source at the center and a steeper drop as we move away from it. Towards the outer edges as the surface area increases, the temperature gradient decreases. This is as expected since a lower wall temperature would lead to a higher rate of heat transfer by radiation as per the Stefan-Boltzmann law. However, the temperature rises by approximately the same amount across the structure. This indicates that the results are proportional to the wall temperature. Hence, for validation purposes, the experiment can be done at room temperature and a COMSOL simulation carried out to replicate the same environment. The results will then be compared to measure the level of accuracy of the simulation. If the results from the simulations are the same as those from the experiments within an acceptable margin of error, it can be concluded that the simulations are accurate and changing the parameters of the simulation would produce fairly accurate results. The verified model could, henceforth, be used with a lower ambient temperature to represent the colder ambient temperature in space.

4.2.4 Absorbing tape

In order to replicate the space environment, the vacuum chamber walls need to absorb as much of the radiation incident from the radiative cooler to represent heat rejection into deep space. Reflected rays from the walls may be absorbed back by the cooler leading to higher measured temperatures and inaccurate calculation of cooling power. The chosen solution involves taping the walls of the chamber with NC233 matte black tape which is made from a layer of nano carbon painted onto aluminum leading to high absorption. [73] The absorptivity of the tape was measured using a Vertex 70 Fourier Transform Infrared (FTIR) spectrometer along with an integrating sphere as shown in Figure 4-14 below.

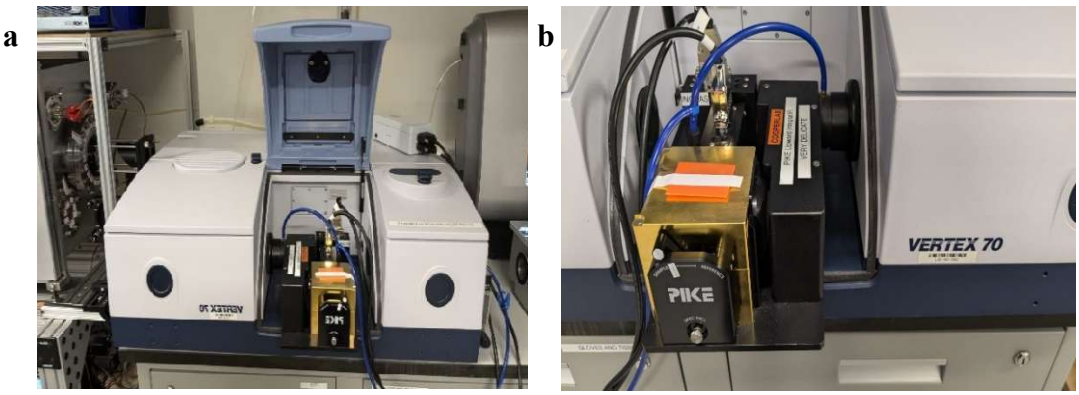

Figure 4-14: (a) Vertex 70 FTIR spectrometer (b) Integrating sphere

A sample of the tape was tested. The spectrometer works by sending an infrared beam in the mid-IR range towards the sample which either absorbs, transmits, or reflects it. A detector inside the integrating sphere detects the reflected light and the information is recorded and processed in order to plot the reflectance spectrum. The FTIR performs a correction to account for any background interference. The following equation can then be used to find the desired value:

$$Absorptance + reflectance + transmittance = 1 \qquad \textit{Equation 19}$$

The total is always 1 since the light can only be absorbed, reflected, or transmitted. For the black tape, transmittance is 0 since it is fully opaque. For non-opaque samples, another test needs to be done for transmittance. The absorptance is, thus, found from the reflectance data obtained from the FTIR spectrometer. The following result was obtained for the black aluminum tape:

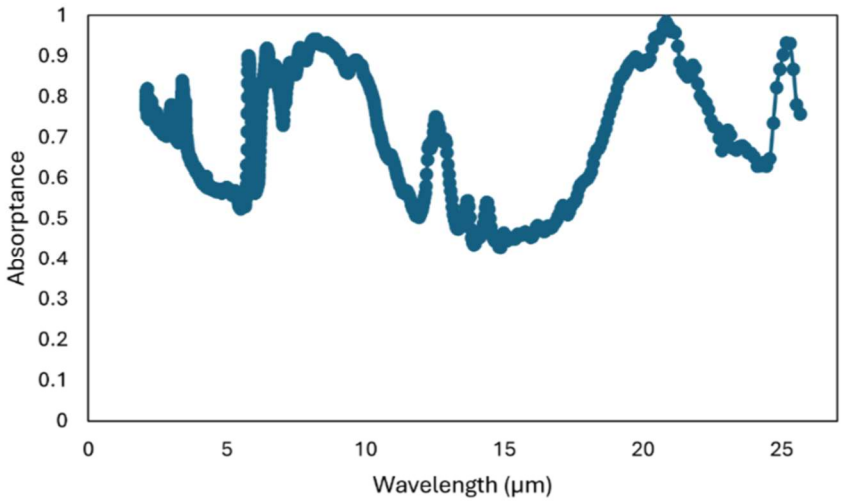

Figure 4-15: FTIR absorptance result for black aluminum tape

The FTIR tests were carried out three times and the values showed an average standard deviation of 0.00728 indicating consistent results. This result is for hemispherical spectral absorption but for the COMSOL model the hemispherical total absorption is required. The following equations can be used to find the required value:

$$\varepsilon = \frac{\int_{\lambda_0}^{\lambda_{max}} \varepsilon_\lambda E_{\lambda b} d\lambda}{E_b} \qquad \textit{Equation 20}$$

Planck's law: $$E_b = \frac{C_1}{\lambda^5 [e^{C_2/\lambda T} - 1]} \qquad \textit{Equation 21}$$

The hemispherical total absorption was calculated to be 0.71 for the black tape which implies 71% of the incoming radiation emitted by the radiative cooler would be absorbed. Additionally, due to the view factors within a vacuum chamber, most of the rays reflected from the tape would more likely be absorbed by the other walls of the vacuum chamber rather than the radiative cooler itself. This was adequate for this experiment.

4.2.5 Support for the radiative cooler

The radiative cooler requires a support when it's being tested. Since the goal of the experiment is to measure radiative cooling power, heat transfer by conduction needs to be minimized. A simple holder was made to hold the object as shown below in Figure 4-16.



Figure 4-16: Support for the radiative cooler

Four supports, with 8 mm diameter and 12 mm in length, made from Alumina were glued to a stand made of Aluminum. This material was chosen due to its low thermal conductivity of 25 W/m·K. Furthermore, the four protruding supports have a relatively small contact area, and both these factors contribute to minimizing the amount of heat loss from the cooler to the holder. The same black aluminum oxide tape used for the vacuum chamber was used to cover the holder as well. This was done to minimize the reflection of the incoming radiative rays coming from the cooler.

4.2.6 Heating element

A heating element had to be chosen to be used in the vacuum chamber to provide the heat flux that would come from the PV cell. After testing several emitters made of different materials such as graphite and ceramic, a positive temperature coefficient (PTC) ceramic heating element (C.12v – 220 ℃/428 °F) [74] was chosen due to its specific characteristic shown in Figure 4-17 (a) below:

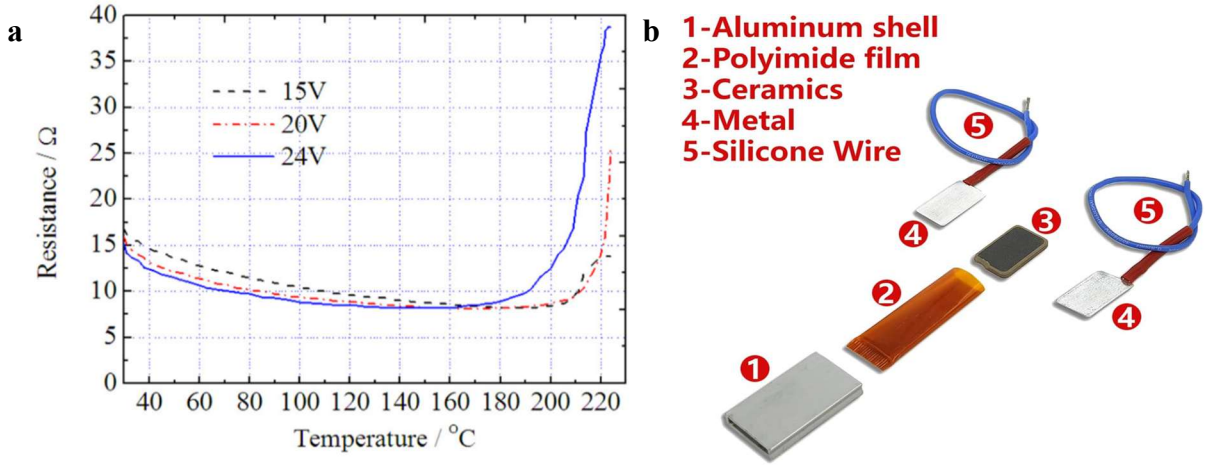

Figure 4-17: (a) Behaviour of a PTC ceramic heater [75] (b) heating element [74]

As its temperature increases, its resistance changes and once it reaches its rated temperature, there is a large increase in resistance. This implies that the maximum temperature the heating element reaches can be reliably and reproducibly determined by monitoring the changes in resistance of the heater. The resistance is calculated using the voltage and current readings obtained from the power supply readings. Since the resistance shows a large increase at

approximately the same temperature, this temperature can be used reproducibly in different experiments to determine the cooling power of the radiative coolers. A better cooling structure would require a greater power input to reach the same heating element temperature and the difference between multiple cases can be used as a way to determine the changes in cooling power. Figure 4-17 (b) shows the structure of the heating element which consists of a PTC ceramic element on the inside that is heated by an electric current. This element is in contact with an outer aluminum shell which can be used to provide smooth even contact with the cooling structure.

4.2.7 Radiative cooler

The experimental setup required a radiative cooler that could be in proper contact with the heating element while providing a measurable amount of cooling. Figure 4-18 shows this heating element used in the lab as well as a radiative cooler made with copper and aluminum.

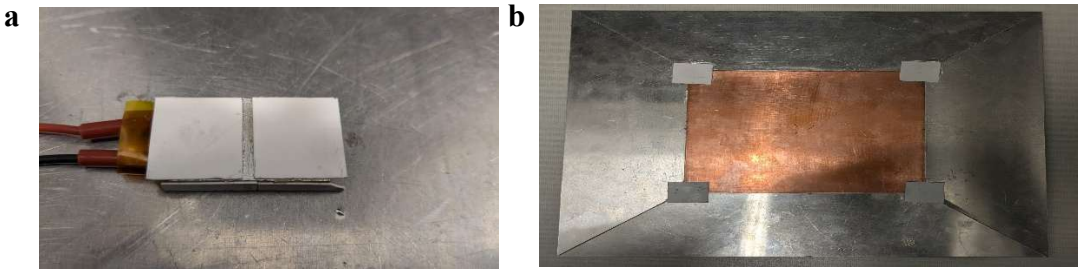

Figure 4-18: (a) Heating element used (b) Radiative cooler

Figure 4-18 (a) shows the heating element, and it can be seen that there are ceramic pieces glued onto it. This was done to minimize the radiation losses occurring from the heating element itself and ceramic was used due to its low emissivity. The bottom of the heating element was unchanged with its Aluminum shell in contact with the radiative cooler. Figure 4-18 (b) shows the radiative cooler constructed in the lab. The dimensions of the radiative cooler components are shown in Figure 4-19.

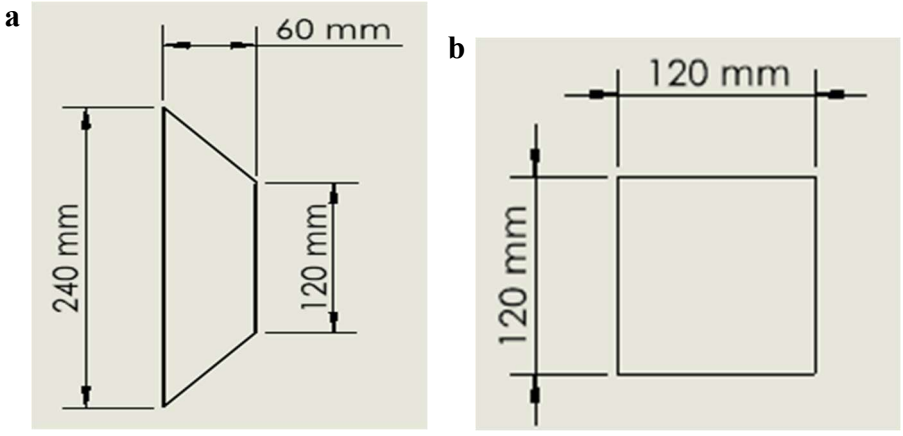

Figure 4-19: Radiative cooler component dimensions (a) aluminum panel (b) copper center

The structure was 24 cm by 24 cm in size. Four aluminum panels were cut from a 0.5 mm thick sheet with the dimensions shown in Figure 4-19 (a) while the copper center was 12 cm by 12 cm in size with the same 0.5 mm thickness. The arrangement can be seen in Figure 4-20.

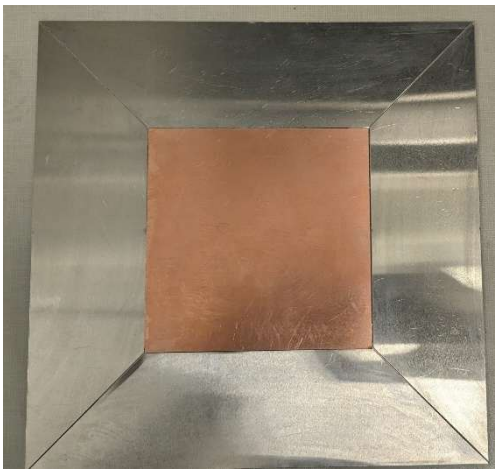

Figure 4-20: Radiative cooler without ceramic pieces

In Figure 4-20, 4 aluminum panels from Figure 4-19 (a) surrounds the copper panel from Figure 4-19 (b). Glued ceramic pieces were used to hold them together and maintain proper contact as shown in Figure 4-18 (b).

The chosen materials were copper and aluminum as they are both commonly used for cooling both in space and on Earth. Furthermore, the two material have distinct properties suitable for comparison as shown in Table 4-7.

Table 4-7: Comparison of material properties

Material	Thermal conductivity (W/m·K)	Density (g/cm^3)	Emissivity
Copper	400	8.96	0.03
Aluminum	237	2.7	0.04

Copper has a higher thermal conductivity which makes it a better material for cooling as it can dissipate heat faster, however, its density is significantly higher compared to Aluminum and this is why Aluminum is usually used in space. It can be observed that both materials have very low emissivity when they are polished. However, for space applications, a coating needs to be applied on the metal surfaces, thus changing their emissivity. A high temperature black ceramic coating will be used for both metals.

The two metals had to be joined together to achieve heat transfer between the two panels. The Aluminum panels were joined together with small ceramic plates attached with silicon glue at the edges of the inner copper plate. The size of the radiative structure was limited to 24 cm by 24 cm due to the size of the vacuum chamber. A thickness of 1 mm was used. This method of joining

the panels was chosen after considering several alternatives, namely, magnets, hinges, braided copper, and thermal graphite sheets. Ultimately, ceramic pieces were chosen to properly demonstrate the multi-material aspect of the cooling structure while minimizing heat transfer through other methods. The heating element was attached tightly to the cooler using Kapton tape, thus, applying a small amount of pressure between the two surfaces.

4.2.8 Power supply and temperature measurement

To replicate the heat flux present in a TPV setup, the ceramic heater was powered with an electrical power supply (Skytoppower STP6005H), which is shown in Figure 4-21 (a).

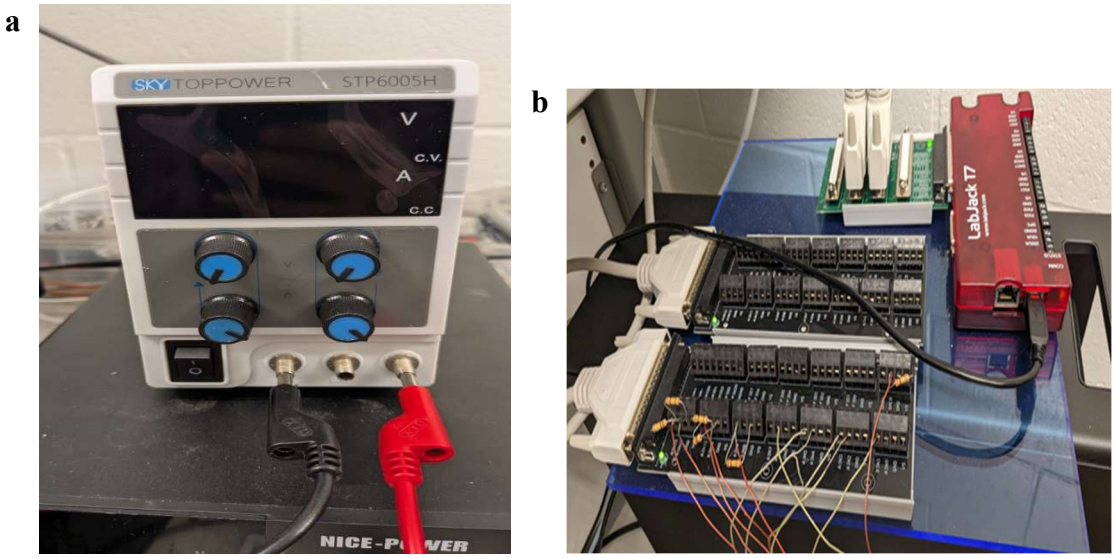

Figure 4-21: (a) Skytoppower STP6005H (b) Labjack T7

This power supply can provide a DC output of up to 60 V and 5 A. To measure the temperature of the radiative cooler, thermocouples also had to be used. Ungrounded t-type thermocouples were chosen due to their lower standard limits of error of ±1 °C. [76] A Labjack T7, pictured in Figure 4-21 (b) was used for data acquisition along with the Kipling software on a PC. All thermocouples used were calibrated by using boiling water and ice as the reference points to derive equations for determining temperature values that were measured with the assistance of Kipling and LJLogM software.

4.2.9 TPV system integrated testing setup

The next experiment stage involves testing the cooler as part of a TPV system. As shown in Figure 1-1, a TPV system consists of a heat source, a high temperature emitter, a TPV cell, a cooling system as well as photon reflectors and a spectral filter. Since the goal of the experiment is to focus on the cooling performance, a 50 W Philips halogen bulb [77], shown in Figure 4-22 (a) was chosen to act as both the heat source and emitter.

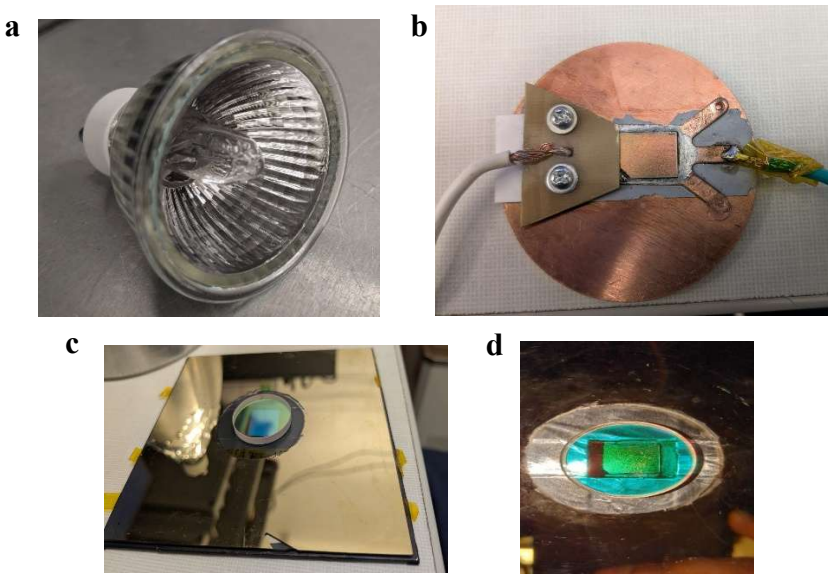

Figure 4-22: (a) Halogen bulb (b) TPV cell (c) photon reflector and selective filter (d) close-up of cell and filter

As shown above, the bulb has a shiny reflector that reflects and focuses the light in one direction. The heated tungsten filament inside provides a suitable emission spectrum for a TPV system. Figure 4-22 (b) above shows the TPV cell used for this experiment. In order to use the cell, the cell was attached to a copper substrate with a Thermalright Odyssey thermal pad [78] to enhance heat conductivity and provide electrical insulation. Wires were soldered onto copper fingers in contact with the cell in order to make use of the power generated by the TPV cell. Figure 4-22 (c) and (d) show the photon back-reflector along with the selective spectral filter placed on top of the opening for the TPV cell. The back-reflector was made using a thin layer of gold sputtered onto glass while the spectral filter was purchased. Both of them aid in improving the efficiency of the system by reflecting unused photons and mostly allowing useful photons to reach the TPV cell, hence, reducing waste heat and lowering the cooling demand. The spectral filter used was a TECHSPEC OD 2.0 Shortpass Filter from Edmund optics with a cutoff wavelength of 1600 nm as illustrated by the transmission spectrum shown in Figure 4-23. [79]

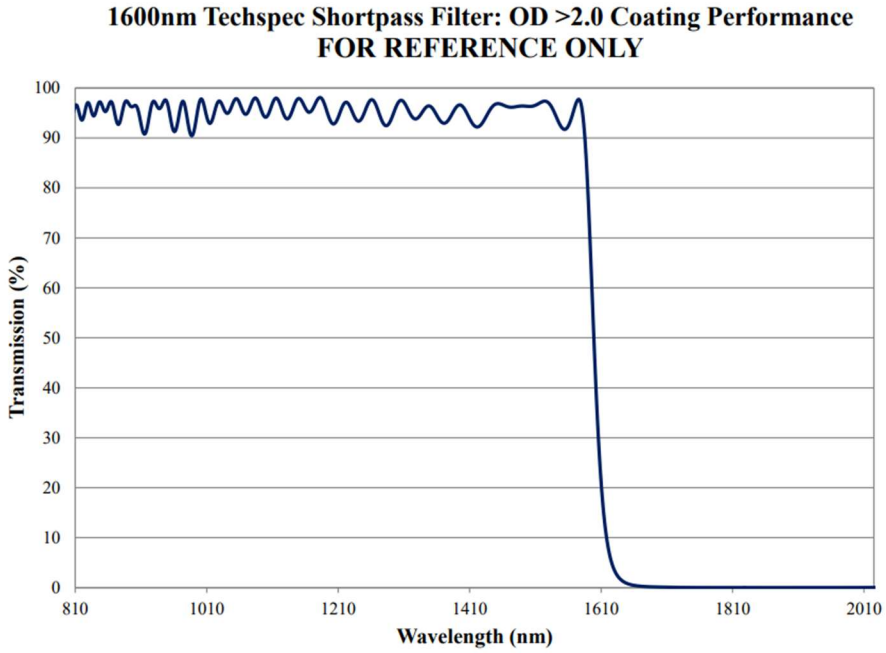

Figure 4-23: Spectral filter transmission spectrum [79]

Figure 4-23 shows that the filter transmits over 90 % of incident rays with wavelengths less than 1600 nm, and the transmission rapidly drops to zero as the wavelength of the incident light increases beyond 1600 nm.

A semi-elliptical cavity was used for photon recycling and to improve system efficiency. The photons reflected by the back reflector, the spectral filter, and the TPV cell itself would be directed towards the walls of the chamber without the presence of the cavity. The reflective aluminum interior allow these photons to be recycled back into the system by reflecting them back towards the bulb. This allowed more of the light emitted by the bulb to reach the TPV cell without being lost to the surroundings. It has to be noted that the elliptical cavity was not a perfect reflector and hence, absorbed a small amount of the incident photons. All these components were combined to create the complete testing setup shown in Figure 4-24.

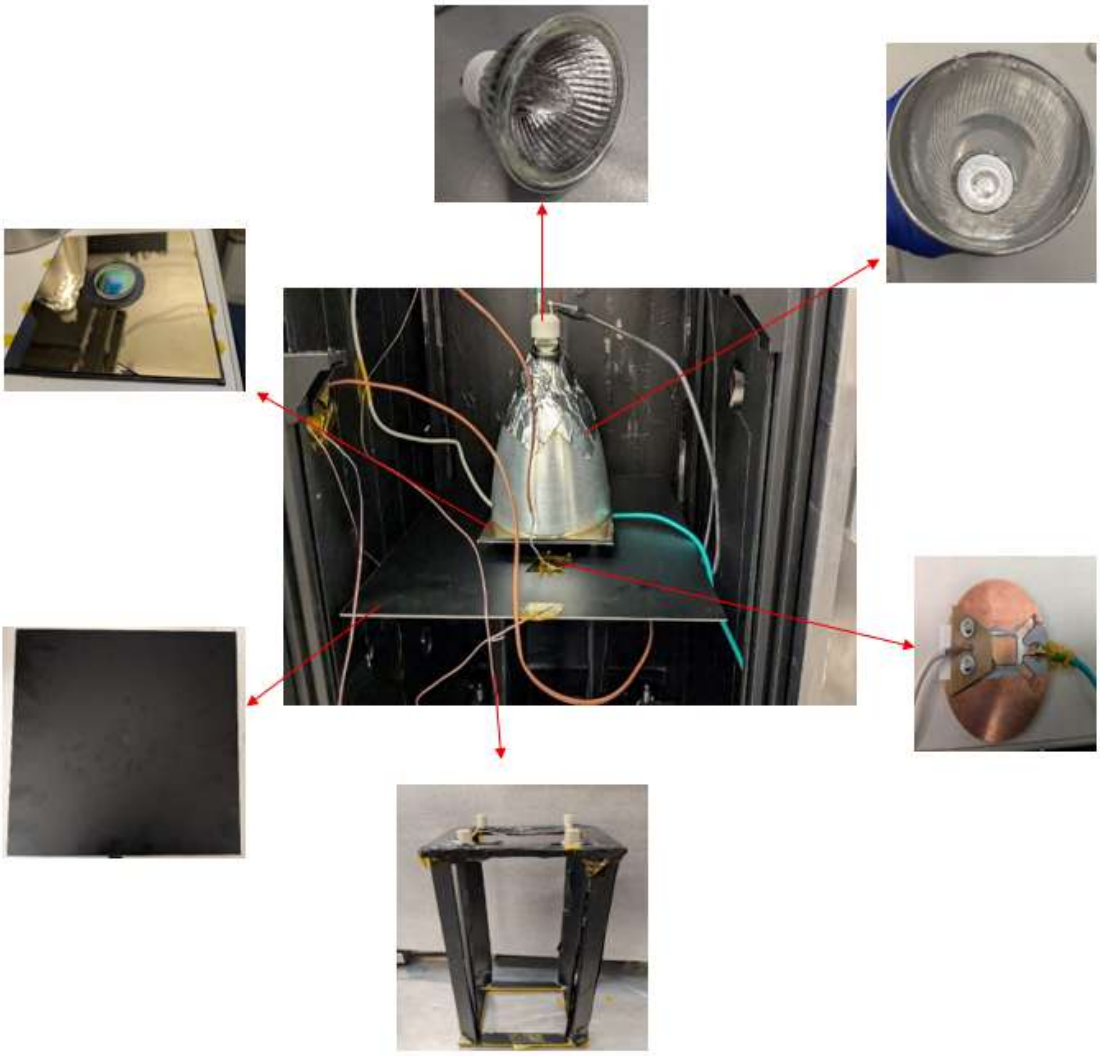

Figure 4-24: Complete TPV testing setup

The components were assembled in the vacuum chamber as shown above. The substrate containing the cell was placed in contact with the radiative cooler such as the black aluminum cooler. The photon reflector glass was placed above the cell and the selective filter was placed above an opening allowing light through similar to Figure 4-22 (d). The semi-elliptical was cut near its focal point such that the bulb could be placed at its focal point as shown in Figure 4-24. This allows the light to travel directly onto the cell. The maximum radius of the semi-elliptical cavity was the same as the width of the glass used as the photon back-reflector. This ensured that the position of the bulb is the same in all experiments and that the bulb is properly centered and directing the majority of its emitted photons towards the cell placed in the middle.

4.2.10 Measurements

For these experiments, the data recorded was the temperatures recorded by the T-type thermocouples, the vacuum pressure level, the power input coming from the power supply, as well as the power output generated from the cell. As previously discussed, the thermocouple data is

recorded on Kipling with the thermocouples placed at multiple different locations to measure the temperature of the following:

1. TPV cell
2. Panel intersections
3. Outer edge of the radiative cooler
4. Bottom part of cooler at center
5. Stand temperature
6. Vacuum chamber wall
7. Ambient air

These measurements are needed to monitor changes in ambient and surrounding temperatures in order to account for environmental variations and conduction losses. Measurements along the radiative cooler allows us to plot the temperature gradient across it and use it to validate simulations done on COMSOL. The TPV cell temperature was monitored to avoid excessive temperatures that could damage the cell and to have a metric that could be used for comparison to determine cooling capabilities.

The power input and vacuum pressure levels were read from the power supply and the vacuum gauge connected to the chamber.

Finally, the power output of the cell had to be measured, and this needed to be done by creating an IV curve for each case. Figure 4-25 shows the circuit used for measurements.

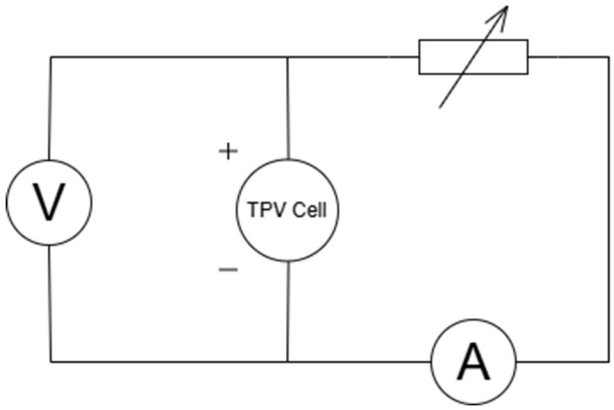

Figure 4-25: Circuit for IV curve measurements

In Figure 4-25 above, a potentiometer is used to vary the resistance. An ammeter is connected in series to measure current, and a voltmeter is used in parallel with the TPV cell to measure voltage. The resistance was gradually changed and readings for current and voltage were recorded and plotted in an IV curve.

4.3 COMSOL modeling

In Section 4.1, preliminary models were done to gain a better understanding of the factors affecting cooling. However, these models use general parameters available in literature or obtained from manufacturer data. A COMSOL model needs to be done to analyse and predict the performance of the coolers used in the experimental setup. This requires a more in-depth model

with accurate parameters used in the experiment itself. To ensure that the simulation model on COMSOL is correct, the model needs to be validated with experimental results found using the experimental setup and coolers mentioned in Sections 4.2.7 and 4.2.1. Moreover, to achieve an optimized shape, parametric studies need to be carried out to obtain the best radiative cooler based on radiative power related to weight.

4.3.1 Mesh independency study

Finite element modeling requires a lot of computational power, and a simplified model is hence, commonly used to obtain accurate results faster especially when iterations are required such as in parametric studies that need to be carried out. A mesh independency study needs to be carried out to determine whether the simplified model can provide accurate results. A COMSOL model was created using actual sizes used for the emitter, copper, and aluminum as shown in the model in Figure 4-26 (a) below.

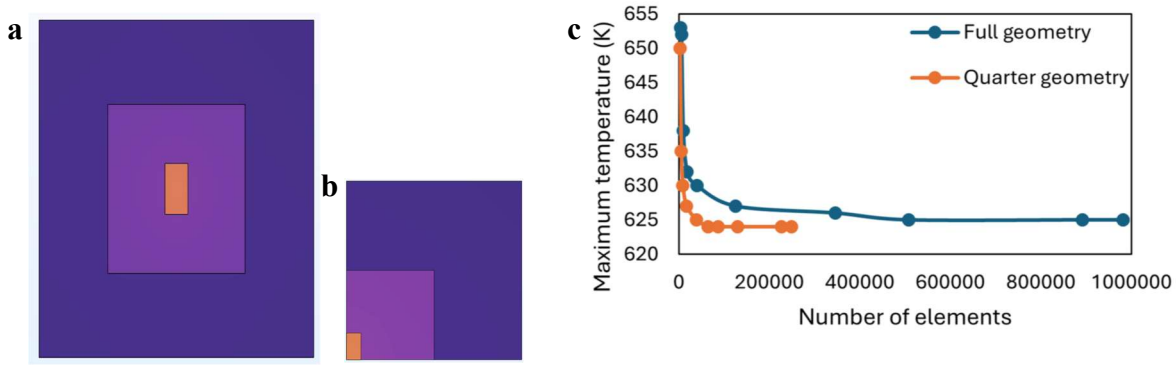

Figure 4-26: (a) Full geometry (b) Quarter geometry (c) Maximum temperature as a function of the number of mesh elements

The COMSOL model used the heat transfer module as well as the surface-to-surface radiation module. A mesh independency study was carried out for the full geometry and symmetry was used to only consider a quarter of the geometry. The in-built symmetry function in COMSOL was used to adjust the boundary conditions. The full geometry required around 500,000 elements when using a minimum mesh size of 0.36 mm and maximum size of 8.4 mm while the quarter geometry required only around 64,000 elements with a minimum mesh size of 1.2 mm and maximum of 9.6 mm to reach the same results. This shows that using a quarter of the geometry can lead to accurate results in much faster time.

4.3.2 Model parameters

COMSOL models perform calculation based on the boundary conditions and parameters provided. The accuracy of the model is heavily dependent on accurate values being used. For this radiative cooling problem, the following parameters need to be considered:

1. Thermal conductivity of copper
2. Thermal conductivity of aluminum

3. Thermal conductivity of alumina ceramic
4. Emissivity of copper
5. Emissivity of aluminum
6. Emissivity of alumina ceramic
7. Conductance between heat element and copper
8. Conductance between copper and aluminum
9. Power input

4.3.2.1 Emissivity

The emissivity values can be found using FTIR measurements and the same method used to determine the emissivity of the absorbing tape in the vacuum chamber as described in Section 4.2.4. Measurements were taken for all three materials, namely, copper, aluminum, and alumina ceramic, and analyzed to find the real emissivity value. Measurements were repeated three times for each sample.

4.3.2.2 Thermal conductivity

Thermal conductivity is a function of temperature. However, the temperature range for this project is low as far as the radiative cooler itself is concerned. Since the TPV cell has an operating temperature of 300 K and typically not used past 333 K to avoid potential cell damage, the experiment was carried out over a small temperature range. Figure 4-27 shows the thermal conductivity of copper and aluminum samples.

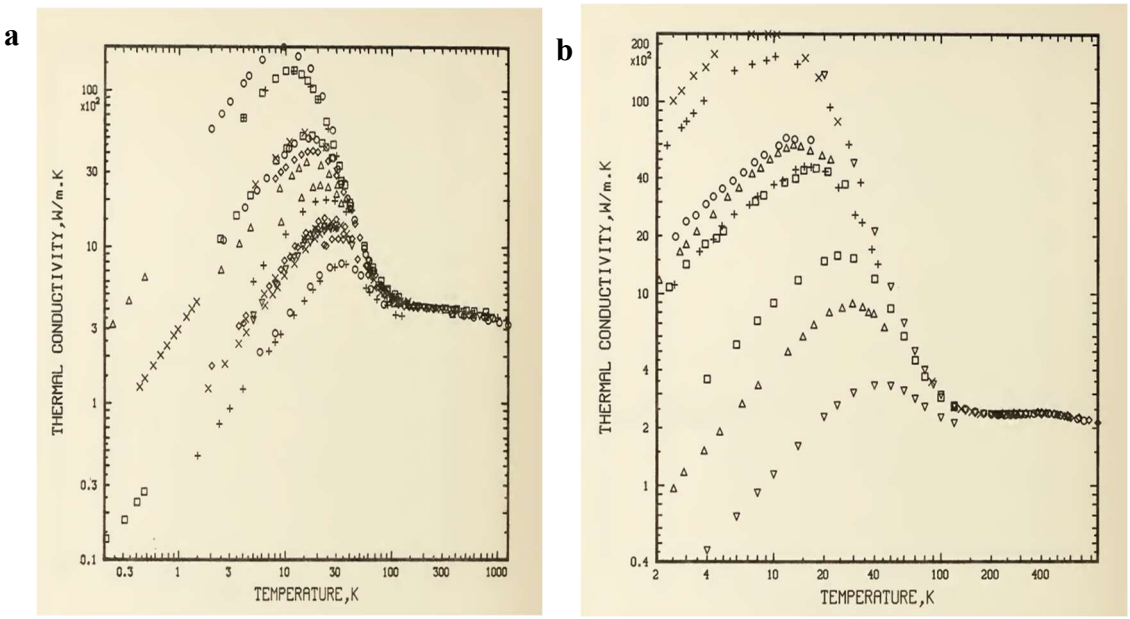

Figure 4-27: Thermal conductivity of multiple (a) copper samples (b) aluminum samples against temperature [80]

It can be observed that in both Figure 4-27 (a) and Figure 4-27 (b), there was a lot of variance at lower temperatures especially due to the purities of the samples that were tested. In the figure, the curves are from different studies carried out that recorded thermal conductivity data at various temperatures. The sample purity variance resulted in discrepancies between recorded

results especially at lower temperatures. Nonetheless, in the range between 300 K to 333 K, the thermal conductivity values for both copper and aluminum are very consistent across several studies and are in line with the theoretical values usually used which are 400 W/m·K for copper and 237 W/m·K for aluminum. Hence, these values can be used for the simulation models with a high degree of confidence.

4.3.2.3 Interface conductance

The next values needed were the conductance between the heat element and the copper as well as the conductance between the aluminum and copper panels. In section 2.1, the background review showed that conductance across an interface can be affected by several factors, such as, temperature, contact pressure, surface roughness, and trapped gases. Hence, theoretical values cannot be used in this case due to the high degree of variability especially in the case involving the two panels which would have greatly differing conductance values based on how well they are joined together in terms of contact pressure and surface roughness. For example, based on the results shown in Figure 2-3, the conductance between these panels would be expected to be around 6000 - 12000 W/m^2K. To find more accurate values, the experimental data was used. The details are discussed in Section 4.3.3.2.

4.3.2.4 Power input

Finally, the last value needed was the power input used in the experiment. The readings for voltage and current were giving directly by the power supply shown in Section 4.2.8. However, a correction needed to be done for the practical losses occurring in the wires used.

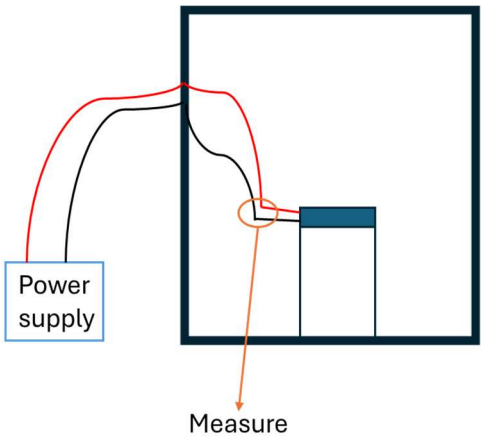

Figure 4-28: Power error measurements

As shown in Figure 4-28, the current and voltage were measured inside the vacuum chamber at the point of contact between the wires of the heating elements and the extension wires connected to the outside of the chamber. These results were used to calculate the power reaching the emitter and compared to the power calculated from the voltage and current displayed on the power supply. The % loss was found and used to adjust the power value used for the applied heat flux in the COMSOL model.

4.3.3 Model validation experiment

A model validation process had to be performed to confirm that the theoretical results match reality. This was carried out experimentally using the setup outlined in Section 4.2.1 and the illustration that had been shown in Figure 4-10 with the PTC ceramic element used on top of the copper-aluminum cooler. The setup was also used to find more accurate conductance values needed for the simulation. To compare the obtained results from simulation with the experiment, the temperature gradient across the cooler needed to be found.

4.3.3.1 Experiment and measurements

The heating element was placed at the middle of the radiative cooling structure with the help of Kapton tape which applied some contact pressure between the two. Multiple T-type thermocouples were attached across the structure as shown in Figure 4-29.

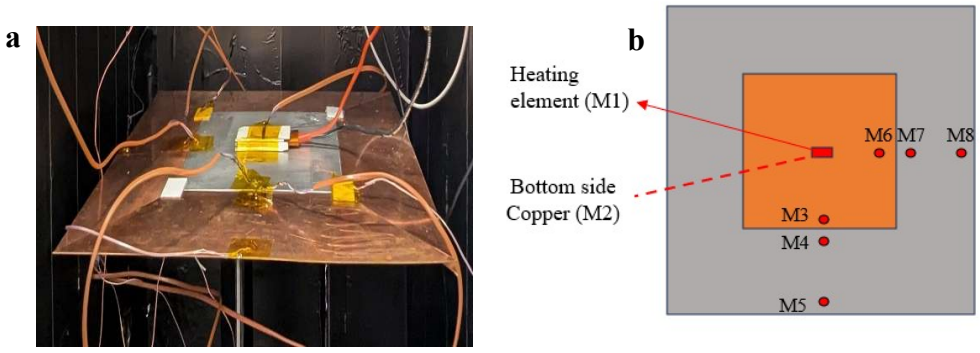

Figure 4-29: (a) Radiative cooler with the heating element and thermocouples (b) Location of thermocouples

As shown above in Figure 4-29, the thermocouples were placed along two straight lines starting from the center of the heat element and ending at the outermost edge of radiative cooler. Since the radiative cooler was assembled with four different aluminum panels attached to one central copper panel, the temperature readings may vary in different directions. Hence, the use of two different lines and averaging the results can reduce the error caused by non-ideal panel interconnections. A thermocouple was also placed at the bottom of the cooler in the middle and the temperature of the chamber walls representing the ambient temperature was monitored as well.

The cooling structure placed on a stand with insulating ceramic supports was placed in the vacuum chamber as shown in Figure 4-29 (a) and a pump was used to bring the vacuum level down to 10 mTorr. The power supply was then used to raise the input voltage from 2 V to 14 V in increments of 2 V. The temperature across the radiative cooler was allowed to reach steady state and the values recorded before each interval change.

Due the characteristics discussed in Section 4.2.6, the PTC heating element keeps heating up until it reaches its rated temperature of 220 °C where a large increase in resistance starts to occur limiting the amount of power supplied to it. The readings for both voltage and current from the power supply were recorded to confirm this increase in resistance and limitation in power input.

This process was repeated three times for each cooler tested which included the following:

1. 24 cm by 24 cm black-painted Copper-Aluminum cooler.
2. 24 cm by 24 cm Copper-Aluminum cooler.
3. 24 cm by 24 cm Aluminum-Copper cooler.
4. Small copper cooler (3.6 cm by 2 cm)
5. Small aluminum cooler (3.6 cm by 2 cm)

The multi-material configurations were arranged similarly as in Figure 4-29 (b) and all cases had 0.5 mm thickness. These configurations were chosen to compare the impact of different configurations as well as to confirm the effectiveness of using the black paint. The small copper and aluminum pieces were used as baselines and for conductance value calculations. The amount of power required for the PTC heating element to reach 220 °C was expected to be different for all cases with the best cooling structure requiring the most power input and the worst structure acting as baseline requiring the least power input.

4.3.3.2 Conductance values calculation

Going back to the conductance values required for the simulation, the experimental results obtained were used. Using Equation 1 and Equation 3 discussed in background Section 2.1, the conductance value can be calculated using the following equation:

$$C = \frac{Q_{cond}}{A\Delta T} \qquad \text{Equation 22}$$

Conductance values need to be found for the heat conduction occurring between the heat element and the cooling structure as well as for the heat transfer between the copper and aluminum panels. Figure 4-30 shows the locations where the required temperature values were recorded.

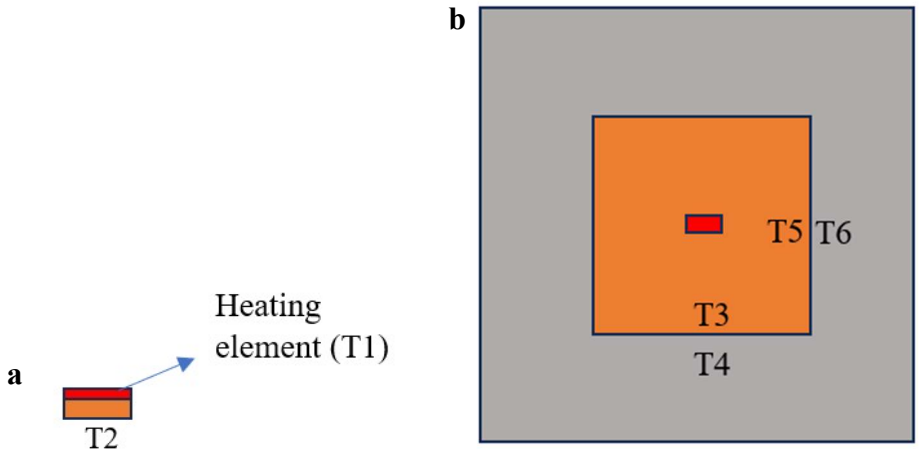

Figure 4-30: Temperature measurements (a) copper and heat element intersection (b) panel intersections

The conductance between the heating element and the copper plate were found using temperatures T1 and T2, shown in Figure 4-30 (a). A small copper sample with the same dimensions as the heating element was used for testing to minimize errors due to radiative losses. A power input was applied to the heating element and the steady-state temperature at the bottom of the copper piece was recorded and used alongside the temperature of the heating element to determine the interface conductance between the heating element and the radiative cooler.

The conductance values between the copper and aluminum panels also had to be found. Since the panel had four different intersections, the conductance value had to be approximated from the values obtained. Two intersections were considered and the temperature readings T1, T2, T3, T4, T5 and T6, shown in Figure 4-30, were used for the interfacial conductance calculation.

The power input had to be adjusted for losses from wires and from radiative emissions occurring from the heating element, thus, giving the following 2 equations:

$$C_{heating\ element\ and\ copper} = \frac{P_{in} - P_{radiative\ losses} - P_{wire\ losses}}{A_{Heater-Cu}\,(T_1 - T_2)} \qquad \text{Equation 23}$$

$$C_{copper\ and\ aluminum\ panels} = \frac{P_{in} - P_{radiative\ losses} - P_{wire\ losses}}{A_{Cu-Al}\,\frac{(T_3 - T_4) + (T_5 - T_6)}{2}} \qquad \text{Equation 24}$$

$A_{Heater\text{-}Cu}$ is the area of contact between the heating element and the copper part of the cooler while $A_{Cu\text{-}Al}$ is the area of contact between the copper and aluminum panels. Equation 23 and Equation 24 were used to calculate the interfacial conductance values needed for the simulation input.

4.3.3.3 Comparison between experimental and simulation results

With all parameters required obtained and mesh size chosen, the simulation was carried out using COMSOL. The black copper-aluminum cooler was the one analyzed with the aluminum shell of the heating element in contact with it in the middle. Table 4-8 shows the values of the parameters used.

Table 4-8: COMSOL validation simulation parameters

Module	Parameter	Value [units]
Material	Copper – thermal conductivity	400 [W/mK]
	Aluminum – thermal conductivity	238 [W/mK]
Heat transfer	Ambient temperature	298 [K]
	Conductance between heat element and cooler	1336 [W/m^{2}K]
	Conductance between Al and Cu panels	4472 [W/m^{2}K]
	Heat source	1.6 W
Surface-to-surface radiation	Emissivity: heating element	0.67
	Emissivity: panels	0.87
	Ambient temperature	298 [K]
Mesh	Maximum element size	2.4 [mm]

	Minimum element size	0.024 [mm]
	Maximum element growth rate	1.3
	Curvature factor	0.2
	Resolution of narrow regions	1

The values for conductance and heat source, shown in Table 4-8 above, were adjusted based on the use of a quarter-geometry. The temperature gradient across the cooler was obtained and plotted. In order to validate these results, they were compared with experimental values. The values recorded during the experiment were averaged and that included the temperature gradients in two different chosen directions in all three experimental trials. The results were plotted alongside the simulation results. Some discrepancies were expected due to variations in contact quality between panels, and other experimental errors. Hence, the power input in the COMSOL model was also varied with a few different results obtained for comparison to see where the experimental data would fit.

Furthermore, an error analysis was conducted to confirm the suitability of the data and identify experimental issues that could be improved. The value for cooling power found by using the PTC heating element power output can be confirmed by manually calculating the cooling power of the cooler using Stefan-Boltzmann's law along with the temperature readings across the cooler. The error for this calculation can be found using the following equation:

$$\frac{\partial P}{P} = \sqrt{\left(\frac{\partial \varepsilon}{\varepsilon}\right)^2 + \left(\frac{\partial A}{A}\right)^2 + \left(4\frac{\partial T}{T}\right)^2} \qquad \text{Equation 25}$$

Emissivity errors based on the method used in this research can be as high as 5%. [81] The error for the area is 0.1 cm^2 based on measurement and machining errors. The error for the temperature is based on the thermocouple accuracy which is around 1 ℃.

4.3.4 Parametric study

The validated COMSOL model allows further studies into more panel configurations with high confidence. With simulations, a multitude of different cases can be analyzed without the need to make a prototype. Hence, the sizes of the panels can be changed with varying size of material used. Only copper and aluminum will be considered for these studies. Figure 4-31 shows an illustration of how the size of the panels are varied.

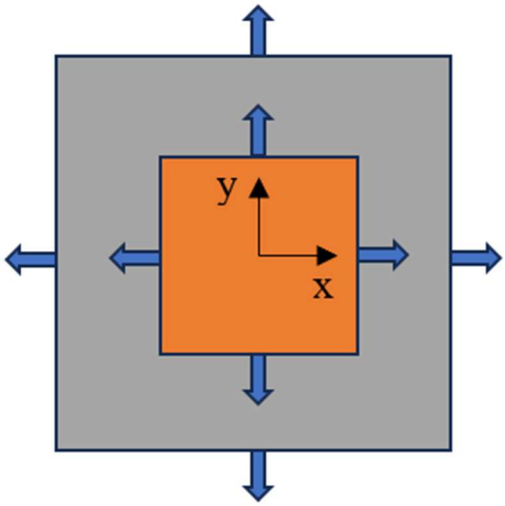

Figure 4-31: Size iterations

As shown above, the length and width of the panels are both increased independently in the x and y directions. Multiple combinations are considered using a parametric sweep in COMSOL with a constant thickness of 1 mm. The parameters were increased by set intervals to find the most useful case which involved a low cell temperature at a relatively low weight. The initial case was slightly bigger than a TPV cell and the size of the panels were stretched larger and larger. A heat flux of 20 W is applied at the middle of the structure where the cell would be placed and the temperatures obtained through the simulations are recorded for all cases. The same boundary conditions outlined in Table 4-8, shown on the previous page, are used. The studies were done for the following cases:

1. Constrained case

   This case assumes the cooler is placed inside the experimental vacuum chamber and is restricted by the size available inside. After accounting for space needed for wires and feedthroughs, the size was limited to a dimension of 24 cm by 24 cm. An initial size of 2 cm x 2 cm was used for the parametric study along with parameter intervals of 2 cm for the both the length and width of each panel.
2. Unconstrained case

   This case foregoes the restriction of being in a vacuum chamber. The cooler is allowed to get as big as possible similar to what would be possible in space. Intervals of 10 cm are used for the length and width with further refinement for the best performing range based on the results obtained.

The results obtained for all these simulations were plotted and analyzed. The temperature changes of the cell were considered to determine the best cases. The smallest case was considered as a base case since it led to the highest cell temperature. The relative temperature drop in all other cases were calculated along with the theoretical weight of all these structures based on their copper and aluminum content. The metric used to compare these cases was their relative temperature drop

to weight ratio with the goal of finding an acceptable value that maximizes the temperature drop while minimizing weight. The variation in temperature caused by weight was also plotted. The size that provided the best weight and temperature compromise was chosen to be the best case. The one chosen from the constrained case was chosen to be used in the designed experimental setup as part of a TPV system.

4.3.5 Space condition analysis

The chosen cooler was picked using data at room temperature. In order to predict its performance in space, COMSOL simulations were done using the same boundary conditions as in Section 4.3.4.

4.3.5.1 Impact of temperature

The first simulation was carried out by only changing the temperature of the surroundings. In Section 4.3.4, a temperature of 298 K was used which is significantly higher than the temperature of 3 K used for deep space. The impact of changing the temperature can be explained by Equation 8 from Section 2.3 shown again below.

$$q_{rad} = \sigma A \varepsilon (T_s^4 - T_{surr}^4) \qquad \text{Equation 8}$$

As the temperature of the surroundings goes down, the amount of radiative power increases due to the larger temperature gradient between the radiating surface and the ambient temperature since the initial values of all the other variables do not change. Hence, at 3 K, the temperature of the cell is expected to be much lower compared to 298 K. The simulation was carried out and the temperature gradients across the cooler were recorded and compared in Section 5.4.2.

4.3.5.2 Radiation in space

The next step involved taking into consideration the impact of solar and Earth radiation on the cooler as described in Section 2.5. Figure 4-32 shows an illustration of how a cooler would be impacted in the worst-case scenario.

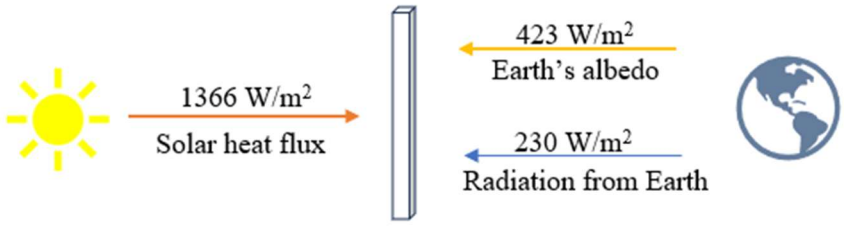

Figure 4-32: Worse case radiation from the sun and Earth on the radiative cooler. [82]

A space vessel would be affected differently by radiation depending on its view factor with regards to the sun and the Earth. For a radiative cooler, the worse case scenario would be a direct exposure to both with rays hitting its largest areas in both directions as shown in Figure 4-32. The solar heat flux is significantly higher than radiation coming from Earth's IR emissions and the

reflection of sun off the Earth. For this analysis, the cooler is assumed to have a AZ-93 coating which has a solar absorptivity of 0.15. This implies that only 15% of all the incoming rays portrayed in Figure 4-32 are absorbed by the cooler. Given the nature of this research which involves TPV, the cell location is facing the sun and a 10 cm by 10 cm area in the middle of the cooler is assumed to be shielded since this is consistent with the size of the smallest CubeSat available. The temperature gradient across the cooler was recorded and compared with the 298 K and 3 K cases.

4.4 TPV experiment

The optimized cooler found through the parametric study done for the constrained case was tested as part of the TPV system. The configuration outlined in Section 4.2.9, which includes a TPV cell, an elliptical cavity, a spectral filter, a photon reflector, a stand, and a bulb as the heat source, was utilized to assess its performance. Figure 4-33 below shows the TPV setup in operation.

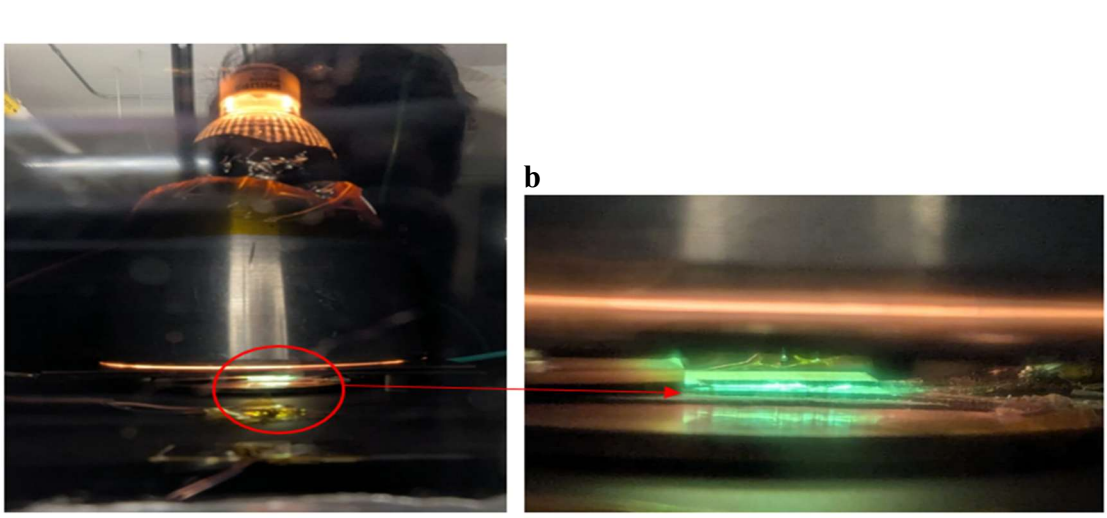

Figure 4-33: (a) TPV setup in use (b) zoomed in illuminated TPV cell

Figure 4-33 (a) shows the semi-elliptical cavity with the bulb powered using an external power source. An aluminum cavity ensured that the light did not escape towards the outside and the majority is focused onto the cell and the back reflector. A close-up of the TPV cell is also shown, in Figure 4-33 (b) with the light illuminating it after going through the spectral filter, thus, producing the green-colored light. The back reflector reflects unused photons back to the tungsten filament inside the bulb, hence, contributing to photon recycling and providing a small heating effect that improves the system efficiency. In order to improve conductance, a thermal graphite adhesive with high thermal conductivity (1800 W/mK) was placed between the TPV cell and the cooler. At the start of every round of experiments, when the components were in place, the cell output was measured at maximum power to ensure that it was properly centered, and that the performance of the bulb was not degrading over time.

As a basis of comparison, the optimized cooler was compared to other cases. For this setup, the following tests were carried out:

1. TPV cell and substrate with no cooler

2. 24 cm black aluminum cooler
3. 24 cm black copper cooler
4. 24 cm optimized multi-material cooler with copper at the center.

The no cooler case was chosen to display the improvement in cell temperature. The aluminum and copper coolers were made using the same dimensions to make them comparable to the optimized case.

This experiment was repeated using the same setup but without using a spectral filter. A spectral filter aids in cooling by filtering out unwanted out-of-band photons and allowing useful in-band photons through. This is carried out by only allowing light within a certain wavelength range through it. While the temperature is lowered, the power output is also reduced since some of the in-band photons outside the wavelength range allowed are filtered out as well. Testing the cooler without the filter provides additional information about the setup performance and the effectiveness of the cooler at slightly higher temperatures.

5 Results & discussion

5.1 Preliminary modeling

This section will show the results obtained using the steps outlined in Section 4.1. An analysis of the results will be discussed and the findings used to proceed to next steps. The flowchart below, in Figure 5-1, shows the steps followed throughout this chapter.

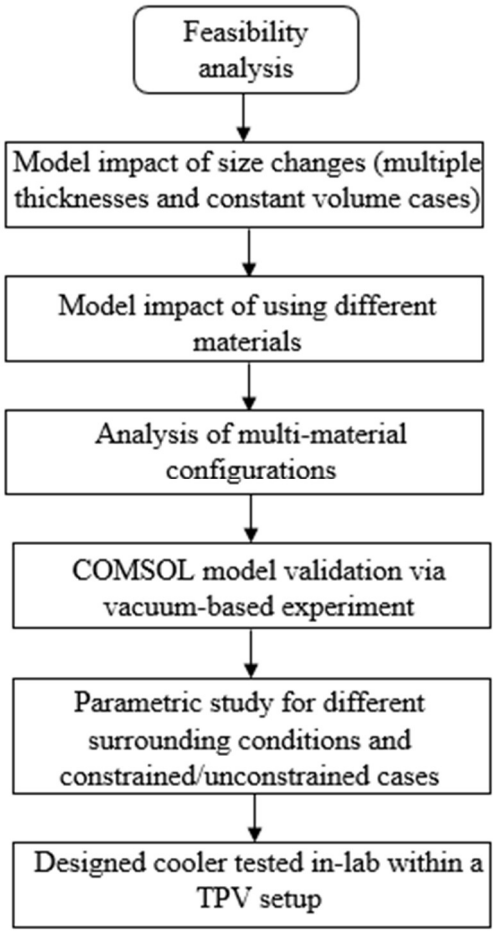

Figure 5-1: Flowchart depicting steps followed for the design of the multi-material radiative cooler

As illustrated in Figure 5-1, an initial feasibility analysis was conducted to determine initial design parameters and verify whether they were reasonable. COMSOL models were then used for further refinement and to analyse the impact of various geometric and multi-material configurations. The COMSOL model was validated using an in-lab experiment that produced comparable results. A parametric study was conducted using the same validated model to design a radiative cooler that was finally tested as part of a TPV setup.

5.1.1 Feasibility analysis

The first set of results were regarding the temperature gradient across a circular copper disc of 12.3 cm with an area of 0.0957 m^2. As discussed in the method section, this area was calculated using the Stefan Boltzmann equation to find the theoretical case where the cell temperature reaches 300 K assuming uniform temperature but in practice, the temperatures across the cell surface vary. Figure 5-2 shows the results obtained in COMSOL.

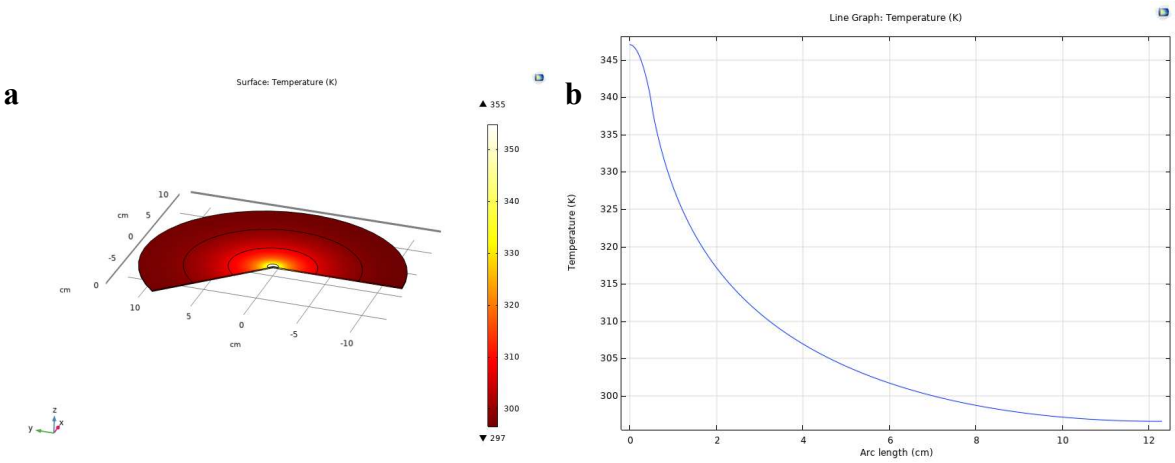

Figure 5-2: (a) Simulation results for a radius of 12.3 cm (b) Temperature gradient across surface

As observed above in Figure 5-2, the maximum temperature obtained corresponding to the cell temperature was 355 K. This number is consistent with the result obtained for the verification check in section 4.1.2 where a temperature of 355 K was also obtained, thus, confirming that the model is accurate. The temperature gradient across the radiative cooler ranges from 355 K at its center to 297 K at its edges. These results differ from the initial feasibility results obtained using the Stefan-Boltzmann equation. This was expected as the latter assumes a uniform temperature across the surface while in practical cases, there exist a temperature gradient across the cooling structure with the areas closest to the heat source being hotter.

Hence, the next step used for the analysis involved running simulations with varying structure radii to find the radius that results in a cell temperature of 300 K for the same boundary conditions. Figure 5-3 shows the temperature gradient obtained for multiple radius ranging from 12.3 cm to 21.3 cm.

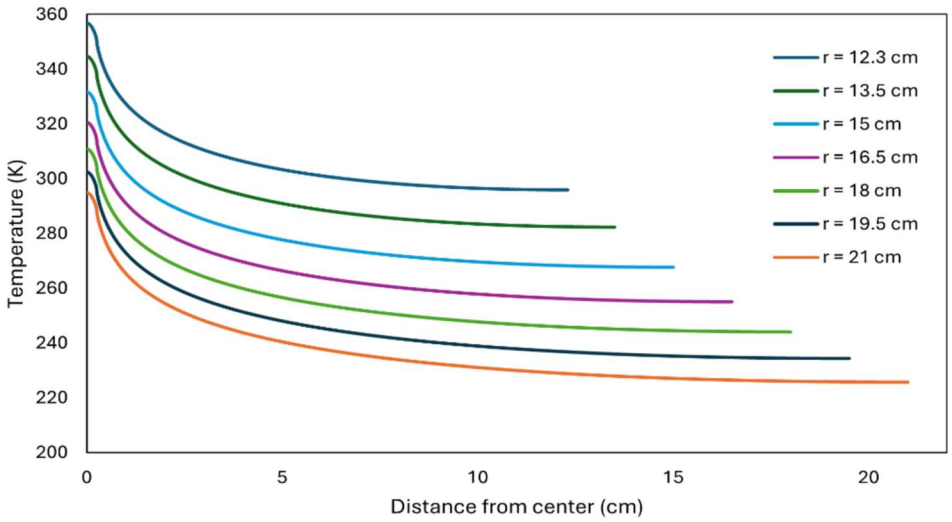

Figure 5-3: Temperature gradient across cooler for different radii at uniform thickness

The results in Figure 5-3 show that as the cooler increases in size its temperature steadily drops. This is caused by the increase in surface area of the cooling structure which increases the amount of heat rejection through radiation. A temperature of 300 K at the center of the cooler is achieved when the radius is 19.5 cm. This structure has a volume of 199.46 cm^3 and a weight of 1.07 kg. While the volume was fairly reasonable for deployable structures, the weight of the cooler was quite heavy for a small satellite or CubeSat and further analysis was required to reduce it.

5.1.2 Impact of size changes

In order to further understand the variation in temperature gradients, the impact of size changes, namely thickness and fixed volume cases, were analyzed with the method described in Section 4.1.3. Figure 5-4 shows the results obtained using COMSOL when varying the thickness of a copper disk with a radius of 15 cm and thicknesses ranging between 0.1 mm to 2 mm and intervals of 0.1 mm. Additionally, to compare its cooling performance, the temperature change relative to the 0.1 mm case was calculated along with the radiative surface area to find the relative temperature change per surface area plotted in Figure 5-4.

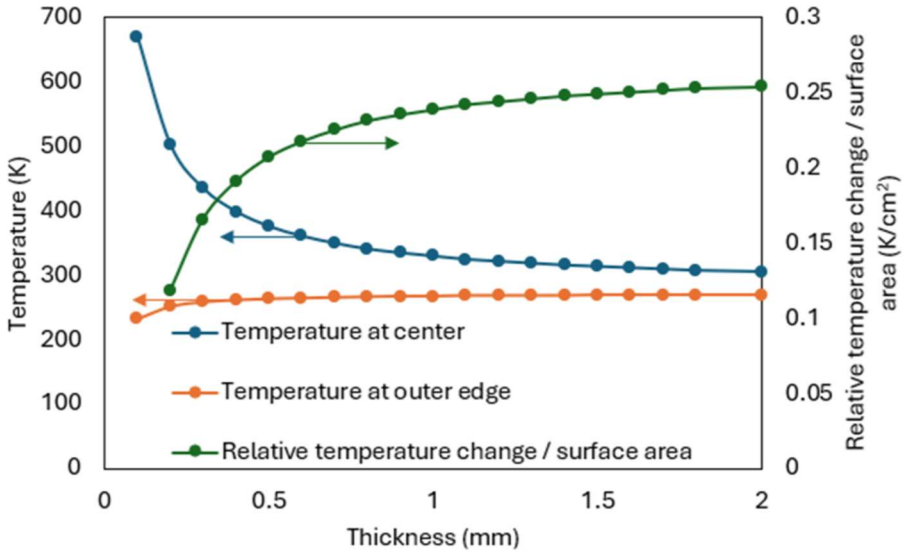

Figure 5-4: Simulation results for the impact of thicknesses of a copper radiative cooler with a radius of 15 cm on cell temperature

Figure 5-4 shows the temperature at the center and outer edge of the radiative cooler as a function of its thickness. The temperature measurements are taken from the top side of the radiative cooler. It can be observed that when the thickness of the radiative cooler is below 0.5 mm, every 0.1 mm increase in thickness has a significant impact on the temperature at the center of the structure, which corresponds to the temperature of the cell. The relative temperature change per surface area shows larger increases for thinner cases before becoming almost constant at larger thicknesses. This indicates that increasing the thickness of the radiative cooler has diminishing returns in terms of cooling performance improvements as the thickness is further increased. Once the thickness becomes larger than 1 mm, the gains in cooling become minimal and are largely attributed to the increase in surface area at the outer edges caused by the thickness increase. This is an important point when considering the design of the radiative cooler because it indicates there is a thickness range that minimizes the cooler weight with very little compromise in cooling performance.

It can also be observed from Figure 5-4 that as the thickness increases, the temperature gradient from the center to the edge of the cooler decreases, with the temperature at the center and outer edge slowly converging towards each other indicating better lateral heat distribution across the top surface. This can be confirmed using Equation 12 comparing temperatures at the top and bottom surfaces of the cooler.

$$R_{cond} = \frac{T_{top} - T_{bottom}}{q} = \frac{L}{kA} \qquad \text{Equation 12}$$

As the length, L, increases the thermal resistance increases as well. This causes a steeper temperature gradient between the top and bottom surface of the cooler indicating better heat dispersion by the radiative cooler across itself implying a more even temperature gradient across its surface from the center to the edges.

The next part of the analysis involved using a fixed amount of material or a fixed volume case. A circular disc with radius 15 cm and thickness of 1 mm was used as the base case for the volume with a value of 70.7 cm^3 and the radius was varied from 3 cm to 30 cm. Figure 5-5 displays the results obtained for the temperatures at the center of the cooler and outer edge. Measurements are from the top surface of the cooler.

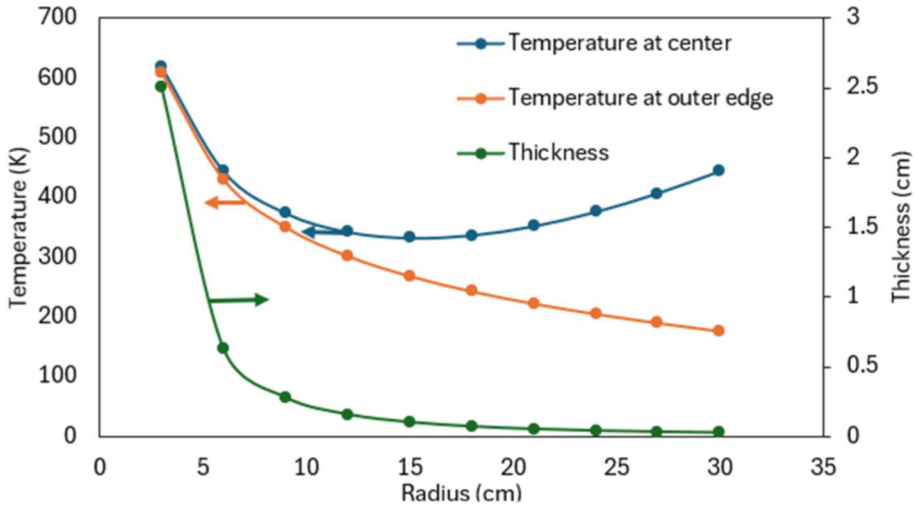

Figure 5-5: Fixed volume analysis with a constant volume of 70.7 cm^3

In Figure 5-5, it can be observed that initially as the radius increases, the temperature at the center decreases. However, as it gets past 18 cm the temperature started to climb back up indicating worse cooling performance. This indicates that there is an optimal point where the cooling performance is maximized when the volume is held constant. This is related to the results obtained in Figure 5-4 since as the radius gets bigger, the structure gets thinner causing worse thermal performance and an increase in temperature at the center. The outer edge temperature keeps getting lower with an increase in radius. This is caused by the increase in distance from the heat source which leads to lower temperature.

5.1.3 Impact of materials

The next step of the analysis discussed in method Section 4.1.4 involved looking at the impact of different materials. Figure 5-7 below shows the results for a material sweep involving aluminum, copper, and carbon-fibre composite across the three sections of a 30 cm wide and 1 mm thick circular cooler with the same boundary conditions as previous simulations. The results obtained are shown in Figure 5-6.

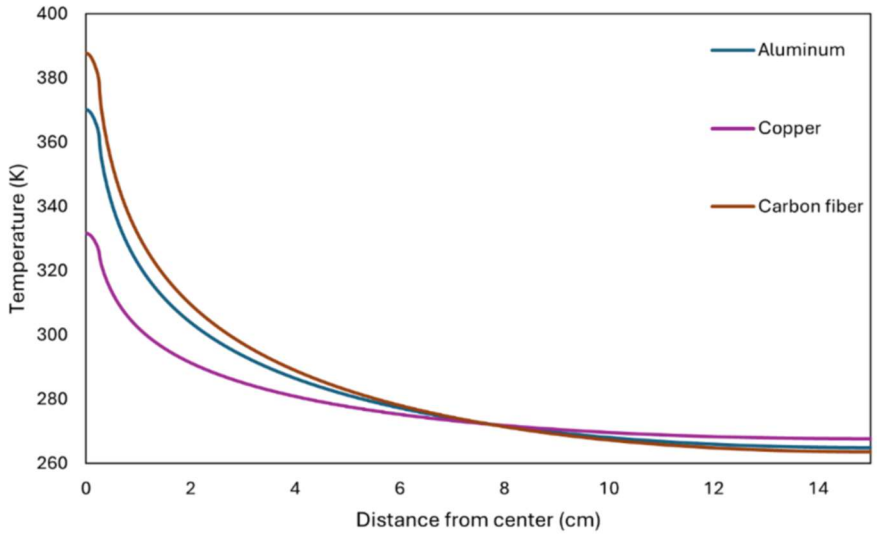

Figure 5-6: Comparison of coolers made of different materials

The expectation was that the material with the highest thermal conductivity, which here is copper, would provide the best cooling performance and hence, the lowest cell temperature. The results obtained in Figure 5-6 met this expectation with the copper cooler having a temperature of 331 K at its center, while center of the aluminum cooler reached 370 K and the carbon fiber cooler performed the worse as the temperature at its center reached 387 K.

5.1.4 Panel configurations

The next set of simulations involved using different material configurations namely horizontally, vertically, and diagonally to compare them and determine the best choice. The results for the horizontal simulations are shown in Figure 5-7 below.

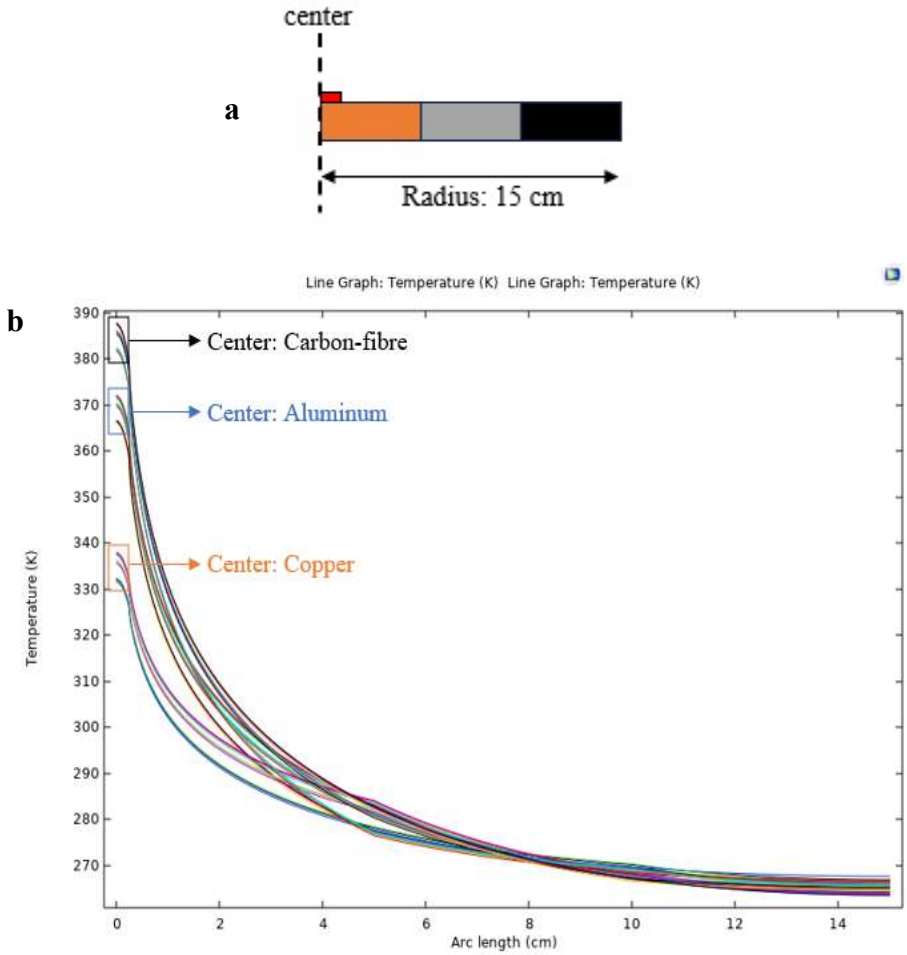

Figure 5-7: (a) Cross-section showing material locations (b) Results of horizontal material sweep

Figure 5-7 (a) above shows a cross-section of the cooler with 3 different sections in the horizontal direction. A material sweep is conducted with these three sections with the material orders varied. It can be observed from Figure 5-7 (b) that there are three distinct temperature range clusters recorded at the center of the radiative cooler. The temperature range between 331 K and 337 K shows the results for configurations wherein copper is in the middle, the temperature range between 365 K and 372 K corresponds to aluminum in the middle while the temperature range between 381 K and 387 K represents the result when carbon-fibre composite is in the middle. This proves that having a material with the highest thermal conductivity at the center where the heat source is located provides the best thermal performance. This was expected as the highest thermal conductivity allows for the most heat to dissipate away from the heat source in the shortest amount of time. Figure 5-8 below provides a comparison of the temperatures at the center of the coolers taken from the results shown in Figure 5-7.

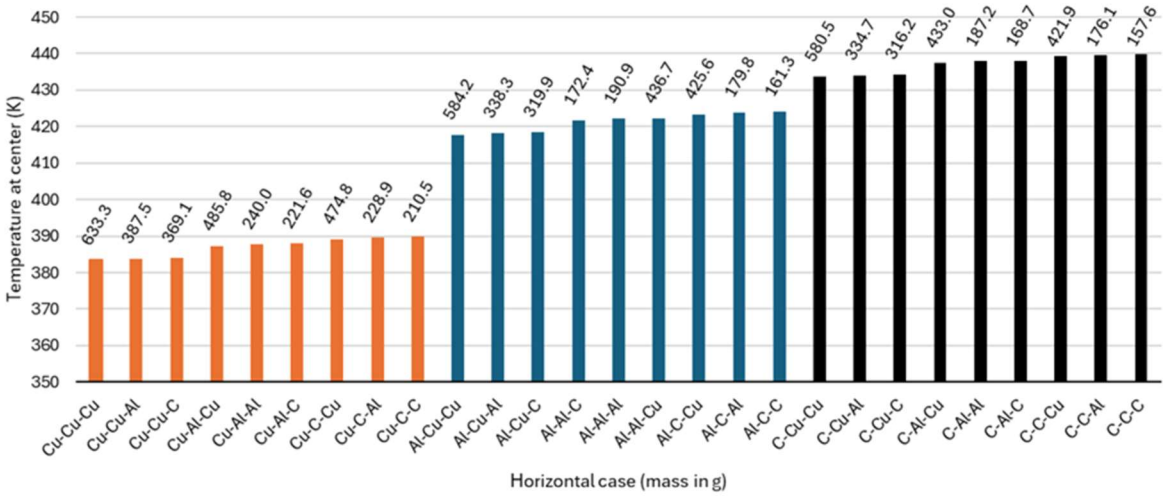

Figure 5-8: Temperature at center comparison for horizontal cases

Figure 5-8 above shows that the cooler made of all copper panels provides the best cooling performance while the one made from all carbon fibre is the worst. Carbon fibre has the lowest thermal conductivity of the three and this explains its performance. The copper-Aluminum-carbon fibre ordered cooler leads to a cell temperature only 3 K higher that the copper cooler and is the best performing case involving all 3 materials. The results indicate that using panels with decreasing conductivities as we move away from the center can cause only a small reduction in cooling performance while allowing for a reduction in cooler weight.

In order to examine the impact of using a sandwich structure with multiple material layers, further simulations were carried out. The simulation set involved the use of a vertical cross section, as shown in Figure 5-9 (a), using the combinations of the same three materials. The results are shown below.

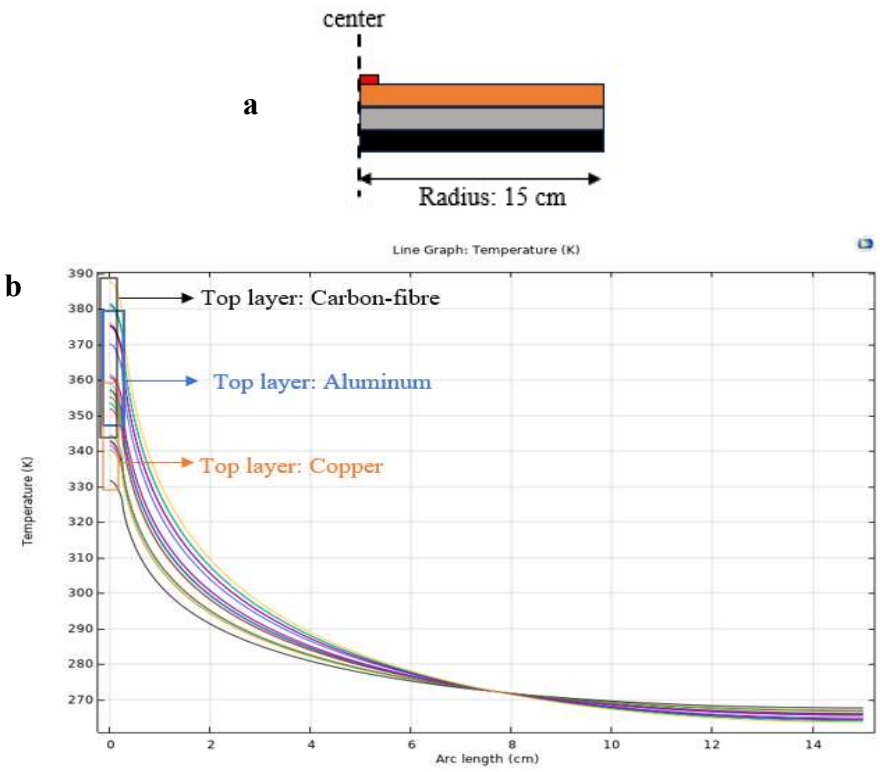

Figure 5-9: (a) Illustration of vertical cross-section (b) results for vertical case

In Figure 5-9 (b), it can be observed that the temperature profiles overlap each other. For the cases wherein the top layer was made with copper, the temperature at the center of the cooler ranged from 331 K to 359 K. When the top layer was aluminum and carbon the temperature at the center of the radiative cooler ranged from 341 K to 380 K and from 343 K to 387 K, respectively. These results further confirm that having copper directly in contact with the cell would result in the best cooling performance. However, there is a larger variation in temperature compared to the horizontal case. Figure 5-10 below shows a further breakdown of these results for all cases.

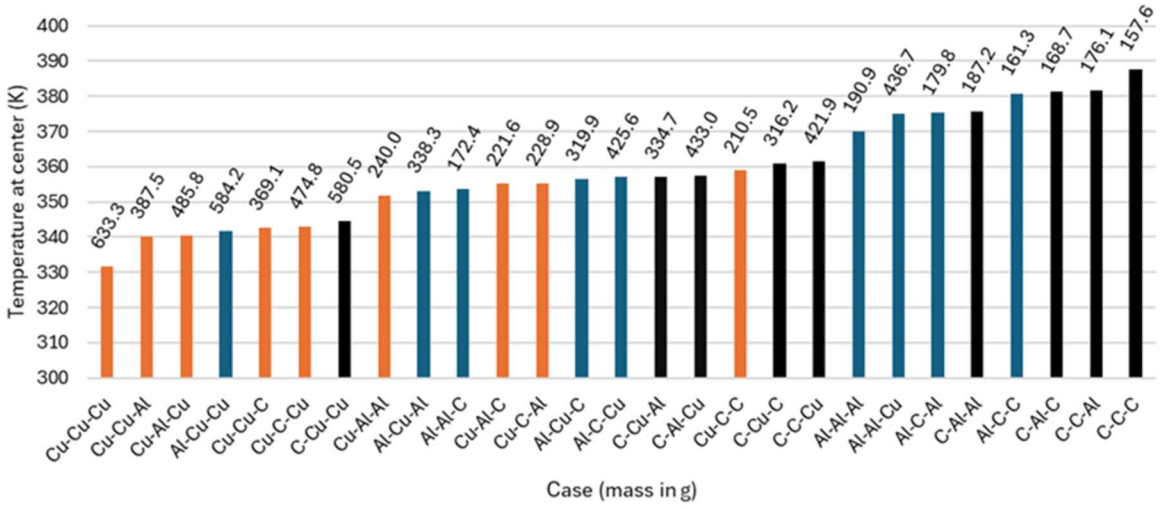

Figure 5-10: Temperature at center comparison for vertical cases

Figure 5-10 above shows that the presence of copper at the top layer or middle layer produces the best results except for the cases where carbon-fibre is present in the top or middle layers. The best case where all three materials are used, Cu-Al-C, resulted in a temperature of 354 K at the center which is a 23 K increase compared to the all-copper best case. This is significantly higher than the 3 K increase shown in the horizontal case.

The order of the materials can be further examined by considering diagonal material combinations as shown in the cross-section below in Figure 5-11 (a).

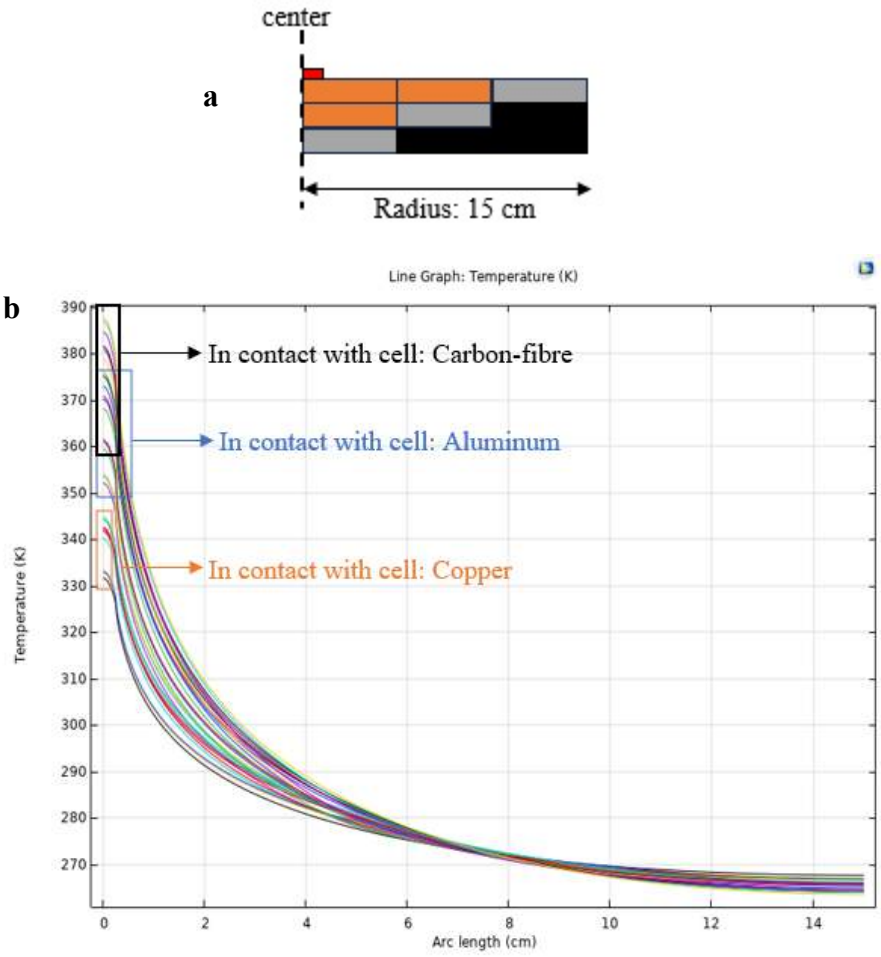

Figure 5-11: (a) Illustration of diagonal cross-section (b) Results for diagonal cases

Figure 5-11 (b) displays the three clusters with the cases where copper is in contact with the cell being the best performing one. The aluminum and carbon fiber cases overlap with each other. The copper cluster ranged between 331 K and 343 K, the aluminum cases ranged from 351 K and 376 K while the carbon fibre cases ranged from 359 K to 387 K. This further solidifies the previous findings where copper in contact with the cell provides the best performance for all configurations. Figure 5-12 below shows a deeper dive into the data with the results from all cases displayed.

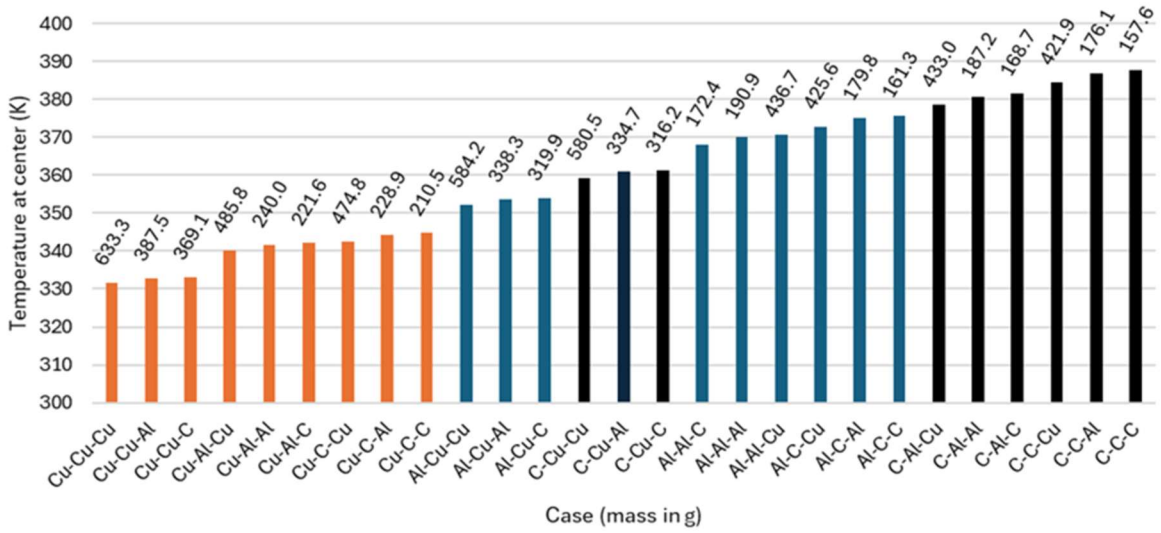

Figure 5-12: Temperature at center comparison for diagonal cases

As shown above in Figure 5-12, the cases with copper in contact with the cell and with copper as the second material in the middle layer are the best performing ones followed by the cases with aluminum in contact with the cell. This is consistent with the thermal conductivity of the materials as the cases with highest conductivity material in contact with the cell produced the best cooling performance. The best case involving all three materials resulted in a temperature of 341 K which was better than the vertical case but worse compared to the horizontal case. This also represented an increase of 10 K in temperature compared to the best case of 331 K.

From the comparison of these three configurations, it is clear that the horizontal one produced the best results in terms of temperature. However, another factor to consider is the weight of the cooler. In order to compare the configurations in the horizontal case, the following metric is used:

$$\Delta T_w = \frac{T_{baseline} - T_{cell}}{W} \qquad \text{Equation 26}$$

Where ΔT_w represent the relative temperature change with respect to weight, T_{cell} is the cell temperature, $T_{baseline}$ is a chosen temperature baseline, and W is weight.

An objective is to maximize ΔTw because the main goal is to minimize the temperature of the cell while minimizing weight. The baseline case chosen was the all carbon-fiber case which produced the highest cell temperature out of all cases studied. The difference between this baseline and the recorded cell temperature shows the relative temperature drop by the other cooler configurations examined. Hence, a higher temperature drop from the baseline, and a lower weight would lead to a higher the relative temperature change to weight ratio which represent better

cooling performance by weight. The chart below in Figure 5-13 shows a comparison the obtained results:

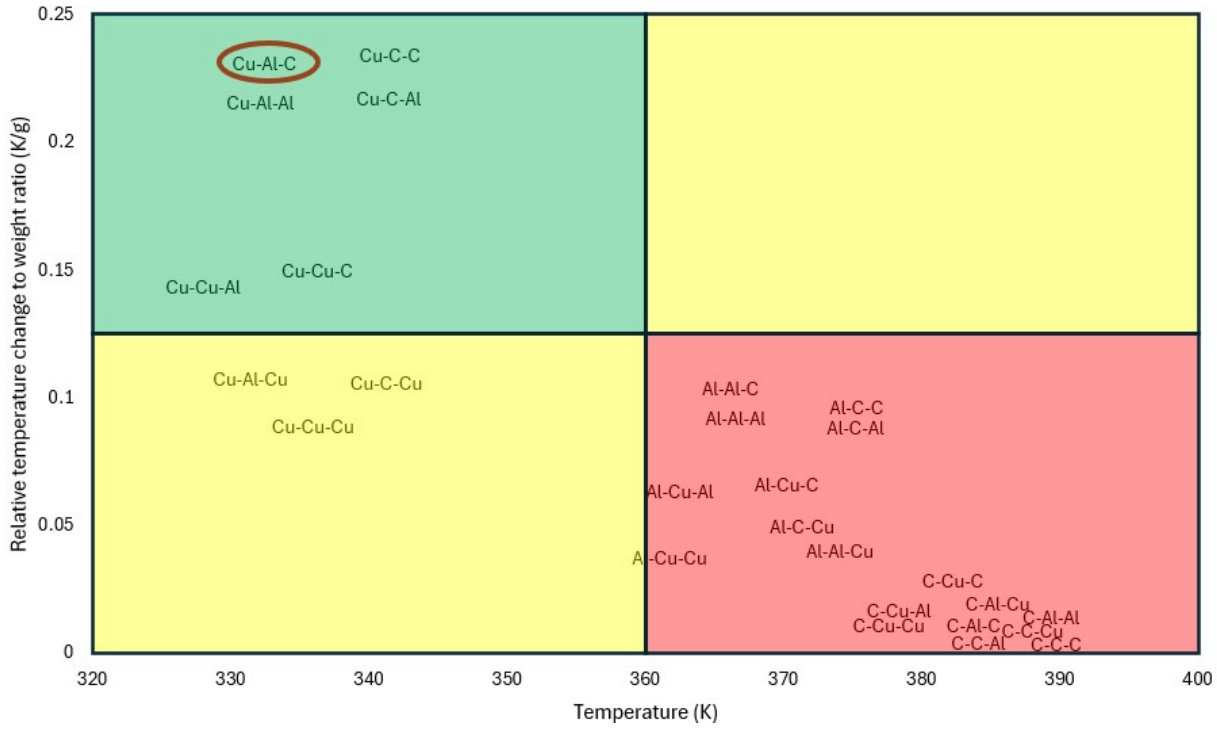

Figure 5-13: Comparison chart of horizontal cases

The chart above, in Figure 5-13, considers the relative temperature change to weight ratio against temperature. The top left quadrant, colored green, represents the best performing coolers with the lowest temperature and highest relative temperature change to weight ratio while the bottom right, colored in red, represents the worst performing ones. The yellow-colored quadrants consist of average performing ones. It can be clearly seen that Cu-Al-C and Cu-C-C have the highest ratios valued at 0.231 and 0.234 respectively. However, Cu-Al-C had a temperature of 336.1 K, lower than the 337.8 K recorded for Cu-C-C. Hence, the panel configuration consisting of Cu-Al-C aligned horizontally to each other ended up being the chosen one for further analysis.

5.2 Model validation

Using the result obtained from the panel configurations analysis, the COMSOL modeling and experimental validation process were the next steps.

5.2.1 Vacuum chamber experiment

The experiments were carried out in the vacuum chamber setup at a vacuum level of 10 mTorr for the 0.5 mm thick radiative coolers listed in Table 5-1.

Table 5-1: Description of experimental cases

Case number	Type of radiative cooler
Case 1	24 cm x 24 cm black-painted Cu-Al (12 cm x 12 cm Cu in the middle)
Case 2	24 cm x 24 cm unpainted Cu-Al (12 cm x 12 cm Cu in the middle)
Case 3	24 cm x 24 cm unpainted Al-Cu (12 cm x 12 cm Al in the middle)
Case 4	3.6 cm x 2 cm Cu piece
Case 5	3.6 cm x 2 cm Al piece

The radiative cooler chosen for analysis was only made of copper and aluminum to minimize the number of connections between panels and reduce experimental errors. Details about the cooler used and the experimental setup were expanded upon in method Section 4.2 while the experimental details were discussed in method Section 4.3.3. The experiments were carried out three times each with the PTC heating element as the heat source placed at the center of the cooler. The voltage applied to the PTC element was incrementally increased by 1 V over a range of 1 – 12 V. The temperatures were allowed to reached steady state and measured at each interval across the cooler and for the heating element. The resistance of the PTC heating element was calculated using current and voltage values recorded.

The average results from the three trials were calculated along with their corresponding standard deviation. These values were plotted as shown in Figure 5-14 below including the error bars showing the standard deviation in values.

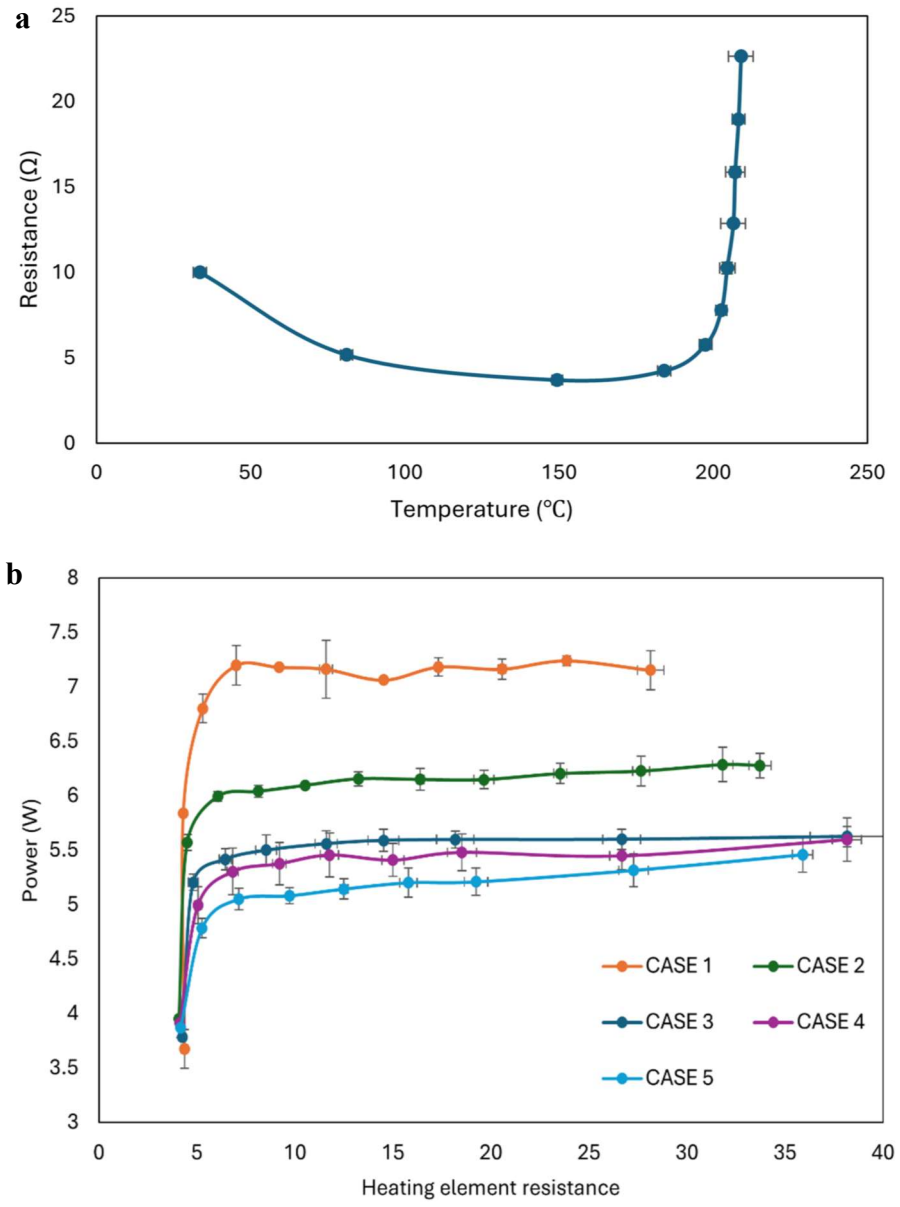

Figure 5-14: Experimental results for (a) PTC heating element tests (b) various radiative coolers

Figure 5-14 (a) shows the change in the PTC heating element resistance as the temperature rises. Due to its characteristics, despite the cooling impact of the radiative cooler, its temperature reaches the same value before its resistance rises. The element was rated for 220 °C, however, the highest measured temperature was 210 °C. The discrepancy could be explained by the uneven distribution of heat throughout the heating element and the limited areas where the thermocouple could reach inside of it. It was also observed during the experiments carried out that the thermocouple had a cooling effect on the heating element when in direct contact with certain areas resulting in higher power values. Hence, the location chosen was on the walls of the heating element slightly away from the main heat source inside of it. The results were as expected as the

typical behaviour of a PTC ceramic element can be clearly observed with a large spike in resistance close to the rated temperature.

Figure 5-14 (b) shows the results obtained. In order to find the differences in cooling power, the power input and the resistance of the heating element were plotted. The large increase in resistance occurs when the peak temperature of the heating element is reached. It can be observed that the Cu-Al with black paint coating required the highest amount of power to reach this increase in resistance and hence, maximum temperature. This is followed by uncoated Cu-Al, Al-Cu, and two small pieces of Cu and Al slightly bigger than the emitter. The results are as expected since, the black paint increases the emissivity of the structure and hence, its cooling power. The black painted Cu-Al required around 1 W extra power compared to the Al piece to reach the same temperature indicating a higher cooling power by around 1 W. By using the small Al piece as a baseline, this implies that that Al-Cu structure has a relative cooling power of 0.43 W, the Cu-Al structure is around 1 W and the painted Cu-Al is around 2 W.

5.2.2 Error analysis

In order to verify the accuracy of these results, an error analysis needs to be carried out. Table 5-2 shows the average power values obtained from the three trials as well as the standard deviation of these three values.

Table 5-2: PTC heating element experimental results

Case	Power input – heating element	Standard deviation – power input	Experimental cooling power
Black painted Cu-Al	7.26	0.34	2.0
Cu-Al	6.20	0.08	1.0
Al-Cu	5.63	0.15	0.43
Cu	5.39	0.20	0.19
Al	5.20	0.23	BASELINE

The standard deviation values shown in Table 5-2 are relatively low implying that the experiments were repeatable and produced consistent results. The use of the power input to the heating element as a way to measure the cooling power can be verified with the results obtained for temperature across the radiative cooler and the Stefan-Boltzmann equation. The black painted Cu-Al is the one used due to its uniform emissivity. FTIR testing was carried out on a sample to obtain the absorptance value of that paint in order to find that emissivity and the result obtained is shown in Figure 5-15.

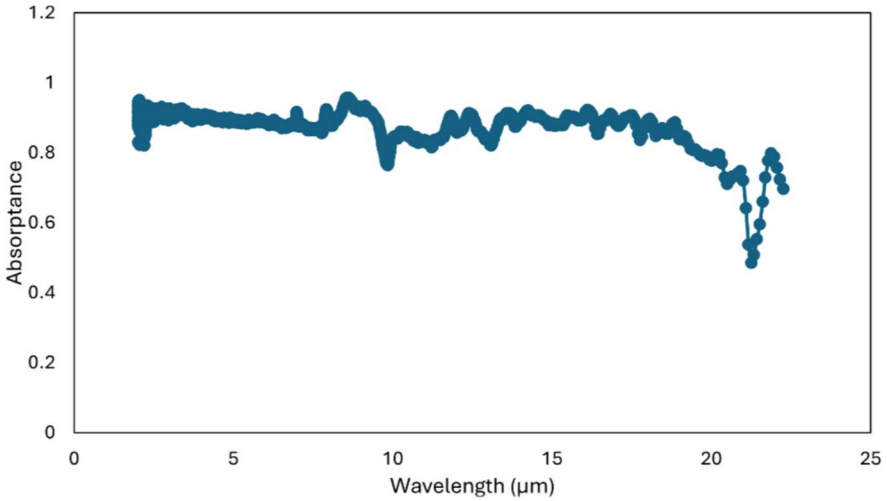

Figure 5-15: FTIR results for black ceramic paint on aluminum surface

The experimental process to obtain the absorptance values as well as the calculation required to find the emissivity of the black tape was outlined in Section 4.2.4. The tests carried out to obtain the results in Figure 5-15 were repeated three times and showed an acceptable average standard deviation of 0.00465. The emissivity of the black ceramic paint was calculated to be 0.87 for the mid-IR range considered and shown in Figure 5-15. The calculation was done using the average values obtained from the FTIR tests and using Planck's law along with emissivity equations for calculations.

The temperature measurement locations were illustrated in Figure 4-29 previously in section 4.3.3.1. The cooler was divided into four different areas based on the thermocouple locations as shown below in Figure 5-16.

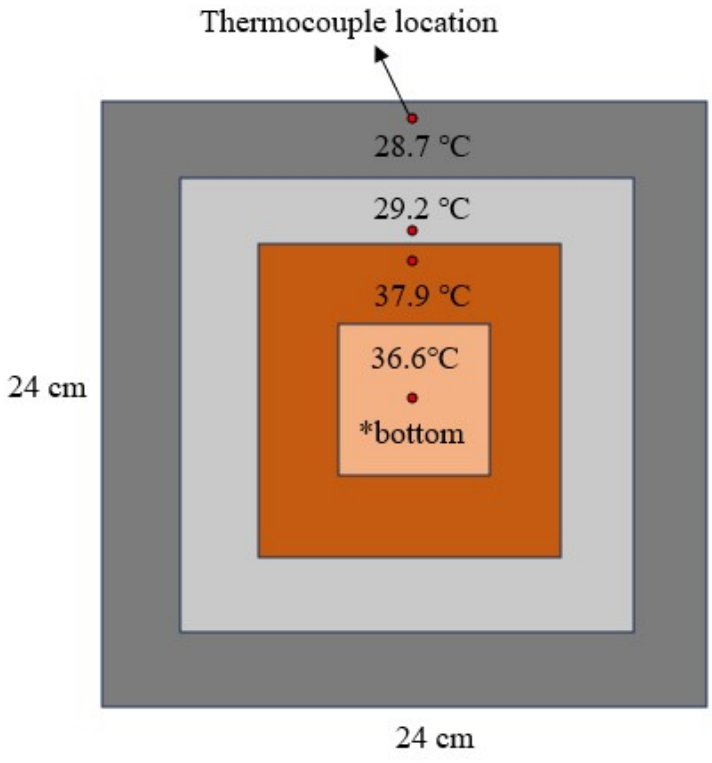

Figure 5-16: Thermocouple readings across 4 different areas

These four areas in Figure 5-16 are considered to have approximately the same temperature across them. It can be clearly observed that the temperature in the middle is lower compared to its adjacent area. This was caused by the measurement being taken at the other side of the cooler due to the presence of the PTC heating element. These temperatures along with their respective areas were used along with the emissivity value to calculate the cooling power as part of the Stefan-Boltzmann equation. It yielded a cooling power of 2.01 W which was identical to the experimental cooling power, however, a more accurate value for the central part of the cooler would have caused it to be higher.

The uncertainty associated to that value can be found using the following equation derived from the Stefan-Boltzmann equation:

$$\frac{\partial P}{P} = \sqrt{\left(\frac{\partial \varepsilon}{\varepsilon}\right)^2 + \left(\frac{\partial A}{A}\right)^2 + \left(4\frac{\partial T}{T}\right)^2} \qquad \text{Equation 27}$$

The derivatives representing the error associated with each measurement were found using literature and manufacturer data. These numbers were:

1. 1% for emissivity
   This value was based on literature from a paper titled: “Uncertainty estimation for emissivity measurements near room temperature with a Fourier transform spectrometer”

by Ishii and Ono. The error for a FTIR spectrometer with a KBr splitter was found to be 1 % for high emissivity cases and 3 % for low emissivity cases. [83]

2. 0.1 cm^2 for area
   The metal sheets were cut with a blade saw in the machine shop. The error was calculated based on its tolerance.
3. ± 1 ℃ or 0.75% for temperature
   This data was obtained from Omega, the manufacturer of the t-type thermocouple. [76]

The uncertainty for the cooling power was calculated to be ±0.110 W or around 5.5% for the 2.01 W value.

Another potential source of error is the difference in thermal contact resistance between the heating element shell with the metals being used. Since conductance is affected by surface roughness and contact pressure, as described in Section 2.1, the metal surface as well as the pressure applied when taping the heating element may not be equal leading to potential errors.

5.2.3 Simulation parameters

The accuracy of the results obtained from a simulation depends on the accuracy of its inputs. The value used for the boundary conditions and relevant parameters need to be as close to reality as possible. The black painted Cu-Al cooler tested in the vacuum chamber experiment was the chosen case simulated in COMSOL.

5.2.3.1 Emissivity values

The emissivity value needed for the black paint was already found to be 0.87 with the results shown in section 5.2.2 and FTIR results illustrated in Figure 5-15. However, this was not the sole emissivity value needed. During the experiment, the heating element placed on top of the cooler was also emitting radiative rays. The emissivity of the top surface of the ceramic pieces attached to the heating element, as shown in Figure 5-14 (a), was also found through the same method with the results shown in Figure 5-17.

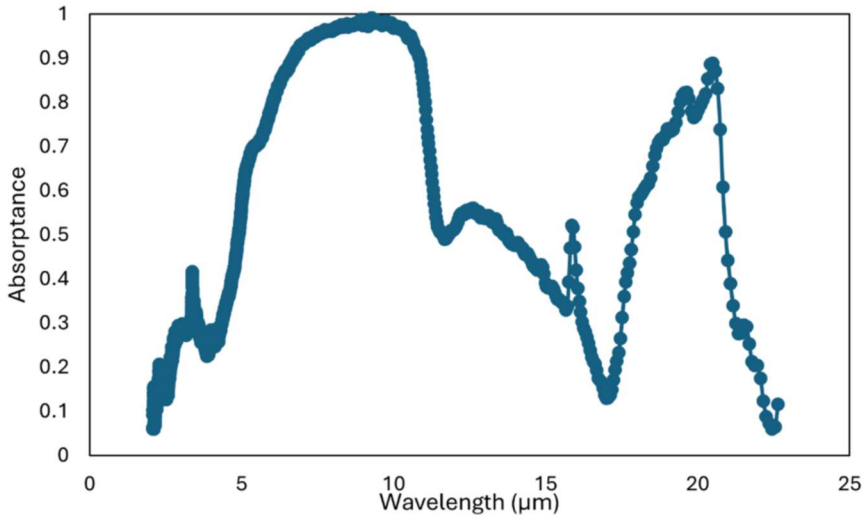

Figure 5-17: FTIR results for ceramic glued to heating element

Based on the results from Figure 5-17, the standard deviation for the FTIR tests was calculated to be an acceptable value of 0.00506 based on three trials while the emissivity value was found to be 0.67 using emissivity equations as well as Planck's law as described in section 4.2.4.

5.2.3.2 Conductance

The conductance value between the heating element and copper was found experimentally following the process described in section 4.3.3.2. A small copper piece measuring 3.6 cm to 2 cm, roughly the same size as the PTC heating element, was used. The two were attached together using a small amount of Kapton tape to ensure they remain in contact during the experiment. Voltages ranging from 4 V to 14 V with intervals of 2 V along with a measurement with 5 V were applied to the heating element. Steady state was reached at each voltage before taking measurements. The average results obtained from three trials for the temperatures of the copper sample used and the heating element are shown in Figure 5-18 below. Error bars are included showing the standard deviation calculated for the three trials.

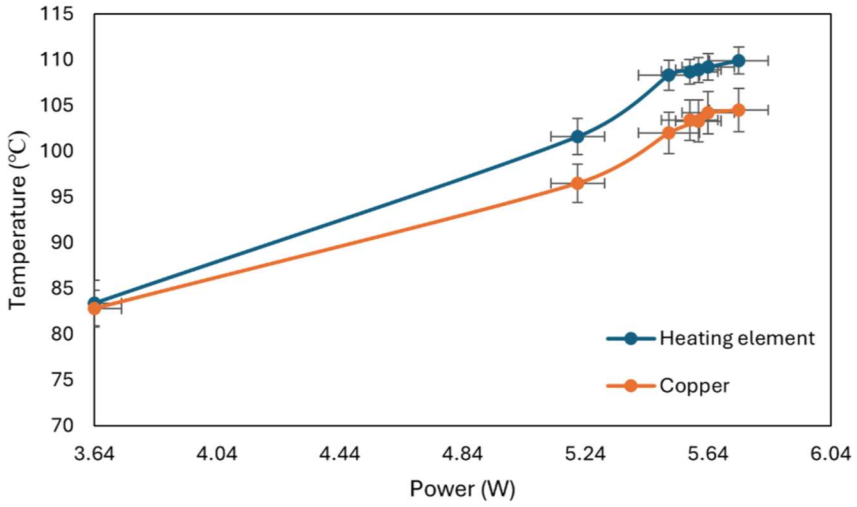

Figure 5-18: Copper and heating element conductance test

The results obtained above in Figure 5-18 were reasonably consistent across three trials. The temperature values for the heating element had an average standard deviation of 1.67 °C while those for copper deviated by an average of 2.22 °C. The temperature difference, highest power input, and area were used to obtain a conductance value of 1336 $W/m^2 \cdot K$ with a standard deviation of 235 $W/m^2 \cdot K$.

Similarly, the conductance between copper and the aluminum panels were measured with the process outline in section 4.3.3.2. The testing was conducted three times with temperatures at two different panel intersections measured each time. A conductance value of 8944 $W/m^2 \cdot K$ was obtained with a standard deviation of 1921 $W/m^2 \cdot K$. This value was consistent with literature results shown in Section 2.1 and specifically Figure 2-3. The error was relatively high due to

varying contact pressure, surface roughness, and contact area between panels depending on where measurements were taken.

5.2.3.3 Power losses

The COMSOL simulation required an accurate value for the heating element power input since this represented the heat flux applied. The supplied power value was obtained from the power supply, however, a correction had to be done for losses in wires. Figure 5-19 shows results obtained following the process described in Section 4.3.2.4.

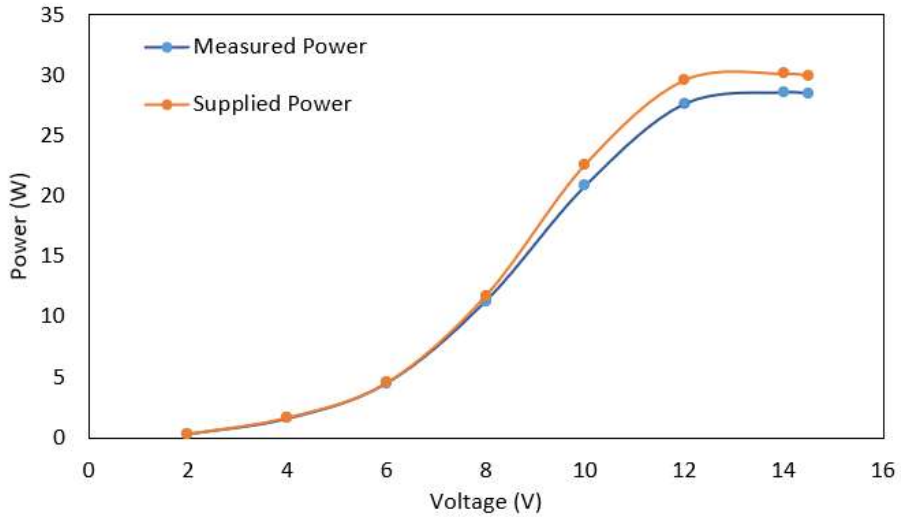

Figure 5-19: Power results using power supply and measurements inside vacuum chamber

Figure 5-19 shows a small loss of power as the voltage supplied exceeds 10 V. This loss is roughly the same in all the cases considered above since the same voltage range and wires were used in all cases. A 5 % correction was applied to the power value of 7.26 W found using the power supply reading to account for this loss.

5.2.4 Result comparison

The simulation was carried out on COMSOL using the parameters outlined in section 4.3.3.3 and Table 4-8. The results comparison between experimental and simulation outcomes are shown in Figure 5-20 below.

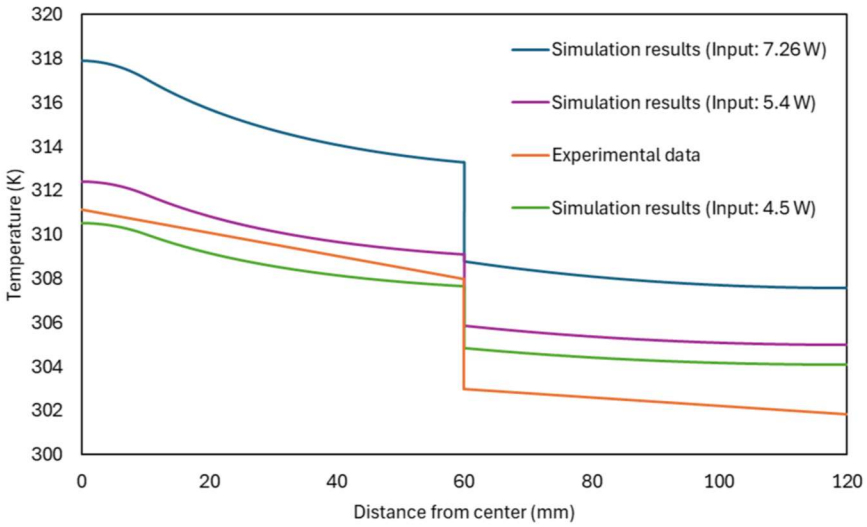

Figure 5-20: Comparison of temperature gradient across cooler for experimental and simulation results

Three different power inputs were used to acquire the simulation results reported in Figure 5-20. The output power calculated from the power supply values was 7.26 W. A correction was done to the power input value used for conductance calculations to account for wire losses and emissive losses through the emitter. After the correction the power input value was determined to be 5.4 W, which was closer to the real heat flux applied in the experiment and transferred from the heating element to the radiative cooler. Finally, through an iterative process, 4.5 W was found to be the power value closest to the experimental results recorded. The experimental results and the simulation results obtained for a power of 5.4 W were reasonably close to each other with a temperature difference at the center of around 1 K.

The results in Figure 5-20 show that the experimental results were close to the corrected power value, however, the simulation results were slightly overestimated. This was due to the conduction losses from the cooler to the stand. Experimental data confirmed that the top of the stand in contact with the cooler experienced an average temperature increase of 2 ℃. Using the 4.5 W power value closest to the experimental results, the conductance losses, to the ceramic posts and the ellipsoidal cavity, were approximately 0.9 W. An estimate of the conductance losses was theoretically calculated using Fourier's law along with the contact area between the cooler and the stand, the conductivity value of alumina and the temperature change recorded at steady state. This value was found to be 0.79 W which roughly aligns with the 0.9 W estimated from simulation, thus, confirming that the error was due to experimental losses through conduction not reflected in the simulation.

From Figure 5-20, a divergence can be observed between the simulated and experimental values with the error increasing with increasing distance away from the center. This discrepancy is due to the procedure used to determine steady state during the experiment where a constant temperature at the center of the cooler was taken into consideration. That choice implied that the edges were not at steady state when the temperatures were recorded as heat transfer was still occurring towards the outermost edge at a much slower and less observable rate. If the experiment

was run over a significantly longer period of time, this discrepancy at the edges would have been mitigated.

5.3 Parametric study

In this section, a parametric study was conducted as per the process described in section 4.3.4. Results for multiple cases are analyzed.

5.3.1 Constrained case

In the constrained case, the Cu-Al cooler is limited in size by the vacuum chamber. The cooler has a set outer length and width of 24 cm. The length and width of the copper middle part is varied between 2 cm to 22 cm using 4 cm intervals. All combinations are considered and the all-copper case is included in the parametric study as well. Further refinement was carried out by considering the 18 to 24 cm range at 1 cm intervals. The results obtained are shown below in Figure 5-21.

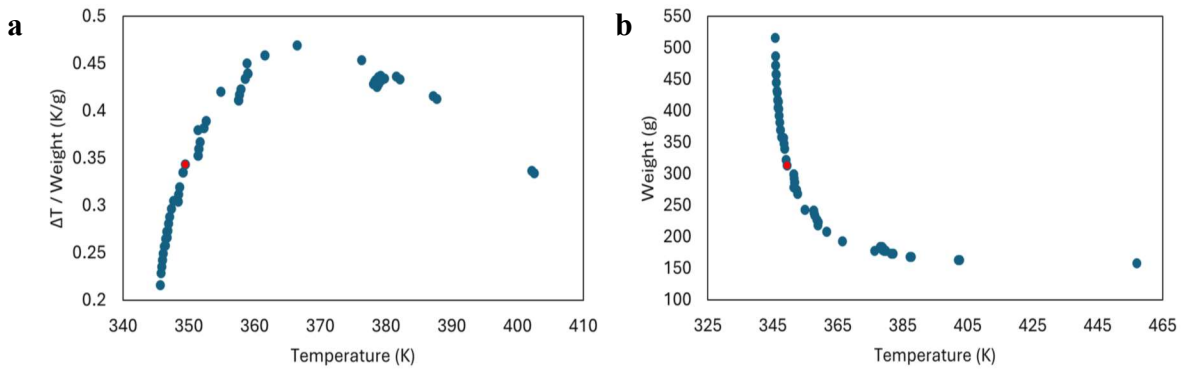

Figure 5-21: Constrained case results (a) temperature drop/weight vs temperature (b) weight vs temperature

The results above, in Figure 5-21, show patterns in both graphs. When taking into consideration, the relative temperature drop normalized to weight relative to cell temperature, it can be observed that there is a peak obtained which represents the best cooling performance with minimal cooler weight. However, this peak happens at a temperature of 366 K while the lowest recorded temperature for the all-copper case was 346 K representing a sizeable difference in temperature of the PV cell. Further information was required to choose the most appropriate cooler dimensions. The weight vs temperature shows a comparison between the weight of the cooler and how the cell temperature is impacted. It can be observed that as the temperature is lowered, an increasingly higher weight increase is needed to keep lowering the temperature. It implies that there are diminishing returns when trying to cool down the cell further. Hence, a compromise needed to be found. Using the results from Figure 5-21 (b), a maximum allowable temperature of 350 K was selected since it represented a relatively small increase of 4 K compared to the best case while also being the point where larger changes in weight were required to cool the cell further. The chosen case is colored red in Figure 5-21 with a temperature of 349.5 K and a mass

of 313 g. The copper size was 14 cm by 18 cm with the longer side aligned with the longer side of the heat element representing a TPV cell. The remainder of the 24 cm by 24 cm cooler was made of aluminum. Based on the temperature results and Stefan-Boltzmann's law, the chosen cooler had a cooling power of 10 W at a surrounding temperature of 300 K.

5.3.2 Unconstrained cases

The same process was followed for different cases without the restriction of the vacuum chamber used for lab testing.

5.3.2.1 At room temperature

In this case, the same parameters were used as the constrained case in Section 5.3.1 and dimensions of the cooler were examined using a range of 10 cm to 50 cm at 5 cm intervals. These dimensions were varied independently for both the length and the width of the cooler with the thickness remaining at 1 mm. This allowed the study of cases going beyond the 24 cm by 24 cm size limitation caused the vacuum chamber. The results are shown in Figure 5-22.

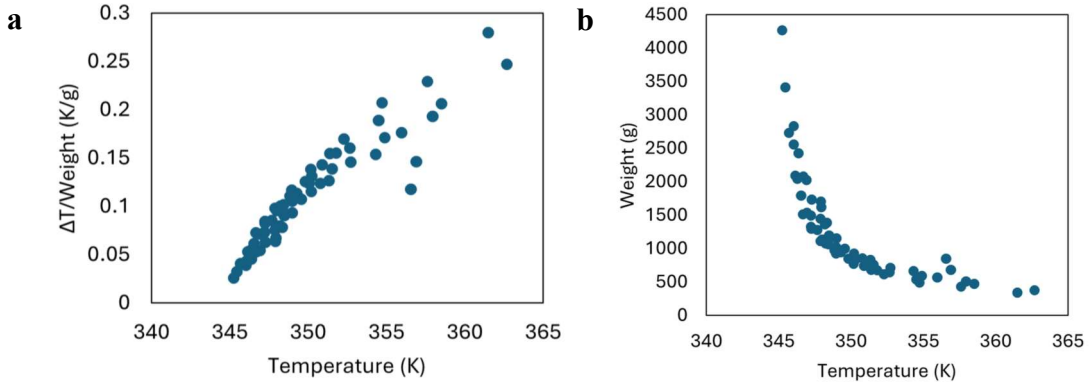

Figure 5-22: Results for unconstrained case at room temperature (a) temperature drop/weight vs temperature (b) weight vs temperature

In Figure 5-22, it can be observed that even as the cooler gets larger, the temperature still peaks at the same 345 K as in Figure 5-21. The range used in this set of data involved larger dimensions to obtain the overall trend in the data. The coolers leading to temperatures between 345 K and 350 K were all 500 g and above while their relative temperature change to weight ratio were not as high as the constrained case which consisted of a more refined range. Based on this data, the cooler selected in Section 5.3.1 is the best overall cooler when considering both weight and cooling performance.

5.4 Performance in space

The parametric study performed considered cases at room temperature. However, since the temperature of deep space is considered to be 3 K, this can have significant impact on cooler performance.

5.4.1 Temperature change

The optimized cooler found in the parametric study was analyzed with the surrounding temperature set to 3 K instead of 298 K while keeping all parameters the same. The result obtained is shown in Figure 5-23.

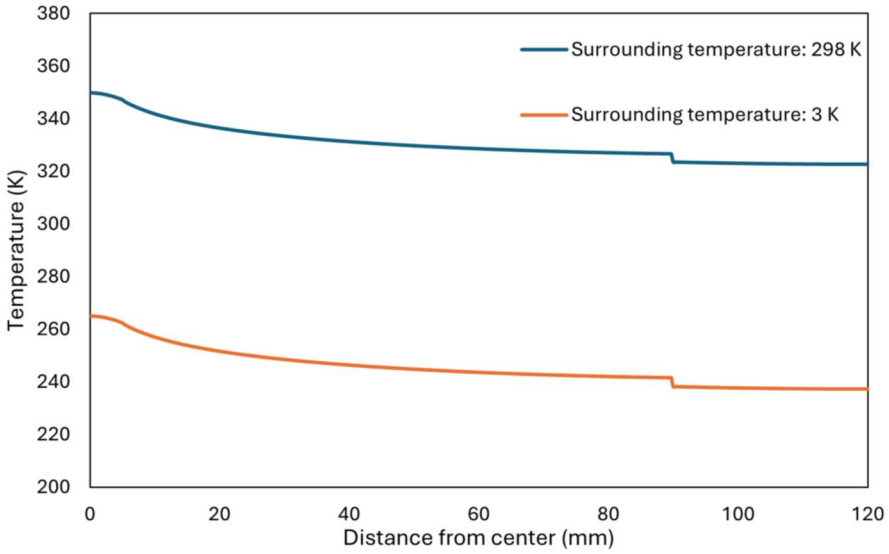

Figure 5-23: Comparison of temperature gradient across cooler surface at 298 K and 3 K

As expected, it can be clearly observed in Figure 5-23 that the temperatures recorded across the radiative cooler are significantly lower at 3 K compared to 298 K. The cooler had a size of 24 cm by 24 cm with a copper interior measuring 14 cm by 18 cm. This is due to the larger temperature gradient between the cooler and the outer surroundings which allows the cell temperature to cool down from 350 K at room temperature to 265 K at space temperature. These results also imply that at lower temperatures, radiative coolers can be smaller in size to meet cooling requirements. This does, however, ignore the impact of solar radiation and other incoming rays on the cooler.

5.4.2 Space conditions

Heat fluxes were applied to the radiative cooler to simulate the worst-case impact of solar rays, the Earth's albedo, and IR radiation emitted from Earth. A coating of AZ-93 with a solar absorptivity value of 0.15 was considered for the cooler and this was represented in the COMSOL simulation by only considering 15% of the incoming rays as being absorbed and creating these heat fluxes. The simulation was carried out at 3 K and with a power input of 20 W applied at the TPV cell similar to the room temperature cases examined. The results are compared in Figure 5-24.

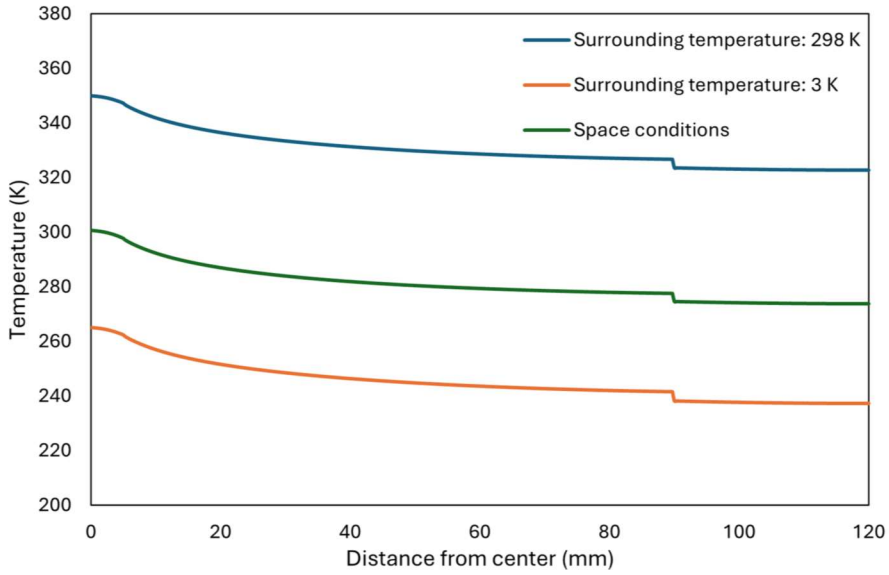

Figure 5-24: Comparison of temperature gradient across cooler surface at 298 K, 3 K and in space conditions

The temperature of the TPV cell increased from 265 K to 300 K due to the influence of the radiative rays as shown in Figure 5-24. The temperature is still significantly below the 298 K surrounding temperature case where the cell was found to reach 350 K and corresponding radiative cooler chosen as the best compromise. In the constrained case in Section 5.3.1, the radiative cooler was determined to have a cooling power of 10 W at room temperature. In this case, it can be observed that in space, the same radiative cooler is able to dissipate 20 W of heat input and maintain a roughly constant temperature since the initial cell temperature was 298 K. This indicates a cooling power of 20 W due to the lower surrounding temperature.

As discussed in Chapter 3, radiative coolers have different cooling powers depending on the operating temperature being considered with the most commonly used one being 298 K. This would imply a cooling power of 20 W for the designed radiative cooler.

It has to be noted that, in practice, the cooling impact would be even greater due to contact at the joints between the cooler and the space vessel being considered such as a CubeSat or a small satellite. There would be a greater amount of heat dissipated through conduction to the rest of the structure. However, since this is not explicitly caused by the radiative cooler and is design specific, that factor was not taken into account as part of this research. Additionally, the multi-material radiative cooler size can be enlarged through the use of origami-based folding techniques while folding in a suitable size for a small satellite.

5.5 TPV experiments

The TPV experiments were carried out using the method outlined in Section 4.4. Results were obtained with and without a spectral filter placed on top of the TPV cell. The power input was kept constant at 18.1 W for all cases and measurements done when the TPV cell temperature reached steady state. A spectral filter only allows photons from a specific wavelength range to pass through it and reflects everything outside that range. A Cu-Al cooler was made based on the dimensions obtained in Section 5.3.1 and was painted with ceramic black paint.

5.5.1 No filter case

The I-V curve acquired for the case when no filter was used is shown below in Figure 5-25.

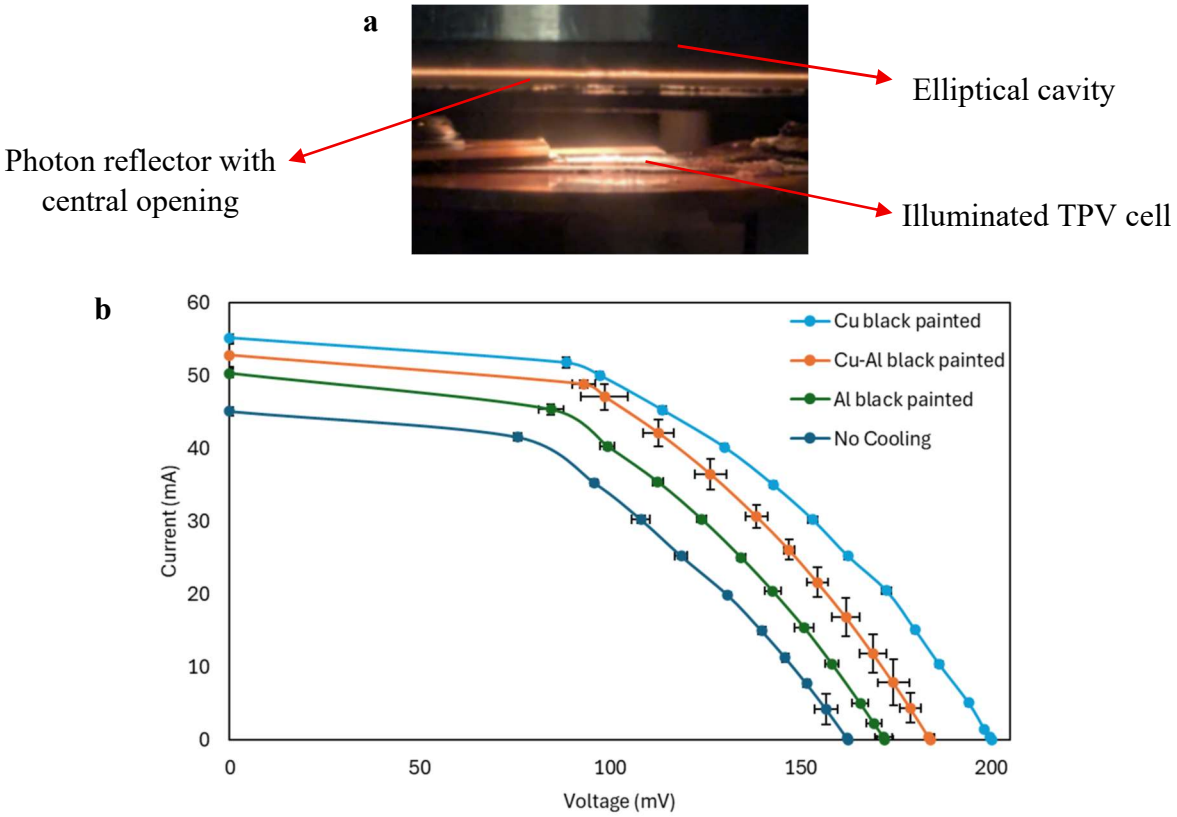

Figure 5-25: (a) Photo of cell during experiment without filter (b) IV curves for different cases

It can clearly be seen, in Figure 5-25 (b), that the black painted copper cooler had the highest power output out of all cases followed by the optimized copper-aluminum cooler, the aluminum cooler and the no cooling case in that order. The experiment produced consistent results in all three runs for each case with an average standard deviation 1.5 mA for current and 2.3 mV for voltage results. The measurement error due to wires was found to be 5% and the multimeter used had an error of 1%. These values were used to correct the standard deviation to create the error bars used in Figure 5-25 (b). The power difference can be confirmed by the maximum power point (MPP) values calculated for each case and shown in Figure 5-26 based on the average value of current and voltage.

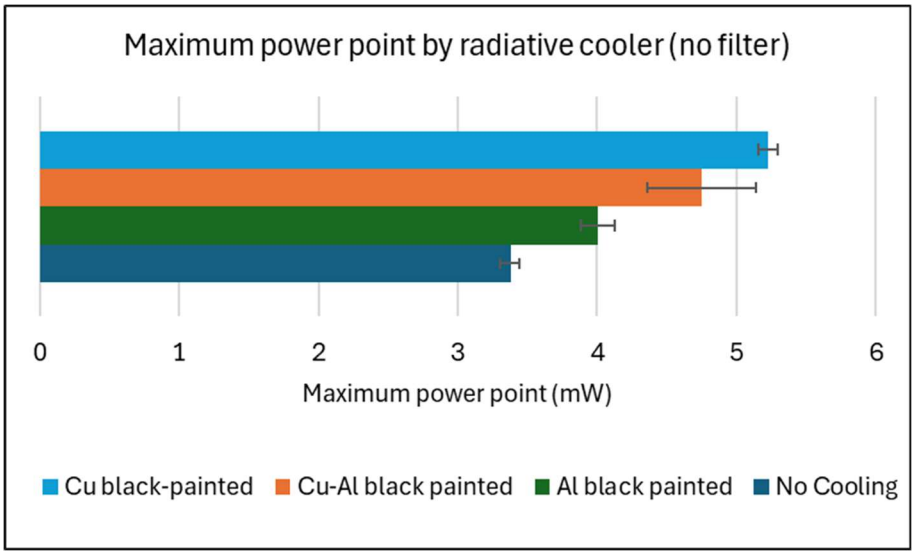

Figure 5-26: Maximum power point calculated for no filter cases

It can be clearly observed, in Figure 5-26, that the black-painted copper had the highest MPP at 5.2 mW followed by Cu-Al, Al and the no cooling case. The error bars were based on the upper bound and lower bound MPP values found using results from the three trials with a correction applied for wire losses and multimeter errors. This confirms the order of the best performing coolers with better cooling leading to higher power output. These trends were as expected based on cooler performance previously observed.

5.5.2 Filter case

The results obtained for measurements wherein an optical filter was used are shown in Figure 5-27 below.

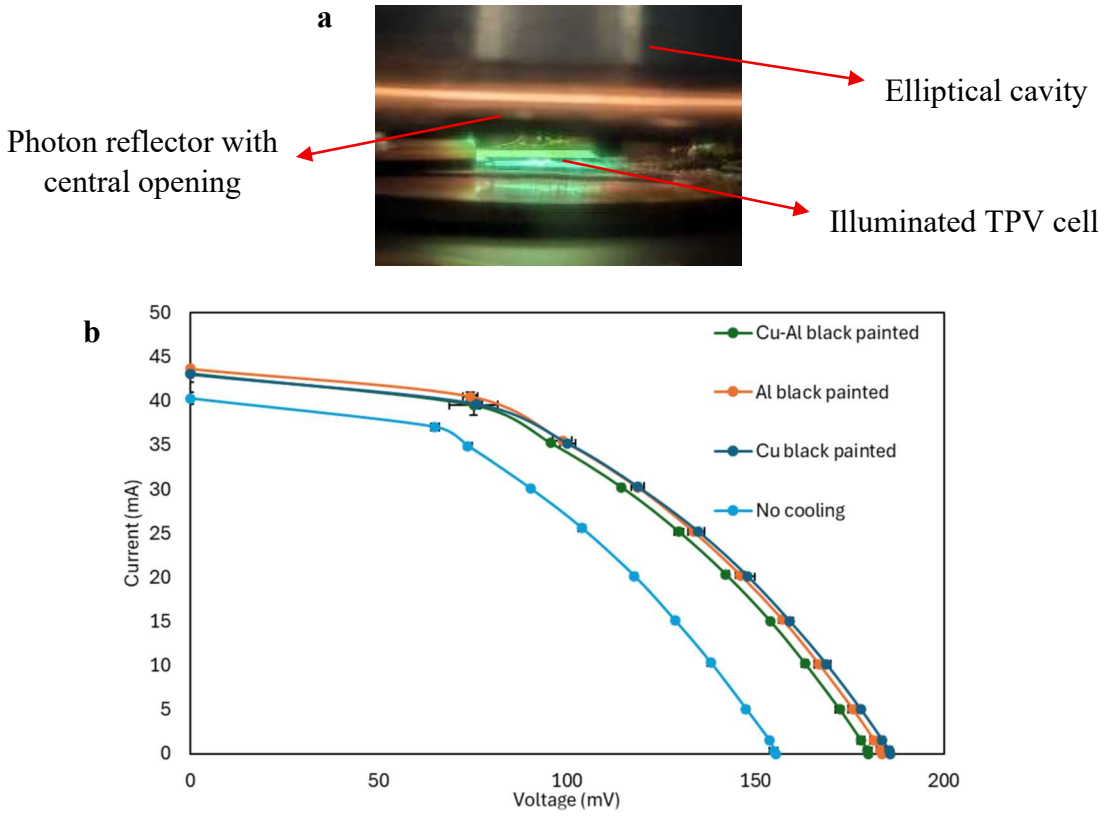

Figure 5-27: (a) Photo of cell during experiment with filter (b) IV curves for different cases

When a filter was used there was less difference in the results for the different types of radiative coolers used. Figure 5-27 (b) shows that while the no cooling case clearly had the lowest output, there was little difference between the three other cases. The copper cooler produced the highest voltage output while the aluminum cooler produced the highest current voltage. The optimized copper-aluminum cooler performed slightly worse than both the aluminum and copper coolers. The average value of the three experiments was used with the standard deviation of these results calculated. These values were adjusted for errors in wires and multimeter values to create the error bars shown in Figure 5-27 (b). Figure 5-28 reaffirms this by comparing the MPP values calculated for each radiative cooler using the average values found for current and voltage.

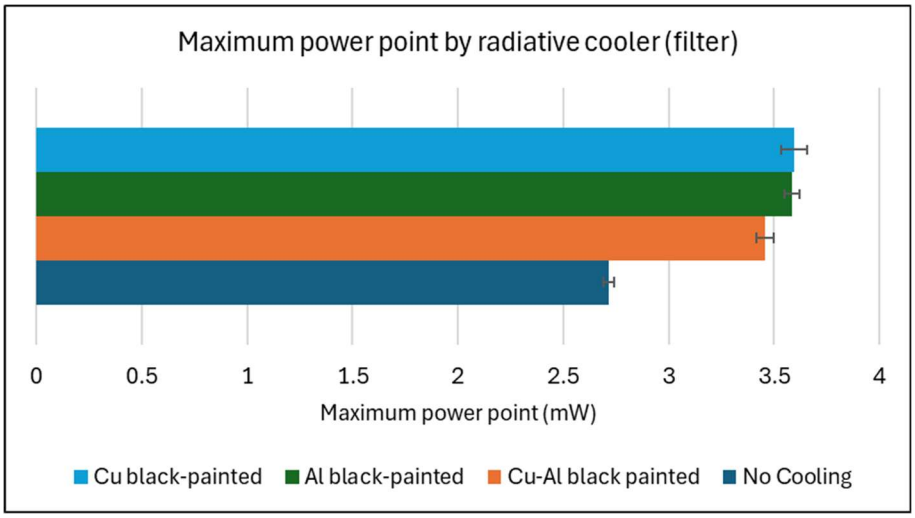

Figure 5-28: Maximum power point calculated for filter cases

It can be seen in Figure 5-28 that the black-painted copper and black painted aluminum cases had very close MPP at 3.59 mW and 3.58 mW respectively. The black painted Cu-Al had a value of 3.46 mW in comparison to the other two. The experimental results were consistent on all three runs for each case as demonstrated by the errors bars calculated using upper bound and lower bound MPP values from experimental data.

It can be observed that the MPP was lower with the filter compared to the no filter case. This can be explained by the filter only allowing photons from a certain wavelength range through and filtering out some useful photons that get used in the no filter case resulting in lower power output. The spectral filter used was not optimized for this TPV cell used with a maximum wavelength of 1600 nm as illustrated by Figure 4-23 in Section 4.2.9. However, the TPV cell used operated at wavelengths up to 1800 nm implying that some photons in the 1600 nm to 1800 nm range, that could have generated electricity, were not allowed to transmit through the spectral filter. This may have impacted cooler performance comparison by not allowing it to reach higher temperatures that would demonstrate clearly differences in cooling power.

5.5.3 Cell temperature comparison

The temperatures reached by the TPV cell for each case used in both no filter and filter experiments are shown in Figure 5-29 below.

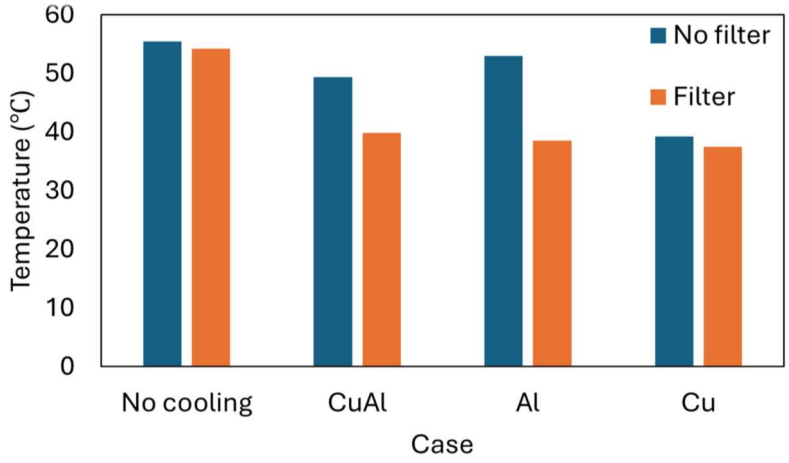

Figure 5-29: Cell temperature comparison with and without spectral filter

The impact of the spectral filter can be observed in Figure 5-29 above with all the filter experiments leading to lower cell temperature compared to no filter. The no cooling case led to the highest temperatures while the copper cases had the lowest temperatures as expected. The optimized copper-aluminum cooler resulted in a lower temperature for the no filter case compared to the aluminum cooler, but it was the reverse with the filter. This is consistent with the IV-curves shown previously and was consistent with theory where a cell performs better when its temperature is lower. These results further solidified the possibility that the higher temperatures would have helped produce better results for the filter case. The filter cases were only separated by 3 degrees while the no filter cases varied by 14 degrees for the three coolers used.

5.5.4 Temperature gradients across coolers

Another set of measurements done in this experiment concerned the temperature gradient across the coolers used and the results are shown below in Figure 5-30.

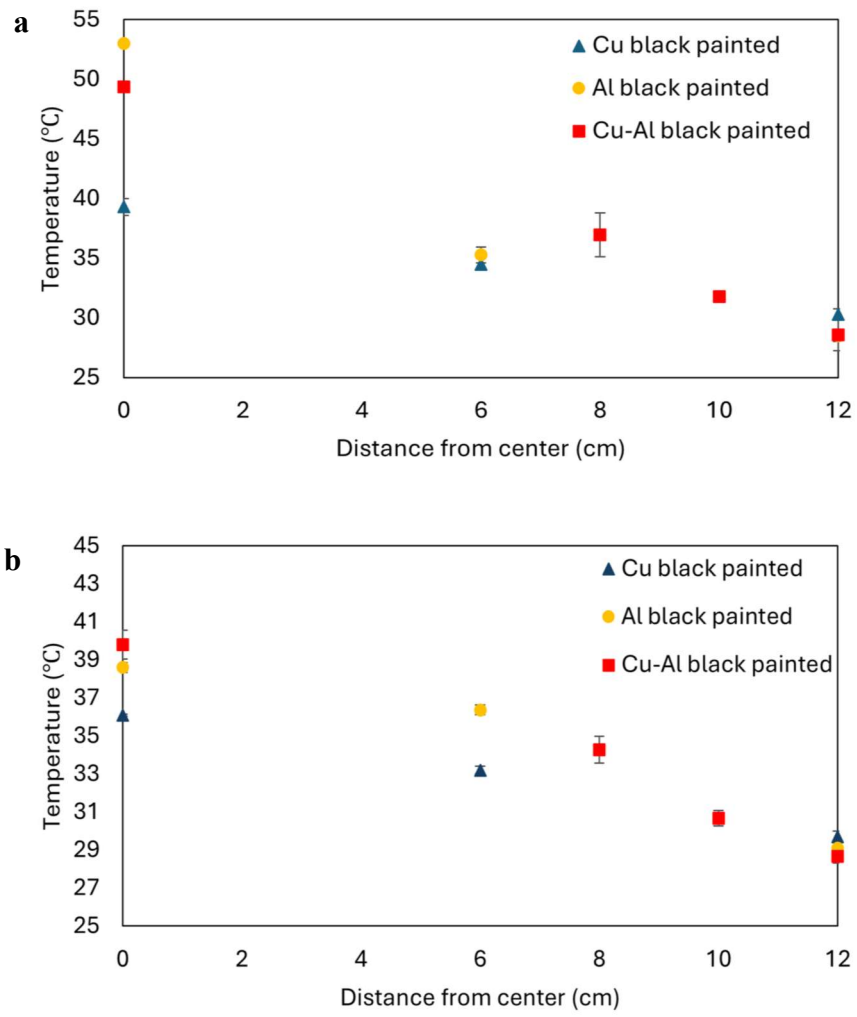

Figure 5-30: Temperature gradient across coolers using (a) no filter (b) filter

The no cooling case was not considered. The results in Figure 5-30 (a) show the copper had the lowest temperature gradient across it due to its high thermal conductivity. Its ability to spread the heat more evenly across its surface leads to a lower temperature at its center where the cell is located. The aluminum cooler has the highest temperature of the three and compared to the optimized copper-aluminum cooler, the temperature drops off faster. For the copper-aluminum cooler, a drop-off in temperature can be observed at the points 8 cm and 10 cm away from the center which is where the panels intersect. The first part of the curve has roughly the same gradient as the copper curve followed by a faster drop-off for the aluminum part of the cooler.

Figure 5-30 (b) shows the result for the filter case with the copper case being the best one again. The aluminum and copper-aluminum cases are very close to each other in terms of gradient with the copper-aluminum cooler having a slightly worse gradient.

5.5.5 Weight and performance comparison

This section investigates the relationship between the maximum cell power output, MPP, as well as temperature with the weight of the radiative coolers. Figure 5-31 shows how they compare with each other.

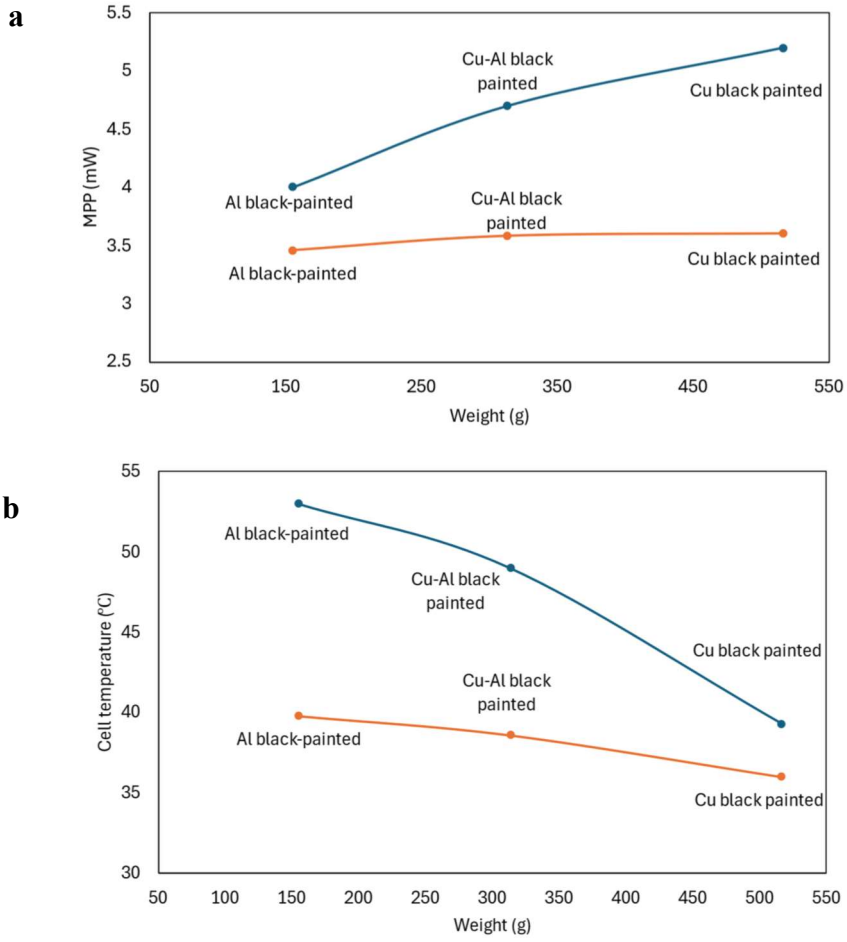

Figure 5-31: (a) Comparison between power output and weight (b) Comparison between cell temperature and weight

In Figure 5-31 (a), an increase in MPP can be observed with an increase in weight for both cases. Conversely in Figure 5-31 (b), as the weight of the radiative cooler increases, the temperature of the cell decreases. These are both related as the heavier copper radiative cooler leads to the lowest temperature. A comparison between the black-painted Cu-Al and black-painted Al radiative coolers, in the no filter case, shows an increase of 0.7 mW (17.5 %) in power output with an additional weight of 158 g for the Cu-Al cooler while the temperature of the cell decreases by 4 °C. The black-painted copper radiative cooler is 203 g heavier than the black-painted Cu-Al cooler and leads to a power output increase of 0.5 mW (10.6 %) along with a significant cell temperature decrease of 9.7 °C. The filter case results follow the same trend but with less consequent differences due to the low differences in temperature between the three cases. These results show that the Cu-Al radiative cooler provides a significant increase in cell output and better cooling performance than the Al cooler. While the Cu radiative cooler leads to the best output, the

increase is not as significant as the difference between Al and Cu-Al and it results in a large increase in weight. These results further solidify previous observations made in this research where the Cu-Al cooler is the best choice to balance weight minimization and cooling performance.

6 Conclusion

TPV systems and small satellites are two fields have both garnered significant interests in recent years due to rapid technological progress and falling launch costs. The high heat to power conversion efficiency of TPV cells without the need of moving parts make them highly suitable for use with small satellite to meet their power demands without compromising space and affecting overall weight. A key challenge, cooling, was addressed with a solution that provides adequate cooling while minimizing weight. This research demonstrated the distinct advantages possessed by deployable multi-material radiative coolers by accomplishing the three main objectives identified as described below:

- Objective 1: Use numerical modeling to design a multi-material deployable radiative cooler with high cooling performance, and low volumetric and gravimetric densities.

  COMSOL simulations were used to study the impact of various geometry changes and materials on cooling performance. The created models were successfully validated via an in-lab experiment. The theoretical and experimental results showed a very close correlation with an R-squared value of 0.976. This confirmation of the validity of the simulations allowed a parametric study to be carried out where the multi-material radiative cooler, made of copper and aluminum, was selected. A 24 cm by 24 cm, 1 mm thick radiative cooler with a 14 cm by 18 cm copper interior was chosen using a relative temperature change by weight metric which accomplished the requirements of objective 1. The model was used for further analysis using space conditions.

- Objective 2: Build a vacuum based experimental setup to test the radiative coolers.

  A functional experimental setup was designed and built to replicate the space environment. The vacuum chamber used reached a vacuum pressure of 10 mTorr and operated at room temperature. The interior of the chamber was able to absorb 71% of all incoming radiation. A holder along with insulators to minimize conduction heat loss was fabricated and used to help consistently position the coolers being tested. While some compromises were made, the setup performed well with several repeatable experiments carried out to analyze various radiative coolers and a TPV system, hence, objective 2 was met.

- Objective 3: Using the experimental apparatus from objective 2, build a multi-material cooler and measure its ability to cool a TPV cell within a TPV system.

  A multi-material designed as part of objective 1 was successfully tested in the vacuum chamber constructed in objective 2. The cooler was built out of copper and aluminum based on the dimensions obtained from the parametric study conducted on COMSOL. They were joined with glued ceramic plates and were used as part of a TPV setup. The effectiveness of the chosen radiative cooler was compared to other alternatives and the results demonstrated its higher performance. Objective 3 was achieved with the cooler being keep the TPV cell cool within a TPV system.

The copper-aluminum radiative cooler was determined to have a cooling power of 20 W in space conditions with an operating temperature of 300 K. Figure 6-1 shows how the designed cooler performs against existing radiative cooler designs from industry and academia.

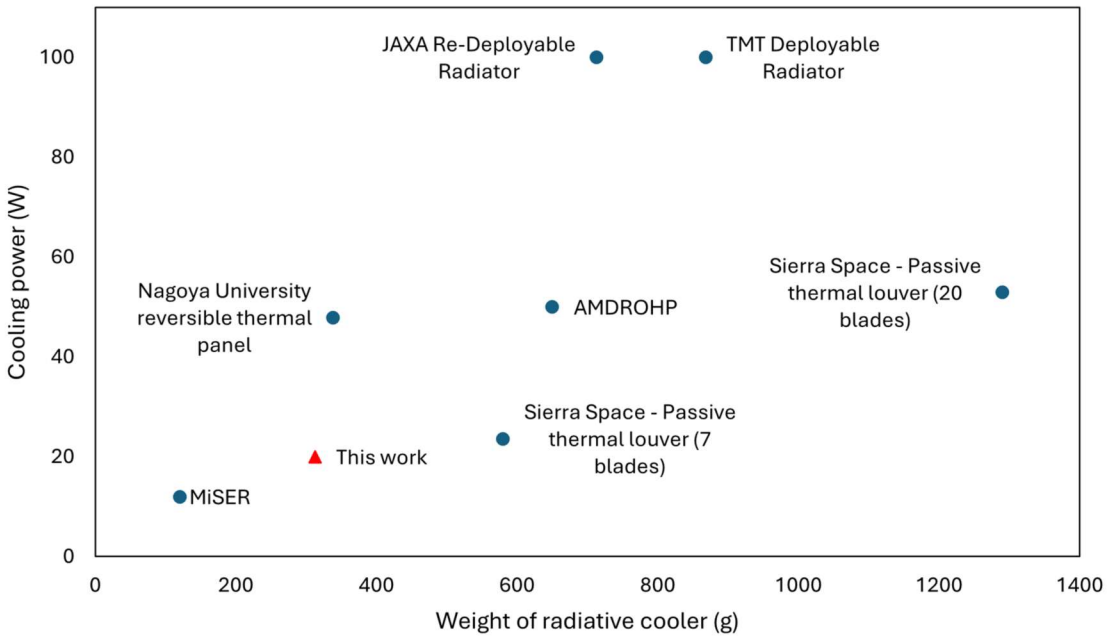

Figure 6-1: Results of this work compared to existing radiative coolers

The designed cooler, as shown in Figure 6-1, was shown to be potentially competitive with comparable designs. It weighed 313 g and provided 20 W of cooling power which places it in line with commercially available products. It can be observed that the Nagoya University reversible thermal panel design performs better than our design. This can be attributed to the use of a larger radiative area and the use of pyrolytic graphite sheets which possess a thermal conductivity 3.8 times higher than copper. [84] The latter is a very promising material for thermal control, however, previous tests have shown material erosion when used in low earth orbit which could be a concern for longer term missions. [85] The cooling power of the cooler designed in this research can be improved through the use of novel materials and improvements in interfacial thermal conductance. Additionally, a proper deployment mechanism for small space vessels still needs to be designed. This is discussed further in the future work section.

The developed radiative cooler is well-suited for integration with small satellites, offering reduced launch expenses and enhanced payload capacity owing to its lightweight design and compact foldability during storage. This advancement in thermal management is likely to enable the implementation of additional space projects involving TPV technology in the future.

6.1 Future work

While the effectiveness of the multi-material radiative cooler was demonstrated, there are still areas for improvement regarding the design itself and experimental processes which demand further work. They are as follows:

1. Experimental setup improvements

   Throughout this results and discussion section, experimental errors including wire losses, measurement uncertainties, thermal heat transfer inadequacies, and measurement errors were discussed and corrections applied where possible. However, one major factor that could have potentially affected results was the vacuum level reached in the vacuum chamber used. Due to budget constraints, a vacuum pressure of 10 mTorr was utilized throughout all experiments which is higher than ideal. Additionally, the experiments were conducted at room temperature. Low earth orbit involves pressures ranging from 10^{-10} to $5x10^{-8}$ mTorr [86] which is significantly lower than the pressure used in the vacuum chamber. This implies that in the experiment conducted in the lab, there were more air molecules present leading to a certain cooling impact on the radiative cooler. Moreover, at lower pressures, there is a larger amount of outgassing that occurs and some of the materials used in the experiment, such as the halogen bulb, are not entirely suitable for these much lower pressures.

   For future experiments, a vacuum chamber capable of reaching these lower pressures should be used. The experiment would require the use of a different emitter that can be reliably used in space without any material outgassing. The setup components such as the stand, TPV cell, photon reflector, ellipsoidal cavity, and spectral filter do not need to be changed. All wires used should be suitable for use at that pressure. This will lead to more adequate results and measurements regarding temperature and IV curve data.

   The results obtained in this research, while reasonably accurate, may have undergone a small amount of additional cooling due to the air molecules still present in the chamber. This may have led to slightly lower temperatures compared to real conditions in space. It is expected that at lower pressure, an increase in temperature would be observed for all cases. Moreover, the comparison in performance between cooler should show a greater discrepancy in temperatures between the better cooler and the worst one. This should further accentuate the advantage of using the Cu-Al cooler rather than the Al cooler.

2. Interfacial thermal conductance improvements

   As discussed in this research, interfacial thermal conductance plays a critical role in determining cooling performance. The heat generated by a particular source needs to be transferred as quickly as possible to a radiator to keep temperatures low. Key factors such as contact pressure and surface deformities affect conductance and can be further mitigated. Further research in highly thermally conductive materials such as pyrolytic graphite and carbon nanotubes can lead to improve heat transfer for the TPV cell to the radiative cooler.

Moreover, a more conductive substrate to the TPV cell itself could further improve performance.

For this experiment, a thermal pad was used between the cell substrate and the TPV cell. This material may undergo some outgassing over the long-term leading to decreased performance. An improvement in TPV cell connection to its substrate as well as investigating the use of thermal interfaces suitable for low-earth orbit pressure can be further investigated to improve thermal conductance while ensuring suitability for long-term missions.

Regarding the panels, this experiment involved a direct connection between the materials while in practice an interface such as a hinge would be involved with potentially improved and more even heat transfer across all sides of the cooler

3. Deployable mechanism and testing

The designed multi-material radiative cooler would be deployable in practice. There are multiple mechanisms that can be used for deployment, such as hinges and actuator system or bimetallic coils that would be suitable for the designed radiative cooler. For space applications, any design needs to be able to withstand the heavy vibrations experienced by a spacecraft during launch while being able to reliably deploy when in space. A more thorough mechanical analysis would need to be done for the chosen design. As previously mentioned, adequate heat transfer between panels is also required.

The use of dynamic thermal control can allow for more flexibility using changes in radiative area. A mechanism that can deploy and retract these panels in a controlled manner would be of interest and can be further investigated in the future.

4. Shape and panel folding

The multi-materials can be folded in multiple ways before being deployed. Further research in origami structures along with a corresponding reliable deployment mechanism could help identify the more efficient ways of storing the radiative cooler at launch. This would also allow for potentially larger radiative coolers to be used. The shape of the radiative cooler may change based on the folding techniques chosen.

5. Scalability

The designed cooler is suitable for small satellites but its use in larger space vessels requires further analysis. The parametric study conducted, and the results obtained were suitable for a specific case. As the size of the problem increases, the optimal dimensions for the radiative cooler would not necessarily scale linearly. While the amount of radiation is proportional to the surface area of the cooler, other factors such as mass and volume would not increase consistently especially when taking into account the use of multiple materials. A case involving a larger radiative cooler would require a new parametric study with adjusted parameters to determine the new optimal dimensions. A study could be

performed for different satellite sizes to compare how the size of the cooler would change including the proportion of copper and aluminum.

7 References

[1] V. L. Teofilo, P. Choong, J. Chang, Y.-L. Tseng and S. Ermer, "Thermophotovoltaic Energy Conversion for Space," *Journal of Physical Chemistry C,* vol. 112, pp. 7841-7845, 2008.

[2] D. Kopper and M. S. Leite, "Material Screening for Thermophotovoltaic Optical Emitters," *ACS Applied Energy Materials,* vol. 8, no. 7, pp. 4144-4151, 2025.

[3] N. Talebzadeh, A. Pirvaram and P. G. O'Brien, "Ellipsoidal Optical Cavities for Enhanced Thermophotovoltaics," *IEEE JOURNAL OF PHOTOVOLTAICS,* vol. 12, no. 1, p. 353, 2022.

[4] L. Tang, L. M. Fraas, Z. Liu, H. Duan and C. Xu, "Doping Optimization in Zn-Diffused GaSb Thermophotovoltaic Cells to Increase the Quantum Efficiency in the Long Wave Range," *IEEE Transactions on Electron Devices,* vol. 64, no. 12, pp. 5012-5018, 2017.

[5] S. Chen, Y. Guo, Q. Pan and Y. Shuai, "A review on current development of thermophotovoltaic technology in heat recovery," *International Journal of Extreme Manufacturing,* vol. 6, no. 2, p. 022009, 2024.

[6] N.-P. Harder and P. Wurfel, "Theoretical limits of thermophotovoltaic solar energy conversion," *Semiconductor Science and Technology,* vol. 18, no. 5, 2003.

[7] P. Martín, V. Orejuela, A. Cano, I. García, A. Luque and I. Rey-Stolle, "Cost-effective 23.2% efficient germanium thermophotovoltaic converters for thermal batteries," *Cell Reports Physical Science,* vol. 5, no. 10, p. 102231, 2024.

[8] B. Roux, C. Lucchesi, J.-P. Perez, P.-O. Chapuis and R. Vaillon, "Main performance metrics of thermophotovoltaic devices: analyzing the state of the art.," *Journal of Photonics for Energy,* vol. 14, no. 4, p. 042403, 2024.

[9] H. M. Tun, "Computer Aided Software Design (CASD) for Light Emitting Diode Modeling.," *International Journal of Computing and Related Technologies,* vol. 2, no. 2, p. 15, 2019.

[10] S. Preet, "A review on the outlook of thermal management of photovoltaic panel using phase change material," *Energy and Climate Change,* vol. 2, no. ISSN 2666-2787, p. 100033, 2021.

[11] B. Wedlock, "Thermo-photo-voltaic energy conversion," *IEEE,* vol. 51, no. 5, pp. 694 - 698, 1963.

[12] R. M. Swanson, "Proposed thermophotovoltaic solar energy conversion system," *IEEE,* 1979.

[13] A. LaPotin, K. L. Schulte, M. A. Steiner, K. Buznitsky, C. C. Kelsall, D. J. Friedman and E. J. Tervo, "Thermophotovoltaic Efficiency of 40.," *Nature (London) 604, no. 7905,* p. 287–91, 2022.

[14] A. Martin and A. Datas, "Thermophotovoltaic energy in space applications: Review and future potential," *Solar Energy Materials and Solar Cells,* vol. 161, no. 0927-0248, pp. 285-296, 2017.

[15] B. Roy-Layinde, J. Lim, C. Arneson, S. R. Forrest and A. Lenert, "High-efficiency air-bridge thermophotovoltaic cells," *Joule,* vol. 8, no. 7, pp. 2135-2145, 2024.

[16] A. Datas and A. Marti, "Thermophotovoltaic energy in space applications: Review and future potential," *Solar Energy Materials and Solar Cells,* vol. 161, no. ISSN 0927-0248, pp. 285-296, 2017.

[17] D. W. Hengeveld, M. R. Wilson, J. A. Moulton, B. S. Taft and A. M. Kwas, "Thermal design considerations for future high-power small satellites," in *48th International Conference on Environmental Systems* , Albuquerque, New Mexico, 2018.

[18] SpaceX, "Smallsat Rideshare Program," [Online]. Available: https://www.spacex.com/rideshare/. [Accessed 14 May 2025].

[19] H. W. Jones, "The Recent Large Reduction in Space Launch Cost," in *International Conference on Environmental Systems*, Albuquerque, NM, 2020.

[20] F. P. Incropera, D. P. Dewitt, T. L. Bergman and A. S. Lavine, Fundamentals of heat and mass transfer, New York: John Wiley & Sons, 2006.

[21] A. S. Allawi and A. M. Abdullah, "Effects of pressure, temperature, and surface roughness on thermal contact conductance across copper-aluminum interface," *Journal of Multidisciplinary Engineering Science and Technology,* vol. 7, no. 8, pp. 12581-12585, 2020.

[22] "2000 ASTM Standard Extraterrestrial Spectrum Reference E-490-00," NREL, [Online]. Available: https://www.nrel.gov/grid/solar-resource/spectra-astm-e490.html. [Accessed 27 December 2024].

[23] "AZ-400-LSW White Thermal Control Paint / Coating," AZ Technology, [Online]. Available: https://www.aztechnology.com/product/9/az-400-lsw. [Accessed 3 January 2025].

[24] BOEING, "Active Thermal Control System (ATCS) Overview," [Online]. Available: https://www.nasa.gov/pdf/473486main_iss_atcs_overview.pdf.

[25] J. R. Cannon, R. B. Mulford and B. D. Iverson, "Triangular fin array passively actuated by bimetallic coils for CubeSat thermal control," *Applied Thermal Engineering,* vol. 240, no. ISSN 1359-4311, p. 122239, 2024.

[26] Y. Akizuki, H. Nagano, T. Kinjo, K. Sawada, H. Ogawa, T. Takashima, K. Nishiyama, H. Toyota, K. Watanabe and T. Kuratomi, "Development and testing of the re-deployable radiator for deep space explorer.," *Applied Thermal Engineering,* vol. 165, no. 1359-4311, p. 114586, 2020.

[27] A. Evans, "Design and Testing of the CubeSat Form Factor Thermal Control Louvers," in *33rd Annual AIAA/USU Conference on Small Satellites*, Logan, Utah, 2019.

[28] C. L. Bertagne, J. D. Whitcomb, D. J. Hartl and L. Erickson, "Experimental Characterization of a Composite Morphing Radiator Prototype in a Relevant Thermal Environment," in *AIAA 2017-1877. 25th AIAA/AHS Adaptive Structures Conference.*, Grapevine, Texas, 2017.

[29] J. R. Cannon, K. N. Havey, N. S. Housley, R. B. Mulford and B. D. Iverson, "Internally stowed, radially deployed radiator panels for passive CubeSat thermal control," *Applied Thermal Engineering,* vol. 270, no. ISSN 1359-4311, p. 126281, 2025.

[30] H. Nagano, A. Ohnishi and Y. Nagasaka, "Development of a lightweight deployable/stowable radiator for interplanetary exploration," *Applied Thermal Engineering,* vol. 31, no. 16, pp. 3322-3331, 2011.

[31] NASA, "An Additively Manufactured Deployable Radiator with Oscillating Heat Pipes (AMDROHP) to Enable High Power Lunar CubeSats," [Online]. Available: https://www.nasa.gov/sites/default/files/atoms/files/9._2022_amdrohp_stp_tech_expo.pdf.

[32] T. Madison, A. A. Moreno, A. Delgado and J. McHale, "Small Satellite Deployable Radiator Study," in *CubeSat Developers Workshop*, Thermal Control Department - The Aerospace Corporation, 2024.

[33] L. Anderson, C. Swenson, A. Mastropietro and J. Sauder, "Active Thermal Architecture: Design and Status," in *34th Annual Small Satellite Conference* , Logan, UT, 2020.

[34] L. N. B. III, R. Gupta, I. Nicolaescu, C.-H. Chen and W. Anderson, "3D Printed Loop Heat Pipe With Deployable Radiator," in *53rd International Conference on Environmental Systems* , Louisville, Kentucky , 2024.

[35] Vought Corporation, "Flexible radiator system," NASA Johnson space center, Houston, Texas, 1982.

[36] A. Lécossais, F. Jacquemart, G. Lefort, E. Dehombreux, F. Beck and V. Frard, "Deployable Panel Radiator," in *47th International Conference on Environmental Systems*, Charleston, South Carolina , 2017.

[37] Sierra Space, "Spaceflight hardware catalog," [Online]. Available: sierraspace.com/spaceflight-hardware-catalog. [Accessed 20 April 2025].

[38] Dcubed, "Deployable Radiator," [Online]. Available: https://dcubed.space/products/deployable-radiator/. [Accessed 2 April 2025].

[39] B. Bauer and C. S. Mukherjee, "FENNEC: A Deployable Radiator for The Next Generation of High-Power SmallSats," in *European Space Thermal Engineering Workshop*, 2024.

[40] "Thermal Management Technologies Deployable radiator," [Online]. Available: https://satsearch.co/products/thermal-management-technologies-deployable-radiator. [Accessed 28 March 2025].

[41] Tmt-ipe, "Spacecraft radiators," [Online]. Available: https://www.tmt-ipe.com/spaceceraft-radiators. [Accessed 18 March 2025].

[42] Redwire Space, "Product spec sheets - Deployable Radiator Q-Rad," [Online]. Available: https://redwirespace.com/capabilities/spec-sheets/. [Accessed 4 January 2025].

[43] ThermAvant Technologies, "Case study: Power-densed OHP based spacecraft thermal control," [Online]. Available: https://www.thermavant.com/case-study/albedo-and-thermavant-tech-power-dense-ohp-based-spacecraft-thermal-control. [Accessed 25 April 2025].

[44] D. Gilmore, "Radiators," in *Spacecraft Thermal Control Handbook*, El Segundo, California, The aerospace press, 2002.

[45] B. Yendler, A. Meginnis and A. Reif, "Thermal Management for High Power Cubesats," in *34th Annual AIAA/USU Small Satellite Conference* , Logan, Utah, 2020.

[46] M. T. Wescott, J. S. McQuien, C. L. Bertagne, J. D. Whitcomb, D. J. Hartl and L. R. Ericksonk, "Design and Fabrication of a Composite Morphing Radiator Panel Using High Conductivity Fibers," in *AIAA SciTech 2017*, Grapevine, TX, 2017.

[47] ASTM, "ASTM E595-15(2021) Standard Test Method for Total Mass Loss and Collected Volatile Condensable Materials from Outgassing in a Vacuum Environment," [Online]. Available: https://store.astm.org/e0595-15r21.html. [Accessed 20 March 2025].

[48] J. Dever, B. Banks, K. D. Groh and S. Miller, "Degradation of Spacecraft Materials," in *Handbook of environmental degradation of materials*, 2004.

[49] Y. Ishikawa, Y. Fuchita, T. Hitomi, Y. Inoue, M. Karita, K. Hayashi, T. Nakano and N. Baba, "Survivability of carbon nanotubes in space," *Acta Astronautica,* vol. 165, no. ISSN 0094-5765, pp. 129-138, 2019.

[50] Q. X, H. J. Y. Ren, Y. Ou, B. Liu, Y. Wang, Y. Chen, P. Long, C. Deng and J. Wang, "VO2-Based Spacecraft Smart Radiator with High Emissivity Tunability and Protective Layer," *Nanomaterials ,* vol. 14, no. 16, p. 1348, 2024.

[51] D. Xu, J. Zhao and L. Liu, "Near-field radiation assisted smart skin for spacecraft thermal control," *International Journal of Thermal Sciences,* vol. 165, no. 1290-0729, p. 106934, 2021.

[52] M. Delkowski, J. V. Anguita, C. T. G. Smith and S. R. P. Silva, "Multifunctional Nanostructures with Controllable Band Gap Giving Highly Stable Infrared Emissivity for Smart Thermal Management," *ACS Nano,* vol. 17, no. 2, pp. 1335-1343, 2023.

[53] B. M. Diaconu, M. Cruceru and L. Anghelescu, "Phase change materials in space systems. Fundamental applications, materials and special requirements – A review," *Acta Astronautica,* vol. 216, no. 0094-5765, pp. 163-213, 2024.

[54] J. Scialdone, C. Clatterbuck and J. Wall, "Thermal Conductance of Two Interface Materials and Their Applications in Space Systems," NASA Goddard Space Flight Center, Greenbelt, MD, 1992.

[55] Thermal Management Technologies, "Thermal components," [Online]. Available: https://www.tmt-ipe.com/thermal-components. [Accessed 25 March 2025].

[56] NASA, "State-of-the-Art of Small Spacecraft Technology," NASA, 2024.

[57] Parker Chromerics, "THERM-A-GAP 579 Thermally Conductive Gap Filler Pads," [Online]. Available: https://ph.parker.com/ca/en/product-list/therm-a-gap-579-thermally-conductive-gap-filler-pads. [Accessed 10 April 2025].

[58] Acktar advanced coatings, "Black & White Thermal Control Coatings Comparison Experiment," 11 March 2021. [Online]. Available: https://acktar.com/thermal-control-coatings/. [Accessed 16 March 2025].

[59] R. C. Youngquist, M. A. Nurge, W. L. Johnson, T. L. Gibson and J. M. Surma, "Cryogenic Deep Space Thermal Control Coating," *Journal of Spacecraft and Rockets,* vol. 55, no. 3, pp. 622-631, 2018.

[60] L. Leeper, K. Jones, M. Finckenor, J. McElderry and M. Carrico, "Thermal Control Coatings Flown on Low Earth Orbit Materials Experiments," *Journal of Spacecraft and Rockets,* vol. 61, no. 5, p. 1329–1338, 2024.

[61] AZ Technology, "Paints & Coatings," [Online]. Available: https://www.aztechnology.com/products-cat/1/paints-coatings. [Accessed 24 June 2024].

[62] L. Kauder, "Spacecraft Thermal Control Coatings References," NASA/Goddard Space Flight Center, Greenbelt, Maryland, 2005.

[63] J. H. Henninger, "Solar absorptance and thermal emittance of some common spacecraft thermal-control coatings," NASA Goddard Space Flight Center, Greenbelt, MD, 1984.

[64] R. Mell and G. Wertz, "Testing and optimization conductive spacecraft of electrically conductive spacecraft coatings," Marshall Space Flight Center, Alabama, 2002.

[65] Sumitaka Tachikawa, Hosei Nagano, Akira Ohnishi and Yuji Nagasaka, "Advanced Passive Thermal Control Materials and Devices for Spacecraft: A Review," *International Journal of Thermophysics,* vol. 43, no. 6, p. 91, 2022.

[66] D. Gilmore, Spacecraft Thermal Control Handbook Volume I: Fundamental Technologies, 2nd ed., California: The Aerospace Press, 2002.

[67] M. N. Thornblom, J. Beverly and J. J. O'Connell, "Technical Capability Upgrades to the NASA Langley Research Center 8 ft. by 15 ft. Thermal Vacuum Chamber," in *Space Simulation Conference*, Annapolis, MD, 2016.

[68] "European Space Agency," [Online]. Available: https://technology.esa.int/page/phenix-tvac-test-facility. [Accessed 22nd August 2023].

[69] R. Dunwoody, J. Reilly, D. Murphy, M. Doyle, J. Thompson, G. Finneran, L. Salmon, C. O'Toole, S. Reddy Akarapu, J. Erkal and e. al., "Thermal Vacuum Test Campaign of the EIRSAT-1 Engineering Qualification Model," *Aerospace,* vol. 9, no. 2, p. 99, 2022.

[70] "Space Thermal and Vacuum Environment Simulation," *Space Flight. InTech.,* June 20 2018.

[71] Kurt J. Lesker Company, "KJLC® 375 Series Panel Mount / Benchtop Gauge Controller," [Online]. Available: https://www.lesker.com/newweb/gauges/convection_kjlc_5.cfm.

[72] Varian vacuum products, "Instruction manual No. 699904400 Revision 2," April 1997. [Online].

[73] Amazon, "Aluminum Black Foil Tape Matt None Reflective Heavy Duty 3.94 Mil 2Inch x 33Feet High Thermal Conductive Adhesive Hot Cold Air Duct Tape for Metal Repair Pipe(NC233)," LLPT, [Online]. Available: https://a.co/d/8LVwXGt.

[74] Amazon, [Online]. Available: https://www.amazon.ca/dp/B0BXPVKZXH?ref=ppx_yo2ov_dt_b_fed_asin_title. [Accessed 15 October 2024].

[75] X. Li, Z. Sun, L. Gu, J. Han, J. Wang and S. Wu, "Research of fuel temperature control in fuel pipeline of diesel engine using positive temperature coefficient material," *Advances in Mechanical Engineering,* vol. 8, no. 1, pp. 1-11, 2016.

[76] "Thermocouple types," Omega.ca, [Online]. Available: https://www.omega.ca/en/resources/thermocouple-types. [Accessed 2 January 2025].

[77] "Philips 50W Halogen GU10 Flood Light Bulb (6-Pack)," Home Depot, [Online]. Available: https://www.homedepot.ca/product/philips-50w-halogen-gu10-flood-light-bulb-6-pack-/1000116071. [Accessed 2 December 2025].

[78] "EXTREME ODYSSEY 85x45x0.5mm," Thermalright, [Online]. Available: https://thermalright.com/product/odyssey-thermal-pad-0-5-mm/. [Accessed 10 December 2025].

[79] Edmund Optics, "1600nm 25mm Diameter , OD 2.0 Shortpass Filter," [Online]. Available: https://www.edmundoptics.ca/p/1600nm-25mm-diameterod-2-shortpass-filter/27725/. [Accessed 15 May 2025].

[80] J. G. Hurst and A. B. Lankford, THERMAL CONDUCTIVITY OF ALUMINUM, COPPER, IRON, AND TUNGSTEN FORTEMPERATURESFROM 1 K TO THE MELTING POINT, Boulder, Colorado: National Bureau of Standards, June 1984.

[81] J.-P. MONCHAU, L. IBOS, M. MARCHETTI, J. DUMOULIN and V. FEUILLET, "Importance and limitation of spectral measurements for emissivity measurement," Themacs ingenierie.

[82] A. B. Narimane Blanchete, "Thermal design, analysis and test: Framework for CubeSat in low Earth orbit," *Results in Engineering,* vol. 24, no. ISSN 2590-1230, p. 103401, 2024.

[83] J. Ishii and A. Ono, "Uncertainty estimation for emissivity measurements near room temperature with a Fourier transform spectrometer," *Measurement Science and Technology,* vol. 12, no. 12, 2001.

[84] A. Fernández-Soler, I. Torralbo, I. Pérez-Grande, R. T. Pardavila and T. Anzai, "Study of pyrolitic graphite sheet potential as thermal passive element in CubeSats," *Advances in Space Research,* vol. 71, no. 11, pp. 4431-4442, 2023.

[85] K. K. d. Groh and B. A. Banks, "The Erosion of Diamond and Highly Oriented Pyrolytic Graphite After 1.5 Years of Space Exposure," NASA, 2018.

[86] NASA Technical Standards system, "Low Earth Orbit Spacecraft Charging Design Standard," [Online]. Available: https://standards.nasa.gov/standard/NASA/NASA-STD-4005. [Accessed 2 08 2025].

[87] R. B. Mulford, M. R. Jones and B. D. Iverson, "Dynamic Control of Radiative Surface Properties with Origami-Inspired Design," *NASA Rocky Mountain Space Grant Consortium,* 2015.

[88] ""Generate an image of a small cubesat in space with the Earth and sun in the background in different directions" prompt," Copilot, Microsoft, 24 January 2025. [Online].

[89] M. K. Choi, "AZW-LA-II White Paint on Swift: Lessons Learned from First Time Flying on Spacecraft Radiators," in *2nd International Energy Conversion Engineering Conference*, Providence, RI, 2004.

[90] Dcubed, "Deployable Radiator," [Online]. Available: https://dcubed.space/products/deployable-radiator/. [Accessed 12 April 2025].

[91] Y. Akizuki, H. Nagano, T. Kinjo, K. Sawada, H. Ogawa, T. Takashima, K. Nishiyama, H. Toyota, K. Watanabe and T. Kuratomi, "Development and Testing of the Re-Deployable Radiator for Deep Space Exploration Technology Demonstrator, DESTINY," in *49th International Conference on Environmental Systems* , Boston, Massachusetts, 2019.

[92] M. T. Kudlac, H. F. Weaver and M. D. Cmar, "Thermal Vacuum Integrated System Test at B–2," in *24th Space Cryogenics Workshop*, Coeur D'Alene, ID, 2012.

[93] W. W. Gay and W. E. Ellis, "Vacuum chamber heat-transmission analysis," NASA, 1967.